DISSERTATION

submitted to the

Combined Faculty of Mathematics, Engineering and Natural Sciences

of Heidelberg University, Germany

for the degree of

Doctor of Natural Sciences

Put forward by

Anna Katharina Scheipers

born in Karlsruhe (Germany)

Oral examination: 30.04.2025

Quantitative Sodium Magnetic Resonance Imaging of the Human Torso at 7 Tesla

Referees: Prof. Dr. Mark E. Ladd
Prof. Dr. Leif Schröder

Quantitative Natrium-Magnetresonanztomographie des Körperstamms bei 7 Tesla

Diese Arbeit etabliert ein Setup und Nachbearbeitungsschritte für die nichtinvasive Bestimmung der scheinbaren Gewebenatriumkonzentration (aTSC) in einem großen Sichtfeld (FOV) des menschlichen Torsos mittels ^{23}Na-MRT bei 7 T. Ein Referenzflaschen-Setup für die ^{23}Na-Quantifizierung wurde entwickelt und mit T_1-, B_1^+- und aufbauspezifischen simulierten B_1^--Korrekturen kombiniert. Die korrigierten Phantommessungen zeigten eine maximale Abweichung vom wahren Wert von 3,4 % und eine maximale Standardabweichung von 0,3 mM zwischen den Messungen. Für die quantitativen ^{23}Na-MR-Bilder wurde eine Rekonstruktion überlappender Datenteilmengen verwendet, um Veränderungen der renalen aTSC während des Trinkens zu untersuchen. Das Verhältnis von medullärer zu kortikaler aTSC betrug 1,71, 2,08 und 1,43 für die erste Probandin und 1,56, 1,89 und 1,69 für die zweite Probandin vor, kurz nach und lange nach dem Trinken. In einer zweiten Studie wurden eine ^{23}Na-HF-Spule und ein 32-Kanal-^{1}H-pTx-Array verwendet, um eine MR-Bildgebung mit zwei Kernen in der gleichen Position in einem FOV von $(400\,\mathrm{mm})^3$ zu ermöglichen. Die mittlere aTSC von drei gesunden Proband*innen wurde in der Leber ((36 ± 6) mM), Milz ((30 ± 7) mM), Gallenblase ((139 ± 19) mM) und weiteren Strukturen bestimmt. Die Durchführbarkeit der zeitaufgelösten ^{23}Na-MRT sowie der kombinierten ^{1}H- und quantitativen ^{23}Na-MRT unter freier Atmung bei 7 T in einem großen FOV in $\leq$47 min wurde gezeigt und damit die Grundlage für eine simultane und genaue aTSC-Bestimmung in mehreren abdominalen Strukturen gelegt.

Quantitative Sodium Magnetic Resonance Imaging of the Human Torso at 7 Tesla

This work presents a setup and a post-processing workflow for the non-invasive determination of the apparent tissue sodium concentration (aTSC) in a large field-of-view (FOV) of the human torso using ^{23}Na MRI at 7 T. A reference vial setup for the ^{23}Na quantification was developed and combined with T_1, B_1^+ and setup-specific simulated B_1^- correction. Corrected phantom measurements showed a maximal difference of 3.4 % from the ground truth value and a maximum standard deviation of 0.3 mM between measurements. A sliding window reconstruction of ^{23}Na MR images was employed to investigate renal aTSC changes during a water load event. Medullary to cortical aTSC ratios of 1.71, 2.08 and 1.43 for volunteer one and 1.56, 1.89 and 1.69 for volunteer two were found before, shortly after and long after water loading. In a second study, the combination of a ^{23}Na RF coil and a 32-channel ^{1}H pTx array was investigated to allow dual-nuclei MRI in the same position for a FOV of $(400\,\mathrm{mm})^3$. The mean aTSC for three healthy volunteers was determined for the liver ((36 ± 6) mM), spleen ((30 ± 7) mM), gallbladder ((139 ± 19) mM) and other structures. The feasibility of time-resolved quantitative ^{23}Na MRI and of combined ^{1}H and quantitative ^{23}Na MRI at 7 T in a large FOV under free breathing in $\leq$47 min is demonstrated, laying the groundwork for an accurate aTSC evaluation of multiple abdominal structures simultaneously.

Contents

List of Abbreviations

3D-DAPR	3D density adapted projection reconstruction
3D GRE-RPE	GRE sequence with radial phase-encoded acquisition
aSC	apparent sodium concentration
ATP	adenosine triphosphate
aTSC	apparent tissue sodium concentration
CSF	cerebrospinal fluid
CV	coefficient of variation
DA	double angle
DAK	dielectric assessment kit
DI	deionized
EM	electromagnetic
FA	flip angle
FID	free induction decay
FLASH	fast low angle shot
FOV	field of view
FWHM	full width at half maximum
GRE	gradient echo
IVC	inferior vena cava
IVD	intervertebral discs
MedSAM	segment anything in medical images
MITK	medical imaging interaction toolkit
MR	magnetic resonance
MRI	magnetic resonance imaging
NMR	nuclear magnetic resonance
NUFFT	nonuniform fast Fourier transform
PSF	point spread function
pTx	parallel transmit
RF	radio frequency
RPE	radial phase-encoded
SAM	segment anything model
SAR	specific absorption rate
SC	sodium concentration

SE	spin echo
SENSE	sensitivity encoding
SNR	signal-to-noise ratio
SOS	sum of squares
SSE	sum of squared error
SST	sum of squared total
TA	acquisition time
T_{E}	echo time
TIAMO	time interleaved acquisition of modes
T_{R}	repetition time
TSC	tissue sodium concentration
UHF	ultra-high field
USF	undersampling factor
UTE	ultra-short echo time
VOI	volume of interest

1 Introduction

Magnetic resonance imaging (MRI) is one of the most used imaging techniques in medicine due to its excellent tissue contrast without the need for ionizing radiation. MRI is extremely flexible, allowing to investigate many different imaging contrasts that can give information about a wide variety of tissue parameters to help understand the human body. Depending on the imaging sequence employed, they range from providing morphological information to imaging diffusion to investigate physiological processes.

For anatomical depiction and generally the majority of MRI measurements, hydrogen (^{1}H) is used as it offers the highest signal in the human body. However, other nuclei with a non-vanishing spin such as ^{13}C, ^{17}O, ^{19}F ^{23}Na , ^{31}P, ^{35}Cl and ^{39}K, called X-nuclei, can also be used in MRI. They can provide additional information on physiology and pathology of the examined tissue that can not be obtained from ^{1}H MRI (Nagel, Amarteifio, et al., 2011; Gerhalter, Gast, Marty, Martin, et al., 2019; Regnery et al., 2020). After the first in vivo ^{1}H MRI in 1973 (Lauterbur, 1973), ^{23}Na was the first X-nuclei to be measured in vivo in 1985 (Hilal et al., 1985). As ^{23}Na provides the second highest signal in the human body and sodium ions play a key role in many metabolic processes, ^{23}Na MRI has since been used to study a multitude of pathologies.

The sodium-potassium ATPase maintains the resting potential of a healthy cell (Gast et al., 2023; Madelin, Lee, et al., 2014) with a gradient between the intra- and extracellular sodium concentration (Maril, Margalit, et al., 2004). The volume-weighted concentration average of both these compartments is the tissue sodium concentration (TSC) (Lu et al., 2010) and the imaging contrast motivating the presented research. Using sodium MRI, the TSC can be quantified (Gast et al., 2023; Madelin, Lee, et al., 2014; Hu et al., 2020; Thulborn, 2018; Zaric, Juras, et al., 2021). As the TSC is sensitive to changes in cell vitality and viability, it can be a potential biomarker for applications ranging from lumbar back pain (Kamp et al., 2024) to heart disease (Ouwerkerk, Bottomley, et al., 2008) to chronic kidney disease (Daniel et al., 2021). To obtain a quantitative ^{23}Na image, the MR signal intensity is calibrated using the known sodium concentrations in internal

(Haneder, Konstandin, et al., 2011; Lott, Platt, et al., 2019; Malzacher et al., 2016) or external references (Haneder, Kettnaker, et al., 2013; Madelin, Xia, et al., 2018; Moon, Furlan, et al., 2014).

The ^{23}Na image acquisition is complicated by several challenges such as a low MR sensitivity and low in vivo Na^+ concentrations, resulting in a lower in vivo signal-to-noise ratio (SNR) compared to hydrogen (Ladd et al., 2018). The development of MR tomographs with higher static magnetic field strengths B_0 have enabled new possibilities as the SNR is expected to increase at least linearly with B_0 for ^{23}Na (Ladd et al., 2018). Most clinical scanners have field strengths of either 1.5 T or 3.0 T, with clinical 7 T scanners being cleared by the FDA in 2017 (Commissioner, 2024). Research scanners have static magnetic fields of up to 20 T (Budinger et al., 2016) to benefit from the increased SNR. At 7 T an adequate SNR for ^{23}Na MRI can be obtained in a clinically feasible measurement time (Kraff et al., 2015). As acquisition times for sodium body MRI are still quite long ($\geq$ 10 min), motion artifacts can decrease image quality (Gast et al., 2023). Additionally, the fast bi-exponential transverse relaxation times require pulse sequences with short echo times, which pose high demands on the hardware (Serai et al., 2023).

Sodium MRI has a low spatial resolution due to the low in vivo SNR, which makes it less suited for segmentation than proton MRI. When acquiring a different examination for the ^{1}H data, there are potential changes within the organs as a result of a different posture within a different coil and/or physiological differences between the two scans due to e.g. rectal and bladder filling, digestive processes, etc. This can complicate image registration of the ^{1}H and ^{23}Na images, especially in a large field-of-view (FOV). To reduce the potential error of an image registration, acquiring both images in the same examination is favorable. This also saves the increased effort for the patient and the staff of changing to a different radio frequency (RF) coil or even to a different MR scanner.

As there are few commercial ^{23}Na RF coils, especially at 7 T and for application in the torso, many ^{23}Na RF coils are custom-built. As many of these RF antenna designs are ^{23}Na only (Haneder, Kettnaker, et al., 2013; Maril, Rosen, et al., 2006; Platt, Umathum, et al., 2018; Wetterling et al., 2012), ^{23}Na MRI is oftentimes not combined with ^{1}H MRI. Recognizing the importance of anatomical information for localization or segmentation, more dual-nuclei coils were designed in the last years (Moon, Furlan, et al., 2014; Boehmert et al., 2019; Graessl et al., 2015). If external reference vials need to be positioned in the FOV for quantification, the limited space within the bore can be a challenge with a dual-nuclei coil setup. Utilizing a 32-channel pTx coil, placed behind the scanner bore (Orzada, Solbach,

et al., 2019) allows the simultaneous use of the local ^{23}Na RF coil in the here presented setup.

While the SNR increase at ultra-high field strengths benefits ^{23}Na MRI, ^{1}H MRI becomes more challenging. The operational frequency of proton MRI at $B_0 = 7\,\mathrm{T}$ is 297.1 MHz, leading to a wavelength in tissue of about 11 cm, 13 cm and 42 cm for water, muscle and fat, respectively (Gabriel et al., 1996). Due to interference this causes signal dropouts in the transmit field distribution. The homogeneity was improved by utilizing parallel transmit (pTx) (Padormo et al., 2016) and time interleaved acquisition of modes (TIAMO) (Orzada, Maderwald, et al., 2010). For sodium, the operational frequency at $B_0 = 7\,\mathrm{T}$ is about 78.6 MHz, which is comparable to ^{1}H MRI at $B_0 = 1.5\,\mathrm{T}$. Standing waves and interferences do not significantly impact the image quality in this case (Kraff et al., 2015; Platt, Ladd, et al., 2021) and pTx optimization is thus not required.

^{23}Na MRI in the human torso has mostly been focused on a single organ or tissue type such as the kidney (Maril, Rosen, et al., 2006; Haneder, Kettnaker, et al., 2013; Boehmert et al., 2019), the heart (Boehmert et al., 2019; Graessl et al., 2015) or the intervertebral discs (Malzacher et al., 2016; Çavuşoğlu et al., 2022). The utilized local RF coils are customized for one or two specific target anatomies and thus often show a limited anatomic coverage and penetration depth, especially in the case of surface coils. Evaluating more than one target structure without an additional scan is thus often not possible with these coils.

As suggested by R. W. Stobbe et al. (2016), the term apparent tissue sodium concentration (aTSC) was used for the determined in vivo sodium concentration values to take into account that there are not exactly known signal losses from relaxation and pulse sequence characteristics. The setup presented in this thesis enables quantification of the aTSC of organs e.g. in the whole upper torso (heart, lung and abdomen) to compare the quantitative sodium concentrations between different volunteers. For torso MRI, a large FOV is required, especially if several abdominal structures are of interest. Knowledge of the aTSC in healthy volunteers may help to differentiate normal levels of physiological change from changes due to diseases. Monitoring treatment success of chemotherapy in patients with whole body metastases is one potential application of ^{23}Na MRI in a large FOV (Wetterling et al., 2012). Another example is the cardiorenal syndrome, a disorder where the dysfunction of the kidneys induces a dysfunction of the heart or vice versa (Ronco et al., 2008). Acquisition of both organs in a single scan could save scan time and help to better understand the interdependence of both organs. A large FOV also allows to investigate body regions that were not examined yet such

as the pancreas and stomach without performing an additional scan.

The goal of the presented research was the accurate quantification of the aTSC in the human torso at 7 T. For this, a reference vial setup containing external reference vials for concentration quantification was designed and build in-house. As B_1 inhomogeneities within the FOV need to be considered for quantitative ^{23}Na MRI, B_1^+ maps were acquired and B_1^- maps were simulated for the setup to correct the image data. The feasibility of time-resolved quantitative ^{23}Na MRI during a water load experiment was shown, allowing to access the aTSC before, during and after the water load. Large FOV abdominal ^{1}H and quantitative ^{23}Na MRI in the same position at 7 T were combined for the first time. ^{1}H MRI provides anatomical images and B_0 shimming capabilities, while the corrected quantitative ^{23}Na MRI provides insights into physiology. Segmentation of several abdominal structures in the ^{1}H images allows to determine the aTSC in several organs at once.

2 Fundamentals

This chapter provides a brief outline of the fundamental physical and physiological concepts relevant to this thesis. It contains an overview of MR imaging (MRI) in general, special challenges of ^{23}Na MRI and ^{1}H MRI at ultra-high fields and gives an insight into the physiological significance of sodium.

2.1 Magnetic Resonance

The foundation for understanding nuclear magnetic resonance (NMR) effects, which are the basis of image generation in MRI, lies in the fundamental principles of quantum mechanics, electromagnetism, and statistical physics. The subsequent section focuses on the quantum mechanical description of nuclei in an external magnetic field to explain the main aspects of NRM and their influence on MRI. For a detailed mathematical discourse, the classic works of Abragam (1961) and Slichter (1990) should be consulted. Alternatively, Brown et al. (2014) offers a more conceptual explanation. The information presented below is drawn from these sources unless otherwise specified.

2.1.1 Nuclear Spin and Magnetic Moment

Every atom consists out of electrons and a nucleus. The nucleus is composed of protons and neutrons, which are also called nucleons. The NMR characteristics of a nucleus are centrally defined by its nuclear spin and resultant magnetic moment, both determined by the nucleus's composition. The nuclear spin $\hat{\boldsymbol{I}} = (\hat{I}_x, \hat{I}_y, \hat{I}_z)$ is a combination of spin and orbital angular momentum of its constituent nucleons, represented by a quantum mechanical angular momentum operator. For most stable nuclei, the orbital angular momentum L is zero ($L = 0$). The sum of spins for nuclei containing an even number of protons and neutrons adds up to

zero. These nuclei possess no net spin and can thus not be used for MR imaging. However, nuclei with an odd number of neutrons and/or protons are particularly relevant for MR imaging. These nuclei have a non-zero nuclear spin $\hat{\boldsymbol{I}}$, hence exhibiting a magnetic moment $\hat{\boldsymbol{\mu}}_{\boldsymbol{I}}$:

$$\hat{\boldsymbol{\mu}}_{\boldsymbol{I}} = \gamma \hat{\boldsymbol{I}} = \frac{g_I \mu_K}{\hbar} \hat{\boldsymbol{I}} \tag{2.1}$$

where γ is the gyromagnetic ratio, $\hbar$ the Planck constant, g_I the Landé g-factor of the specific nucleus and μ_K the nuclear magneton given by

$$\mu_K = \frac{e\hbar}{2m_p} \tag{2.2}$$

with the rest mass of the proton m_p.

For the quantum mechanical description the nuclear spin $\hat{\boldsymbol{I}}$ fulfills the commutator relations:

$$\left[\hat{I}_i, \hat{I}_j\right] = \epsilon_{i,j,k} \hbar \hat{I}_k \tag{2.3}$$

and

$$\left[\hat{\boldsymbol{I}}^2, \hat{I}_i\right] = 0. \tag{2.4}$$

In the following, the z-axis is used as quantization axis without loss of generality. This leads to the eigenvalue equations:

$$\hat{\boldsymbol{I}}^{\mathbf{2}} \left|I, m_s\right\rangle = \hbar^2 (I+1) I \left|I, m_s\right\rangle \tag{2.5}$$

and

$$\hat{I}_z \left|I, m_s\right\rangle = m_s \hbar \left|I, m_s\right\rangle \qquad\qquad m_s = -I, -I+1, \ldots, I-1, I \tag{2.6}$$

where $|I, m_s\rangle$ is the angular momentum basis with the spin quantum number I and m_s is the magnetic quantum number, which has discrete values between $-I$ and I.

In the absence of an external magnetic field, the states are degenerated $(2I+1)$ times for each spin quantum number I. When an external magnetic field is present, the states are split in dependence to m_s as described in the following section 2.1.2. Hydrogen atoms, which consist of only one proton, are the simplest atomic nucleus

with an odd number of nucleons and have the greatest gyromagnetic ratio of stable in vivo occurring nuclei, while the gyromagnetic ratio of ^{23}Na is only about a quarter of its size (see Table 2.1).

2.1.2 Zeeman Effect

The Zeeman effect emerges from the interaction between the magnetic moment $\hat{\boldsymbol{\mu}}$ and an external magnetic field $\boldsymbol{B}$ at the nucleus location. When a homogeneous static magnetic field $\boldsymbol{B} = B_0\boldsymbol{e_z}$ is applied along the z-axis, the energy states for a nucleus with a nuclear spin I undergo division into $(2I+1)$ equally spaced energy levels along the quantification axis, depending on the magnetic quantum number m_s:

$$E_m = \langle I, m_s | \, \hat{\mathcal{H}} \, | I, m_s \rangle = -\gamma m_s \hbar B_0 \tag{2.7}$$

with the Hamiltonian

$$\hat{\mathcal{H}} = -\hat{\boldsymbol{\mu}}\boldsymbol{B} = -\gamma \hat{I}_z B_0. \tag{2.8}$$

The energy difference between two neighboring states is given by

$$\begin{aligned} \Delta E &= E_m - E_{m+1} \\ &= \frac{1}{2}\hbar\gamma B_0 - \left(-\frac{1}{2}\hbar\gamma B_0\right) = \hbar\omega_0 \end{aligned} \tag{2.9}$$

with the Larmor frequency

$$\omega_0 = \gamma B_0. \tag{2.10}$$

The Larmor frequency is a nucleus-specific quantity depending on the gyromagnetic ratio γ and the applied magnetic field B_0, which describes the frequency at which the magnetic moment of the nucleus precesses in an external magnetic field. The hydrogen atom, with a nuclear spin of $I = 1/2$, exhibits two energy states when subjected to a magnetic field, as illustrated in Figure 2.1. ^{23}Na possessing a nuclear spin of $3/2$ undergoes a division into four energy states, as depicted in the same figure. For all nuclei with spins $I > 1/2$, quadrupole interactions, elaborated further in section 2.1.6, may induce a shift in the split energy states (Figure 2.1).

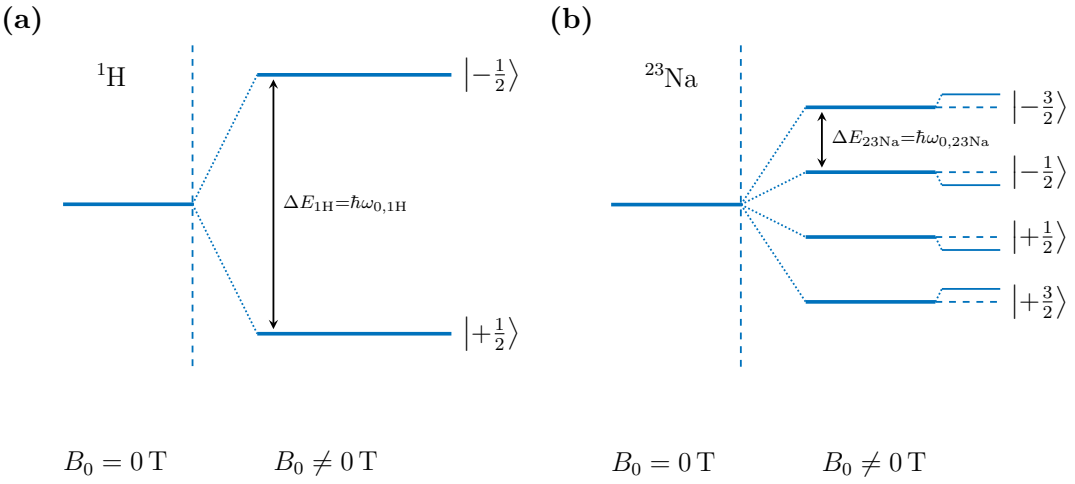

Figure 2.1: Zeeman effect in (a) ^{1}H ($I = 1/2$) and (b) ^{23}Na ($I = 3/2$). The splitting of energy states in an external static magnetic field B_0 into $2I+1$ equidistant energy level with an energy difference of $\Delta E = \hbar\omega_0$ is depicted. For ^{23}Na , the dashed lines indicate the energy levels without quadrupole interactions for the $\pm 1/2$ and the $\pm 3/2$ states. When considering quadrupole interactions (see section 2.1.6), the energy levels are shifted proportional to m_s^2 as indicated by the solid lines.

2.1.3 Macroscopic Magnetization

In thermal equilibrium and with $\boldsymbol{B} \neq 0$, the occupation numbers of energy levels adhere to a Fermi-Dirac statistic due to the fermionic nature of both ^{1}H and ^{23}Na. In the high-temperature regime, which is typically fulfilled in clinical NMR experiments, the probability of a certain state being occupied can be approximated by a Boltzmann distribution. For an energy level E_m, the probability of occupation p_m can be expressed as:

$$p_m = \frac{1}{Z} \cdot \mathrm{e}^{-\frac{E_m}{k_B T}} = \frac{1}{Z} \cdot \mathrm{e}^{\frac{\gamma \hbar m_s B_0}{k_B T}} \tag{2.11}$$

with

$$Z = \sum_{m_s=-I}^{I} \mathrm{e}^{\frac{\gamma \hbar m_s B_0}{k_B T}} \tag{2.12}$$

with the Boltzmann constant k_B, the absolute temperature T and the canonical partition function Z, which is used as a normalization factor. NMR experiments detect the state of macroscopic sample volumes given as the superposition of all

magnetic moments in the sample, motivating the introduction of the macroscopic magnetization across a spin ensemble to allow a semi-classical description. The macroscopic magnetization $\boldsymbol{M_0}$ of an object with N spins equals the expectancy value of the magnetic moments $\hat{\boldsymbol{\mu}}_{\boldsymbol{i}}$ per volume V:

$$\boldsymbol{M_0} = \frac{1}{V}\sum_{i=1}^{N}\langle\hat{\boldsymbol{\mu}}_{\boldsymbol{i}}\rangle = \frac{1}{V}\sum_{i=1}^{N}\gamma\cdot\left\langle\hat{\boldsymbol{I}}_{\boldsymbol{i}}\right\rangle. \tag{2.13}$$

In thermal equilibrium the magnetization is parallel to the external magnetic field ($\boldsymbol{M} = (0,0,M_0)^T$). Utilizing the high-temperature approximation $k_BT \gg E_m$, which is valid at room and body temperature, the first-degree Taylor expansion of p_m yields

$$M_0 \approx \frac{N}{V}\gamma^2 B_0 \frac{\hbar^2 I(I+1)}{3k_BT}. \tag{2.14}$$

The ratio N/V is also referred to as spin density ρ. Since the temperature of the human body should remain nearly constant during an NMR measurement, the use of a cryoprobe to cool the sample is not possible. To enhance the macroscopic magnetization M_0 in vivo for nuclei with low spin density, other techniques such as enriching the sample or designing sensitivity enhancing pulse sequences are employed (Zhuang et al., 2023). Alternatively, the magnetic field strength B_0 can be increased, which is one explanation for the trend towards higher magnetic field strengths in MR scanners.

2.1.4 Excitation of Spins

The system is assumed to be in thermal equilibrium with a macroscopic magnetization $\boldsymbol{M_0} = (0,0,M_0)^T$ aligned parallel to an external magnetic field $\boldsymbol{B} = (0,0,B_0)^T$. To detect a signal from the magnetization, it must first be tipped out of its equilibrium position. This is achieved by applying a radio frequency (RF) alternating magnetic field $\boldsymbol{B_1}(t)$ (also called RF pulse) perpendicular to the static magnetic field $\boldsymbol{B_0}$ with a frequency ω_{RF} corresponding to the Larmor frequency ω_0 of the imaged nuclei (see Table 2.1), for a duration τ using a transmit RF coil. This field, often referred to as the transmit ($\boldsymbol{B_1^+}$) field, can be described as

$$\boldsymbol{B_1}(t) = \begin{pmatrix} B_1(t)\cos(\omega_{\mathrm{RF}}t) \\ B_1(t)\sin(\omega_{\mathrm{RF}}) \\ 0 \end{pmatrix}. \tag{2.15}$$

This field induces a tilt in the macroscopic magnetization $\boldsymbol{M}$, generating a non-zero component of magnetization in the xy-plane, known as the transverse magnetization $M_\perp$, which precesses around the z-axis of the reference system at the Larmor frequency $\omega_0 = \gamma B_0$. Assuming a circularly polarized $\boldsymbol{B_1}$ field the equation of motion of the macroscopic magnetization during excitation becomes

$$\frac{\mathrm{d}\boldsymbol{M}(t)}{\mathrm{d}t} = \gamma \boldsymbol{M} \times \boldsymbol{B}(t) = \gamma \boldsymbol{M} \times \begin{pmatrix} B_1(t)\cos(\omega_{\mathrm{RF}} t) \\ B_1(t)\sin(\omega_{\mathrm{RF}}) \\ B_0 \end{pmatrix}. \tag{2.16}$$

In a reference system rotating with angular frequency ω_{RF} around the z-axis, the precession of the magnetization and the time dependence of the RF field transform such that the apparent precession frequency of the magnetization is reduced by ω_{RF}. Equation 2.16 becomes

$$\frac{\mathrm{d}\boldsymbol{M'}(t)}{\mathrm{d}t} = \gamma \boldsymbol{M'}(t) \times \begin{pmatrix} B_1(t) \\ 0 \\ B_0 - \frac{\omega_{\mathrm{RF}}}{\gamma} \end{pmatrix} = \gamma \boldsymbol{M'}(t) \times \boldsymbol{B}_{\mathrm{eff}} \tag{2.17}$$

for a B_1, without loss of generality, chosen parallel to the x'-axis. During a resonant excitation with $\omega_{\mathrm{RF}} = \omega_0 = \gamma B_0$, the effective magnetization is $\boldsymbol{B}_{\mathrm{eff}} = (B_1, 0, 0)$ pointing along the x'-axis. As a result, the magnetization rotates around the x'-axis in the rotating frame of reference. Neglecting relaxation during the RF pulse, the rotation angle is:

$$\alpha = \int_{t=0}^{\tau} \gamma B_1(t)\mathrm{d}t. \tag{2.18}$$

In NMR experiments, α is usually referred to as the flip angle. For a rectangular excitation pulse $B_1(t) = B_1$ is constant during the pulse duration, resulting in a flip angle of

$$\alpha = \gamma B_1 \tau. \tag{2.19}$$

Rectangular pulses are frequently used in X-nuclei MRI to tilt the magnetization into the transverse plane (x'y'-plane, 90°-pulse) or to invert it (180°-pulse).

2.1.5 Relaxation of Spin-1/2-Nuclei

Another important characteristic of a spin ensemble is its relaxation towards thermal equilibrium, which was omitted in the previous considerations on excitation and signal formation. This relaxation results from inter- and intramolecular spin interactions and is crucial for contrast formation in experimental measurements. For spin = 1/2 nuclei, the differential equation for the magnetization in the presence of a magnetic field is an empirical vector equation referred to as the *Bloch equation* (Bloch, 1946):

$$\frac{\mathrm{d}\boldsymbol{M}(t)}{\mathrm{d}t} = \gamma \boldsymbol{M}(t) \times \boldsymbol{B}(t) - \frac{M_{\parallel}(t) - M_0}{T_1}\boldsymbol{e_z} - \frac{\boldsymbol{M}_{\perp}}{T_2}. \tag{2.20}$$

When solving this equation for the laboratory system with a magnetic field strength of $\boldsymbol{B} = (0, 0, B_0)$, the time evolution of the longitudinal component $M_{\parallel}$ after an RF pulse can be described as

$$\begin{aligned} M_{\parallel}(t) &= M_{\parallel}(t_0) \cdot \mathrm{e}^{-\frac{t}{T_1}} + M_0 \cdot \left(1 - \mathrm{e}^{-\frac{t}{T_1}}\right) \\ &= M_0 \cdot \left(\cos(\alpha) \cdot \mathrm{e}^{-\frac{t}{T_1}} + 1 - \mathrm{e}^{-\frac{t}{T_1}}\right) \end{aligned} \tag{2.21}$$

with the relaxation time T_1. The relaxation of the transverse component $M_{\perp}$ is an exponential decay

$$M_{\perp}(t) = M_{\perp}(t_0) \cdot \mathrm{e}^{-\frac{t}{T_2}} \tag{2.22}$$

with the relaxation time T_2.

These equations provide independent exponential relaxations of both $M_{\parallel}$ and $M_{\perp}$. The macroscopic magnetization precesses around the external magnetic field B_0, with the longitudinal part $M_{\parallel}$ relaxing to the equilibrium state with the relaxation time T_1, while the transverse component $M_{\perp}$ relaxes with the relaxation time T_2.

The longitudinal relaxation, also called spin-lattice-relaxation is explained by the Bloembergen-Purcell-Pound (BPP) theory. This theory attributes the effect to fluctuating magnetic fields caused by thermal rotational and translational movements of surrounding molecules (Bloembergen et al., 1948). This process involves the transfer of energy from the spin system to the lattice, resulting in the longitudinal magnetization $M_{\parallel}$ reverting to the equilibrium state. In human tissue, T_1 usually ranges from tens to thousands of milliseconds for protons depending on the B_0 field strength used.

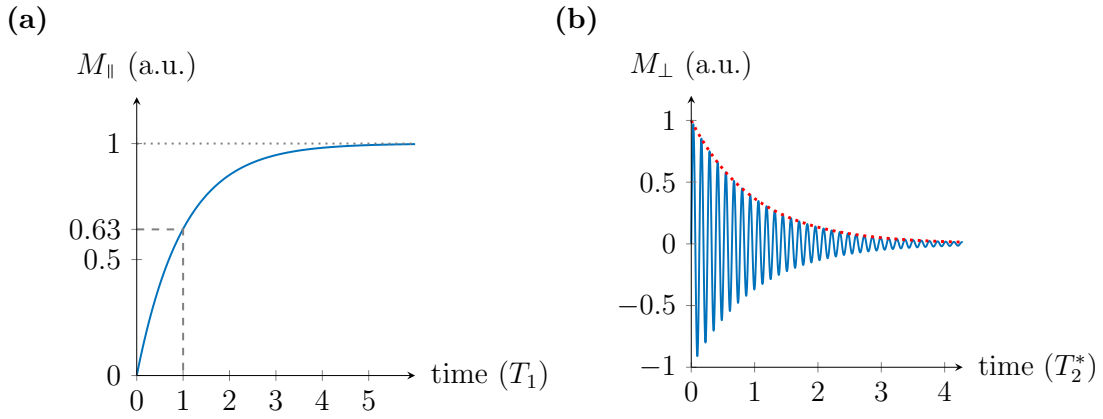

Figure 2.2: Time series of the magnetization after an excitation with $\alpha = 90°$. The relaxation of the longitudinal magnetization $M_\parallel$ into the thermal equilibrium is depicted in (a). In (b) the oscillation of the transverse magnetization $M_\perp$ with the Larmor frequency ω_0 is shown. The envelope (red line) of the transverse magnetization is an exponential decay with the relaxation time T_2^*.

The transverse relaxation time T_2 (spin-spin relaxation) is the result of irreversible dipole-dipole interactions between spins, and it is defined as the time at which the dephasing of a magnetic resonance signal falls to $1/e$ (37 %) of its initial value after a 90° RF pulse. Immediately after the stimulation, the spins are in phase coherence, which is then decaying exponentially. This dephasing occurs due to energy exchange between rotating spins driven by local B_0 fluctuations, which are caused by random atomic movements. These fluctuations alter the local Larmor frequency, causing spins rotating at different speeds to lose phase coherence. While the mentioned dipole-dipole interactions are the dominant form of dephasing in spin-$1/2$-nuclei, quadrupole nuclei ($I > 1/2$) introduce additional interactions, which are discussed in more detail in section 2.1.6. The T_2 times are practically frequency independent over the field strengths used in clinical setups (up to 3 T) as predicted by the dipole-dipole interaction model of Bloembergen Purcell and Pound, but are shorter at ultra-high fields due to different effects being accentuated (Graaf et al., 2006). Typically, T_2 times for protons in almost all human tissue amount to tens of milliseconds. The T_2 values in solids are typically in the order of microseconds and therefore much shorter than for liquids, where they are in the order of seconds.

Furthermore, time-independent B_0 inhomogeneities (ΔB_0) accelerate the transverse decay. These inhomogeneities can be a result of susceptibility differences

in the examined object or fluctuations in the initial magnetization, resulting in varying spin precession. The spatial distribution of B_0 leads to a spatially varying distribution of Larmor frequencies, thereby causing a phase distribution. The differing spin precessions result in a rapid decline of the transverse magnetization with the effective relaxation time T_2^*, which is smaller than T_2:

$$\frac{1}{T_2^*} = \frac{1}{T_2} + \frac{1}{T_2'} = \frac{1}{T_2} + \gamma \Delta B_0 \tag{2.23}$$

where T_2' is an additional relaxation time depending on the local, time independent B_0 inhomogeneities ΔB_0. After a resonant excitation pulse, the signal is a damped oscillation with the Larmor frequency (Figure 2.2) called free induction decay (FID). The T_2^* time is characteristic for the envelope of an FID-signal. Typical T_2' values are in the order of tens of milliseconds (Brown et al., 2014).

2.1.6 Relaxation of Spin-3/2-Nuclei

The so far considered spin-$^1/_2$-nuclei relax mainly due to magnetic interactions. As all NMR relevant nuclei with $I > {}^1/_2$, the sodium nuclei ($I = {}^3/_2$) has an additional electrical quadrupole moment Q. The charge distribution of the nucleus thus differs from the spherical symmetry of spin-$^1/_2$-nuclei, enabling an additional spin interaction with the electrical fields generated near the nuclei. The electrical relaxation is oftentimes several orders of magnitude higher than the magnetical relaxation and thus dominant (Werbelow, 2011). For this reason, relaxation times of nuclei with quadrupole moments are in general significantly shorter than those of ^{1}H .

For the electrical interactions, the transverse and longitudinal part can be expressed as a sum of exponential functions. For nuclei with an integer spin quantum number I, the sum also has I components. For half-integer spins the resulting sum has $I + {}^1/_2$ elements. This implies $({}^1/_2 + {}^1/_2 = 1)$ elements in the exponential function for $I = {}^1/_2$ nuclei and $({}^3/_2 + {}^1/_2 = 2)$ elements for $I = {}^3/_2$ nuclei. Therefore, the relaxation process for spin-$^1/_2$-nuclei such as ^{1}H is mono-exponential while nuclei such as ^{23}Na with a spin of $I = {}^3/_2$ have a bi-exponential relaxation (Hubbard, 1970). The bi-exponential character of the longitudinal and transverse relaxation

of a spin-$^3/_2$-system can be expressed by modifying equations 2.21 and 2.22:

$$\begin{aligned} M_{\parallel}(t) =& M_{\parallel}(t_0) \cdot \left(0.8 \cdot \mathrm{e}^{-\frac{t}{T_{1s}}} + 0.2 \cdot \mathrm{e}^{-\frac{t}{T_{1l}}}\right) \\ &+ M_0 \cdot \left(1 - 0.8 \cdot \mathrm{e}^{-\frac{t}{T_{1s}}} + 0.2 \cdot \mathrm{e}^{-\frac{t}{T_{1l}}}\right) \end{aligned} \tag{2.24}$$

$$M_{\perp}(t) = M_{\perp}(t_0) \cdot \left(0.6 \cdot \mathrm{e}^{-\frac{t}{T_{2s}}} + 0.4 \cdot \mathrm{e}^{-\frac{t}{T_{2l}}}\right) \tag{2.25}$$

where T_{1s} and T_{1l} are the short and the long component of the longitudinal relaxation contributing 80 % and 20 %, respectively and T_{2s} and T_{2l} are the short and the long component of the transverse relaxation contributing 60 % and 40 %, respectively for a single compartment. In the case of ^{23}Na in the human brain, the relaxation times at 7 T amount to (5.5 ± 1.3) ms and (29.3 ± 3.8) ms for the short and the long component of the bi-exponential transverse decay in white matter, respectively (Kratzer et al., 2021). In the calf muscle, Lott, Platt, et al. (2019) found $T_{2s}^* = (26.6 \pm 2.9)$ ms and $T_{2l}^* = (3.0 \pm 0.1)$ ms. This is short compared to the relaxation times of ^{1}H , which are around 80 ms and 110 ms for gray matter and white matter at 3 T, respectively (Wansapura et al., 1999).

In fluids, such as blood or cerebrospinal fluid, a mono-expontial transverse relaxation is observed. This behavior can be attributed to the fact that the relaxation and decay characteristics rely on the correlation time τ_c, which is characterizing the random fluctuation of the electrical field gradients (direction and / or orientation). For the limiting case of a short correlation time ($\omega_0 \tau_c \leq 1$), as for example valid in fluids, the relaxation is showing a mono-exponential behavior ($T_{2s} = T_{2l}$). A detailed theoretical explanation can be found in Maarel (2003) and Jaccard et al. (1986).

2.1.7 Specific Absorption Rate

The applied RF energy of an excitation pulse during an MRI acquisition can be deposited in the body as heat, thus rising the tissue temperature. As even a temperature increase of a few degrees can cause damage to the tissue, the International Electrotechnical Commission (IEC) defined limits for the maximal core body temperature, the maximal core body temperature increase and the maximal tissue temperature. Since the tissue temperature can not be directly measured during an MR measurement, the specific absorption rate (SAR) is used.

The specific absorption rate measures the amount of power deposited by an RF

field in a certain mass of the imaged object. By limiting the SAR during an MRI scan, consequentially the RF induced heating of the tissue is limited. The SAR is limited by the IEC-guidelines (IEC. 60601-2-33:2022) for the whole body, partial body and for a mass of 10 g for a 10 s and 6 min average and is given by

$$SAR = \frac{1}{2V} \int_V \frac{\sigma(\boldsymbol{r})}{\rho(\boldsymbol{r})} |\boldsymbol{E}(\boldsymbol{r})| \mathrm{d}\boldsymbol{r} \tag{2.26}$$

where σ is the electrical conductivity and ρ the mass density of the tissue. For volume coils, only the whole body and partial body SAR are limited (Platt, 2018). If either the 10 s or the 6 min limit is reached, the measurement is stopped. While the calculation of SAR in human subjects is very complex, a simplified model with only one RF pulse can be used to illustrate the dependencies of SAR on different measurement parameters (Reiser et al., 2008). In this case, the time-averaged SAR can be approximated as

$$SAR \propto B_0^2 \cdot \alpha^2 \cdot \frac{\tau}{T_R} \tag{2.27}$$

where B_0 is the static magnetic field strength, α is the flip angle, τ is the pulse duration and T_R is the repetition time (time between two excitation pulses). This equation is only valid for small frequencies (up to 80 MHz in a sphere of uniform electrical conductivity) as e.g. T. M. Fiedler et al. (2018) show a less than quadratic increase in local SAR with B_0.

With rising magnetic field strengths, the RF energy to achieve a specific flip angle has to be increased. As this leads to a potentially larger tissue heating, sequence parameters or the excitation scheme are altered to ensure safe measurements by reducing the applied RF energy and thus SAR. For a fixed flip angle α, the pulse voltage U_P of a rectangular pulse is decreasing inversely proportional with the pulse duration. As the specific absorption rate depends quadratically on the pulse voltage, the mean administered RF energy and hence the mean SAR can for example be reduced by prolonging the pulse duration τ.

Commercially available MR scanners are equipped with safety supervision that estimates the SAR values for the selected imaging protocol and weight of the volunteer or patient and suggests changes to the imaging settings if the SAR limits are expected to be exceeded. During the measurement, the applied power is measured in real time and the measurement is aborted if the SAR limits are exceeded.

For parallel transmit (see section 2.4.1), local SAR needs to be considered in order to take heating in small areas into account that results from the spatially and

temporally variable total electric field. The required knowledge of the electric fields for the local SAR estimation is typically provided by electromagnetic field simulations in digital body models.

For ^{1}H imaging performed in the context of this research work, the SAR was limited by limiting the input power per channel. Therefore, a custom safety supervision system as described by T. Fiedler et al. (2024) was used, which automatically shuts off if any of the 32 channels exceeds the 10 s or 6 min power limit for the torso. The power limits were predefined according to electromagnetic field simulations.

2.2 MR Imaging

This section covers the fundamentals of signal acquisition and imaging. A detailed depiction can be found in the works of Bernstein et al. (2004), Brown et al. (2014) and Reiser et al. (2008). The physical characteristics of the sodium nucleus cause special challenges for MR imaging, that are further discussed in section 2.3. The particularities of MRI at ultra-high fields will be the focus of section 2.4.

2.2.1 Signal and Signal Strength

As described in section 2.1.4, an RF pulse is used to tip the magnetization out of its resting position, causing it to precess in the external magnetic field with the Larmor frequency. The electromagnetic induction this precession causes in a receive coil can then be detected. The induced voltage or electromotive force can be computed from Faraday's law of induction:

$$U_{\mathrm{ind}} = -\frac{\mathrm{d}\Phi_m}{\mathrm{d}t} \qquad \Phi_m = \int_S \boldsymbol{B}\mathrm{d}\boldsymbol{S} \tag{2.28}$$

where Φ_m is the magnetic flux and, in case of a loop coil, $\boldsymbol{S}$ is the observed coil surface. The time-dependent form of this holds the information that can be translated into an image of the investigated object. In order for the electromotive force to be non-vanishing, the magnetic flux through a surface with a normal component perpendicular to the magnetic field has to change over time, and a conducting loop must enclose this varying flux to induce a voltage. The strength

Table 2.1: NMR properties of the most widely used nuclei in MRI (Harris et al., 2001). The nuclear spin I, the gyromagnetic ratio γ, the natural abundance n, the relative receptivity $\mathcal{R}$ in relation to $\mathcal{R}_{^1\mathrm{H}}$ of ^{1}H and the resonance frequency f_0 at 1 T are listed.

nucleus	I ($\hbar$)	$\gamma/10^7$ (rad T^{-1} s^{-1})	n (%)	$\mathcal{R}$ (rel. to $\mathcal{R}_{^1\mathrm{H}}$)	f_0 at 1 T (MHz)
^{1}H	1/2	26.7522	99.99	1	42.6
^{13}C	1/2	6.7283	1.07	1.7×10^{-4}	10.7
^{17}O	5/2	−3.6281	0.04	1.1×10^{-5}	5.8
^{19}F	1/2	25.1815	100	8.34×10^{-1}	40.1
^{23}Na	3/2	7.0801	100	9.27×10^{-2}	11.3
^{31}P	1/2	10.8394	100	6.65×10^{-2}	17.3
^{35}Cl	3/2	2.6242	75.78	3.58×10^{-3}	4.2
^{39}K	3/2	1.2501	93.26	4.76×10^{-4}	2.0

of a specific MR signal S is given by

$$S \propto (\Delta x)^3 \gamma^3 B_0^2 \cdot \rho \cdot I(I+1). \tag{2.29}$$

Here, $\rho = N/V$ describes the spin density, I the nuclear spin and B_0 the static magnetic field. The spin density depends on the natural abundance of the measured nucleus and the concentration in the imaged tissue (see Table 2.1). Due to their smaller gyromagnetic ratio γ and spin density ρ compared to ^{1}H, X-nuclei generate smaller signal amplitudes. When comparing the relative receptivity of different X-nuclei in Table 2.1, ^{19}F exhibits values very close to those of ^{1}H. Due to the physiological concentrations of detectable mobile fluorine being below the detection limits, endogenous ^{19}F MRI signal from the body is negligible. Therefore, ^{23}Na is the nucleus with the second largest in vivo NMR signal after ^{1}H when excluding the use of tracers. Section 2.3 provides more details on this topic and ^{23}Na MRI in general.

2.2.2 Spatial Encoding and k-space

Identical nuclei in locations with changed magnetic fields precess with different Larmor frequencies, which allows to spatially resolve the signal from the magne-

tization in a sample. Usually a combination of frequency and phase encoding is used to differentiate between voxels (volume elements).

For frequency encoding, a linear time- and location-dependent varying magnetic field $\boldsymbol{r}\boldsymbol{G}(t)\boldsymbol{e_z}$, called a gradient field, is superimposed onto the homogeneous static magnetic field $\boldsymbol{B_0} = (0, 0, B_0)$. This leads to a total magnetic field of

$$\boldsymbol{B}(\boldsymbol{r}, t) = \boldsymbol{B_0} + (\boldsymbol{r} \cdot \boldsymbol{G}(t) \cdot \boldsymbol{e_z}) \qquad \text{with } \boldsymbol{G}(t) = \begin{pmatrix} \partial_x B_G(t) \\ \partial_y B_G(t) \\ \partial_z B_G(t) \end{pmatrix} \tag{2.30}$$

at position $\boldsymbol{r} = (x, y, z)$. This changes the local Larmor frequency to

$$\omega_0(\boldsymbol{r}, t) = \gamma(B_0 + \boldsymbol{r} \cdot \boldsymbol{G}(t)). \tag{2.31}$$

The location dependency of the Larmor frequency can be used to either differentiate locations within a slice or for a process called slice selection, where a specific slice is excited.

For slice selection, an RF pulse is applied which only excites magnetization within a specific frequency band, called the bandwidth $\Delta\omega_{\mathrm{RF}}$. For a gradient G_{slice} in z-direction and a given bandwidth, a slice with a thickness of

$$\Delta z = \frac{\Delta\omega_{\mathrm{RF}}}{G_{\mathrm{slice}}\gamma} \tag{2.32}$$

is excited.

To achieve another encoding direction, e.g. in the y-direction, phase encoding is utilized where the gradient $\boldsymbol{G}$ is applied during a time T before the readout of the signal. Temporarily applying a gradient results in a temporary spatially-dependent Larmor frequency. The at different frequencies precessing spins thus accumulate a different phase depending on their y-position. After the gradient is turned off, the frequencies are the same again while the phase is preserved. If frequency encoding is now applied in x-direction during the readout of the signal, the resulting signal is a superposition of different location-dependent Larmor frequencies according to equation 2.31. The information on the position from the frequency and phase of the magnetization in each voxel can be used to allocate the signal origin $\boldsymbol{r}$ unambiguously.

The 3D k-space, also called momentum space, is sampled in a discrete manner by using the gradients $\boldsymbol{G}(t)$ to creating a suitable trajectory. The measured signal

in k-space is comprised of the frequency and phase information of the transverse magnetization. The spatially resolved signal in the image space can be obtained by an inverse Fourier. The measured signal $S(\boldsymbol{k}(t), t)$ when omitting relaxation is given as

$$S(\boldsymbol{k}(t), t) \propto \int M_{\perp}(\boldsymbol{r}, t) \mathrm{e}^{-2\pi i \boldsymbol{k}(t)\boldsymbol{r}} \mathrm{d}\boldsymbol{r} \tag{2.33}$$

where $\boldsymbol{k}(t)$ is the wave vector

$$\boldsymbol{k}(t) \coloneqq \frac{\gamma}{2\pi} \int_0^t \boldsymbol{G}(t') \mathrm{d}t' \tag{2.34}$$

resulting in a phase $\phi(\boldsymbol{r}, t)$ of

$$\phi(\boldsymbol{r}, t) = \gamma \boldsymbol{r} \int_0^t \boldsymbol{G}(t') \mathrm{d}t' = 2\pi \boldsymbol{r} \boldsymbol{k}(t). \tag{2.35}$$

The transverse magnetization $M_{\perp}$ can be calculated from equation 2.33 by an inverse Fourier transform:

$$M_{\perp}(\boldsymbol{r}) \propto \int S(\boldsymbol{k}(t), t) \mathrm{e}^{+2\pi i \boldsymbol{k}(t)\boldsymbol{r}} \mathrm{d}\boldsymbol{k}. \tag{2.36}$$

In order to reconstruct the complex signal, a sufficiently sampled k-space is needed. This so called k-space coverage depends on the switching of gradient fields of different strength and duration which determine the trajectory and density of sampled data points in k-space. In section 2.2.3 the adequate sampling density is determined in more depth.

The data to fill k-space can be acquired in any order as long as the k-space coverage is sufficient. Depending on the application, the readout trajectory can vary, with the three exemplary forms cartesian, center-out radial and spiral being shown in Figure 2.3. For clinical uses, cartesian readout schemes are most common. In 2D imaging, each k-space row corresponds to the data obtained from a single application of the phase encoding gradient before and a frequency encoding gradient during readout. Here frequency encoding is only performed in one direction, while it is applied in all directions for radial and spiral imaging schemes. The density of coverage of the acquired k-space in cartesian imaging methods can be chosen uniformly. In radial sequences the density of coverage is higher in the k-space center and decreases with distance from the origin (Figure 2.3).

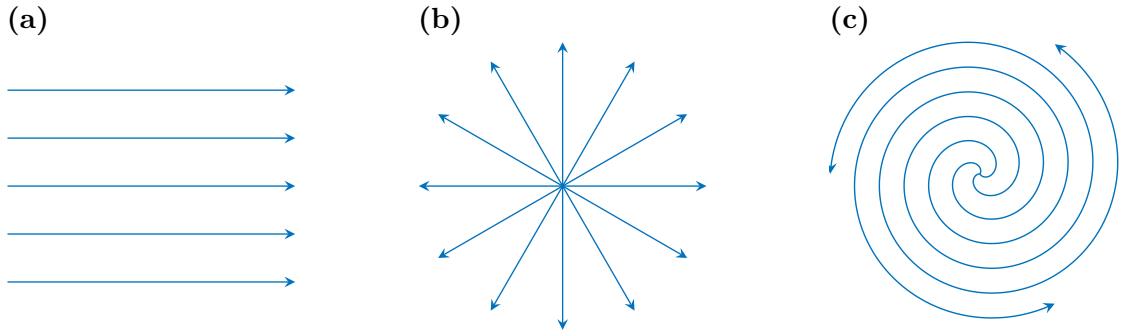

Figure 2.3: Exemplary readout trajectories for data acquisition in k-space. The shown 2D readout techniques for 2D acquisition are (a) cartesian, (b) radial center-out and (c) spiral trajectories. The arrows show the readout direction.

Sampling density in different parts of k-space have an influence on the image quality. Lower frequencies that are close to the k-space center form the general structure and the image contrast. Higher frequencies in the k-space peripheries give detailed and fine structures. Image parameters such as the spatial resolution and the FOV determine the size of the sampled k-space.

The pulse sequence for ^{23}Na MRI used in the context of the here presented research work is based on radial readout trajectories and is described in detail in section 3.2.1.2. The advantages of a radial acquisition for ^{23}Na MRI is discussed in section 2.3. As artifacts from moving structures do not propagate along a single phase encoding direction, but are spread more diffusely across the whole image for radial sampling, a radial readout scheme has a lower intrinsic sensitivity to motion compared to cartesian sampling. This is advantageous for MRI of the torso where artifacts from respiratory and cardiac motion can be reduced leading to improved image quality.

Reconstruction of the radially sampled image can not simply be performed by a fast Fourier transform. Advanced implementations and reconstruction algorithms are needed to for example perform a regridding of the data before reconstruction or use a nonuniform fast Fourier transform. Details on the adopted imaging sequence for ^{23}Na MRI can be found in section 3.2.1.2, while the reconstruction is explained in more detail in section 3.3.1.

2.2.3 Nyquist Criterion

A sufficiently filled k-space is needed in order to reconstruct an adequate image. The measured data is filling k-space in a discrete manner. This results in the characteristics of the discrete Fourier transform from equation 2.36 to influence the properties of the resulting image. Mathematically, the discrete sampling of the continuous signal can be described as a convolution with a periodic sequence of δ-functions (Dirac comb). The Fourier transform of the Dirac comb function is a periodic function with reciprocal distances. The measured image is thus repeating periodically with $1/\Delta k_{\max}$. Considering data that was measured with uniform spacing of distances $\Delta k_{\max}$ between data points, the spatial interval over which the reconstructed image repeats itself is called field-of-view (FOV):

$$FOV = \frac{1}{\Delta k_{\max}}. \tag{2.37}$$

One of the copies is chosen when an image is reconstructed. In case of a FOV that is too small for the size of the imaged object, the images overlap and cause aliasing artifacts, folding image content from outside the FOV back into the reconstructed image. To reconstruct the FOV without artifacts, the Nyquist criterion can be applied. The nominal resolution of the MR image Δx:

$$\Delta x = \frac{1}{2k_{\max}} \tag{2.38}$$

depends on the k-space position furthest away from the center ($k_{\max}$).

The term undersampled is used to describe data that does not satisfy the Nyquist criterion, while oversampling is used to describe data that more than satisfies the Nyquist criterion. The undersampling factor (USF) of a given sequence quantifies the level of undersampling. For radial trajectories it is defined as the ratio

$$\mathrm{USF} = \frac{N_{\mathrm{Nyquist}}}{N_{\mathrm{Sequence}}} \tag{2.39}$$

of the number of projections needed for an artifact-free reconstruction N_{Nyquist} and the number of projections used in the given sequence N_{Sequence}.

For a radial imaging scheme, the outermost points on the trajectories in k-space form a sphere with a radius $(\Delta k)_{\max}$. To get adequate radial sampling for large k, smaller k-values are oversampled. The total acquisition time for radial sampling is thus a factor of $\pi/2$ longer compared to cartesian sampling. While the longer

scan time is a drawback, the extra points translate to a better signal-to-noise ratio (see section 2.2.6) for a sub-region of sampled points. Section 3.2.1.2 discusses a density adapted radial sequence, which reduces the oversampling of central k-space. The Nyquist criterion for radial imaging gives the number of projections that are needed for an artifact-free reconstruction:

$$N_{\text{Nyquist}} \geq 4\pi \left(\frac{FOV}{2\Delta x} \right)^2 . \tag{2.40}$$

Radial undersampling causes noise-like artifacts, posing a much smaller problem compared to the aliasing artifacts in cartesian sampling. Therefore a higher USF can be used for radial sampling. This is for example useful when image data is sorted into different subsets before reconstruction as for example done in section 4.3.1 for a time course during a water load experiment.

2.2.4 Pulse Sequences

A pulse sequence is the combination of RF excitations and gradients. The two main sequences are the spin echo sequence (SE) and the gradient echo sequence (GRE).

The spin echo sequence begins with a slice selection gradient and a SINC pulse to flip the magnetization by 90°. As the FT of a SINC pulse is a rectangular pulse, this is the shape of the RF pulse in the frequency domain. The entire selected slice is thus excited with the same flip angle α. A phase encoding gradient changes the phase along one axis of the slice for spatial encoding as described in section 2.2.2. To reverse the dephasing effect of the T_2^* decay a second RF pulse with a flip angle of 180° is applied at $T_E/2$. This leads to a rephasing of the excited spins that form an echo at the time T_E , which is thus called echo time, after the initial RF pulse. Utilizing a gradient field for frequency encoding, a complete line in k-space can be acquired. Before repeating this sequence for another line in k-space, the magnetization has to decay back to its ground state. The time between two consecutive 90° pulses is called repetition time T_R. By adjusting T_E , T_R and α of the RF pulse, different imaging contrasts can be obtained (see section 2.2.5).

The gradient echo sequence is similar to the described SE sequence but does not utilize the second RF pulse to rephase the excited spins. Because only one RF pulse is applied, the echo can be recorded much more quickly in a GRE sequence and T_E is thus generally shorter for GRE sequences than for SE sequences.

Table 2.2: Summary of the main rules for generating the most widely used tissue contrasts (Table adapted from Brown et al. (2014)).

Type of contrast	T_R	T_E
spin density	$\sim 5\ T_1$	$\ll T_2^*$
T_1-weighted	in the order of the T_1 values	$\ll T_2^*$
T_2-weighted	$\sim 5\ T_1$	in the order of the T_2-values

2.2.5 MRI Contrasts

An MR image can have a variety of contrasts depending on the imaging parameters such as echo time, repetition time or the flip angle. Most widely used image weightings are spin density, T_1- and T_2-weighting. Depending on the chosen image weighting type, the distinct relaxation characteristics and spin densities of different tissue types are contributing in a particular way to the signal intensity.

For a spin echo sequence as described in section 3.2, a long T_R minimizes T_1 effects, as all imaged tissues have the time to fully recover in between the excitations. A short T_E minimizes the T_2 effects, as the differences in the T_2 decay only have a short time to appear. As a result, the image contrast is mainly determined by the spin density ρ for minimized T_2 and T_1 effects when $T_E \ll T_2^*$ and $T_R \gg T_1$.

For a T_1-weighting, T_2^* effects are minimized by using a short T_E paired with a short T_R ($T_R < T_1$). In this case, tissues with short T_1 times contribute more to the signal intensity than tissue with long T_1 times. The effects of spin density differences can not be entirely neglected. To optimize the T_1 contrast, a priori knowledge of the tissue properties of the imaged object can help to choose an appropriate relaxation time.

For a T_2-weighted image, the effects of T_1 relaxation are kept small by choosing a long T_E and T_R time. An overview over the different imaging contrasts and the needed T_R and T_E times are listed in Table 2.2.

In practice, the minimum T_E is mainly restricted by the required pulse duration, which is in turn restricted by SAR limitations (see section 2.1.7). The maximal feasible T_R is limited by measurement time and imaging efficiency. Furthermore, almost all images have varying contributions from all of the different tissue parameters (T_1, T_2, ρ, diffusion, susceptibility, chemical shift, flow, perfusion), causing

all MR images to contain a variety of image contrasts.

For quantitative X-nuclei MRI, spin density weighted images are often preferred as they enable the quantitative determination of the sodium concentration.

2.2.6 Signal-to-Noise Ratio

The signal-to-noise ratio (SNR) is, together with the image contrast, an important quality standard in many experiments to for example compare different imaging techniques. It is defined as follows:

$$\mathrm{SNR} = \frac{\mathrm{signal}}{\mathrm{noise}} \tag{2.41}$$

where the noise is comprised of the noise from the electronics as well as the sample volume. In clinical MRI, the noise is dominated by inductive losses and is assumed to rise linearly with the Larmor frequency for volume RF coils and large samples. Electrical noise is created through the thermal movements of charged particles, but can be neglected in most large volume coils, since the noise is dominated by the sample.

The SNR shows the following proportionalities:

$$SNR \propto \Delta x \cdot \Delta y \cdot \Delta z \cdot \rho \cdot \gamma^{2 \text{ to } 2.75} \cdot B_0^{1 \text{ to } 1.75} \cdot I(I+1) \tag{2.42}$$

where Δx, Δy and Δz are the edge lengths of the chosen voxel. These dependencies are similar to the NMR sensitivity in equation 2.29, but considering noise reduced the proportionality on B_0 and the gyromagnetic ratio γ. Ladd et al. (2018) for example discussed the dependencies of SNR on γ and B_0 in more detail. This equation also motivates the trend towards systems with high static magnetic field strengths B_0 that will be discussed in section 2.4.

Since the spatial resolution is inversely related to the signal-to-noise ratio, the chosen voxel sizes in X-nuclei MRI are relatively large. Generally there is a trade-off between small voxel sizes for a high geometrical accuracy and sufficient SNR with big voxel sizes and increased partial volume effects (see section 2.2.7). A better SNR often comes with an increase in measurement time, which at some point becomes unfeasible for the measured volunteers or patients.

2.2.7 Point Spread Function & Partial Volume Effects

The Point Spread Function (PSF) describes the response of an imaging system to a point source. In accordance with equation 2.33 the signal of a point source at location $\boldsymbol{r'}$ can be represented as

$$S(\boldsymbol{k}(t), t) \propto \int V \cdot \delta(\boldsymbol{r} - \boldsymbol{r'}) \cdot \mathrm{e}^{-2\pi i \boldsymbol{k}(t)\boldsymbol{r}} \mathrm{d}\boldsymbol{r} \propto \mathrm{e}^{-2\pi i \boldsymbol{k}(t)\boldsymbol{r'}} \tag{2.43}$$

with the use of the Dirac-Delta function. The PSF is the Fourier inverse of this expression and depends on the k-space sampling. In case of a dense enough sampling, the PSF can be seen as the FT of the sampled k-space volume.

The nominal image resolution is the ratio of the area under the PSF to the value of the PSF at the origin. Thus, the full width at half maximum (FWHM) of the PSF can be used as a measure of spatial resolution. The FWHM is broadened for the radial sampling scheme compared to a cartesian sampling scheme (Figure 2.4). This is the case as the FT of a cuboid volume is a sinc-function with a FWHM ≈ 1.21, while the Fourier transform of a sphere volume gives a full width at half maximum of FWHM ≈ 1.59. For the for ^{23}Na MRI utilized density-adapted 3D projection reconstruction (see section 3.2.1.2), the PSF was simulated to have a FWHM of 1.67 before being further widened by a Hamming filter to a FWHM of 2.1.

Partial volume effects decrease image quality by blurring small structures due to the limits in achievable resolution and are a combination of "tissue-fraction effects" and "spill-over effects".

Discrete sampling is one influence on the measured intensity distribution. The "tissue-fraction effect" is due to voxels having signal contributions from different tissue types. The measurement approximately depicts the weighted mean of the different tissue signals in the voxel. Partial volume effects can be reduced by reducing the voxel sizes, but even at high spatial resolution inaccuracies due to this effect can occur.

Truncation of the continuous, infinitely extended k-space signal at $k_{\max}$ can mathematically be described as the multiplication of the signal with a filter function $h(\boldsymbol{k})$. This is mathematically equivalent to a convolution of the signal in position space with the Fourier transform of the filter function. The resulting signal

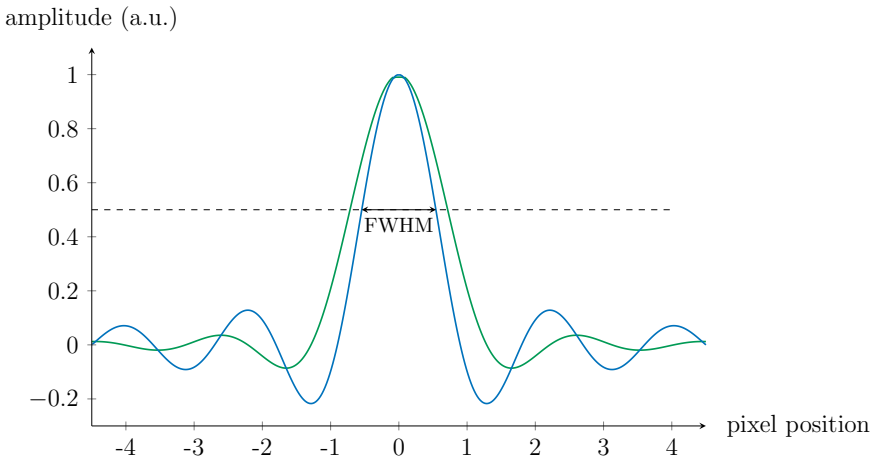

Figure 2.4: Comparison of the Point Spread Function in position space for a cartesian (blue) and a radial (green) readout scheme. The spherical sampling volume of the radial readout is broadening the full width at half maximum (FWHM) compared to the cuboid volume for cartesian readout.

intensity $S(\boldsymbol{x})$ in spatial domain is therefore

$$S(\boldsymbol{x}) = V(\boldsymbol{x}) \circledast H(\boldsymbol{x}) \qquad \text{with } H(\boldsymbol{x}) \coloneqq \mathrm{PSF}(\boldsymbol{x}) \tag{2.44}$$

where $V(\boldsymbol{x})$ is the true, immeasurable intensity distribution and $H(\boldsymbol{x})$ is the Fourier transform of $h(\boldsymbol{k})$. This leads to a broadened intensity distribution in the obtained image. The "spill-over effect" describes the overlap of signal intensity of adjacent tissue compartments, which can induce false signal intensities, especially in small structures of around the scale of the resolution or smaller. For example in the neighboring areas of a high signal intensity, some of that signal would "spill out", elevating the surrounding regions signal.

The in section 2.2.1 discussed lower signal strength of ^{23}Na MRI compared to ^{1}H MRI results in voxel sizes in X-nuclei MRI to be chosen relatively large. This and the fast T_2-relaxation broadens the PSF. The use of filters (see section 3.3.1.1), to smoothen the signal due to the low SNR, further widen the PSF. Combined, these factors reduce the accuracy of quantitative ^{23}Na MRI by partial volume effects.

2.2.8 Parallel Imaging

The NMR signal is detected by receiver coils, the properties of which have not yet been taken into account. Originally, the NMR phased array approach (Roemer et al., 1990), where multiple independent receive coils are used to simultaneously acquire data that is then combined in post-processing, was developed in order to increase the SNR without increasing the scan time. The different receive elements can also be used to decrease the imaging time with parallel imaging.

Each receive element has a spatially varying receive sensitivity $\mathcal{S}_i(\boldsymbol{r})$, resulting in equation 2.33 to yield

$$s_i(\boldsymbol{k}) = \int \mathcal{S}_i(\boldsymbol{r}) M_\perp(\boldsymbol{r}) \exp^{-2i\pi \boldsymbol{k}\boldsymbol{r}} \, \mathrm{d}\boldsymbol{r} \tag{2.45}$$

for the ith receive coil element.

In order to decrease the acquisition time, k-space is not sampled completely and missing information is estimated with the additional knowledge of the spatial information within the receive sensitivities. The employed phase undersampling dramatically reduces imaging time but leads to overlapping of the resulting signals. To separate overlapping images, the sensitivity maps provide the relative weighting of signals from different points of origin within each coil of the array.

This concept can be applied in image space or k-space with the most established methods being SENSitivity Encoding (SENSE) (Pruessmann et al., 1999) and GeneRalized Autocalibrating Partial Parallel Acquisition (GRAPPA) (Griswold et al., 2002). SENSE is performed in image space after reconstruction of data from the individual coils, while GRAPPA corrects in k-space before Fourier transformation.

In general, a larger number of coil elements increases the effectiveness of higher acceleration factors. The size of the raw data and the time for image reconstruction increases with the number of elements.

2.3 ^{23}Na MRI

This section will give a brief insight into sodium MRI and its challenges for MR imaging. For a more detailed description, the reader is referred to Madelin and Regatte (2013).

The main challenge of ^{23}Na MRI is the low SNR (see section 2.2.6) compared to ^{1}H MRI. Following equation 2.29, and considering the approximately 1000-times lower in vivo concentration of ^{23}Na compared to ^{1}H , the signal ratio becomes

$$\frac{S(^{23}\mathrm{Na})}{S(^{1}\mathrm{H})} \approx 10^{-4}. \tag{2.46}$$

For this reason, higher magnetic field strengths B_0 are chosen, as the signal strength depends on it at least quadratically (Ladd et al., 2018). When now factoring in the gyromagnetic ratio of ^{23}Na being approximately 3.8 times smaller than the ^{1}H gyromagnetic ratio (see Table 2.1), the Larmor frequency is reduced by the same factor according to equation 2.10. Assuming the thermal noise to be linearly dependent on the frequency (Nagel, Laun, et al., 2009), the SNR of both nuclei has a relation of

$$\frac{\mathrm{SNR}(^{23}\mathrm{Na})}{\mathrm{SNR}(^{1}\mathrm{H})} \approx 2.5 \cdot 10^{-3}. \tag{2.47}$$

As a result, ^{23}Na MRI suffers from long scan durations and/or reduced image resolution to achieve adequate SNR depending on the application.

Additionally, the bi-exponential transverse relaxation times are short for ^{23}Na as the quadrupole interactions (see section 2.1.6) lead to relaxation times in the order of milliseconds (Nagel, Laun, et al., 2009). To minimize the signal decay between excitation and data acquisition, pulse sequences with ultra short echo times (UTE) are required that pose high demands on the hardware (Serai et al., 2023). Center-out readout trajectories such as radial imaging, spiral imaging or twisted projection imaging combined with non-selective excitation are thus often used. As the imaging starts in the k-space center for center-out readout trajectories, no time is lost during the gradient that would otherwise be needed to move out of the k-space center before e.g. acquiring a line for a cartesian readout scheme.

The reduced gyromagnetic ratio of the ^{23}Na nuclei compared to the ^{1}H nuclei leads to a smaller Larmor frequency and thus larger wavelength for the same static magnetic field strength. ^{23}Na RF coils for 7 T can thus produce much more

homogeneous excitation fields, which is one of the major challenges of ^{1}H MRI at 7 T and is discussed further in section 2.4. Following equation 2.10, the smaller gyromagnetic ratio also makes ^{23}Na MRI less sensitive to off-resonances in the B_0 field as $\Delta\omega_0 = \gamma\Delta B_0$.

However, the smaller gyromagnetic ratio has the disadvantage to increase the gradient amplitude that is needed to reach a certain point in k-space. Due to the increased voxel sizes in ^{23}Na MRI leading to smaller maximal k-values for ^{23}Na MRI compared to ^{1}H MRI, this is mostly not problematic in practice.

2.4 Ultra High Field MRI

As the SNR is expected to increase at least linearly with the magnetic field strength B_0 (Ladd et al., 2018), higher field strengths are particularly interesting for applications where SNR is limited, such as X-Nuclei MRI.

The development towards higher field strengths takes place for clinical MR systems that now include 7 T additionally to the standard field strengths of 1.5 T and 3 T and experimental human MR systems that investigate MRI at 9.4 T, 10.5 T and 11.7 T. Field strengths above 7 T are considered ultra high fields (UHF).

While ^{23}Na MRI benefits from the increased SNR at ultra-high field strengths, proton MRI at UHF is becoming more challenging, particularly in the torso.

At higher fields, the imperfections of the static magnetic field are more pronounced. Additionally, susceptibility differences are proportional to B_0. This leads to differences between neighboring tissues causing macroscopic B_0 inhomogeneities (Truong et al., 2006). As a result, the spins accumulate different phases depending on their location, leading to a signal loss. Increased inhomogeneities in the static magnetic field can be addressed through higher order shimming coils.

The inhomogeneities and signal dropouts in the transmit field distribution are a result of interferences. According to equation 2.10, an increase in the static magnetic field strength leads to an increase in the Larmor frequency. The operational frequency of ^{1}H MRI at 7 T is 297.1 MHz, corresponding to a wavelength of about 11 cm, 13 cm and 42 cm in water, muscle and fat, respectively (Gabriel et al., 1996). As the dimensions of the human torso are larger than the wavelengths in water and muscle, interference effects influence the signal intensities. For most low flip

angle gradient echo sequences, constructive interference leads to hyperintensities in the image while destructive interference can cause complete signal dropouts. Since the first abdominal ^{1}H images at 7 T were published in 2009 (Vaughan et al., 2009), several methods were proposed to decrease signal dropouts. To improve the transmit field homogeneity and thus image quality, multi-channel transmit arrays, parallel transmit (pTx) (see section 2.4.1) and Time Interleaved Acquisition of MOdes (TIAMO) (see section 2.4.2) were used for ^{1}H MRI in the context of the here presented research work.

As the operational frequency of sodium is about 78.6 MHz at 7 T, which is comparable to ^{1}H MRI at 1.5 T, standing waves and interferences do not impact the image quality to a degree where pTx optimization would be required (Kraff et al., 2015; Platt, Ladd, et al., 2021).

2.4.1 Parallel Transmission

In parallel transmission (pTx), several transmission elements are used to generate a homogeneous B_1^+ field in a desired VOI. Each transmission element has a spatially varying transmit sensitivity $\mathcal{T}_i(\boldsymbol{r})$, which can be combined to generate an arbitrary RF waveform to excite the target magnetization

$$B_1^+(\boldsymbol{r},t) = \sum_{i=1}^{N} B_{1,i}^+(\boldsymbol{r},t) = \sum_{i=1}^{N} p_i(t)\mathcal{T}_i(\boldsymbol{r}) \tag{2.48}$$

with $p_i(t)$ being the RF pulse played through the ith transmit element. The amplitude and phase of the individual RF pulses can be altered, scaling or phase-shifting the resulting B_1^+ field. The new degrees of freedom that come from the increased number of transmission coils can be used to increase transmit field homogeneity or design subject-specific RF pulses for spatial selection. All pTx methods rely on some degree of prior knowledge of $\mathcal{T}_i(\boldsymbol{r})$ of the transmit channels, which is achieved by B_1^+ mapping.

Parallel transmit techniques are divided into static, dynamic and multi-pulse parallel transmit. In static pTx, the B_1^+ shim settings, which is a term used for the vector of the N phases and N amplitudes of an N-Tx-channel coil, is kept constant throughout the RF pulse to achieve a spatially uniform overall B_1^+ field by superpositioning the transmit sensitivities. In dynamic pTx, the shim settings vary during the RF pulse, allowing for temporal control over the applied RF field to produce a spatially uniform flip angle. For full pTx, this shim setting variation

requires an independent RF waveform generator and amplifier to independently drive each transmit channel with a microsecond temporal resolution. For this reason, dynamic pTx is more demanding for the RF hardware and safety supervision. The additional degrees of freedom can however help to generate the desired flip angle distribution at multiple spatial locations at once. Padormo et al. (2016) offer a good starting point to explore parallel transmit further than this thesis can offer.

The utilized 32-channel ^{1}H coil system (see section 3.1.3) has separate modulators and amplifiers for each coil allowing for static and dynamic pTx acquisitions. Typically there is a trade-off between achievable B_1^+ homogeneity and local SAR (see section 2.1.7) that can be administered.

2.4.2 Time Interleaved Acquisition of Modes

The mentioned transmit field inhomogeneity for ^{1}H MRI at high field strengths lead to spatially varying flip angles and thus an inhomogeneous image contrast. In case of destructive interferences, local signal dropouts may occur. One way of improving the homogeneity is Time Interleaved Acquisition of MOdes (TIAMO) developed by Orzada, Maderwald, et al. (2010), which works by acquiring two images with different excitation modes and reconstructing them together. The two modes are excited in an interleaved fashion applying static RF shimming with two static phase and amplitude sets as described in the previous section. Complementary RF patterns of the two modes produce images with differing distributions of signal hyperintensities and signal voids, which if combined lead to an improvement in signal homogeneity. This doubles acquisition time, which can be counteracted by encoding with accelerated GRAPPA (see section 2.2.8) and forming virtual receive elements out of the acquired data (2 times 32 receive elements) for a combined reconstruction with parallel imaging algorithms.

2.5 Physiological Fundamentals

Sodium ions play a vital role in many physiological processes in the human body. This section will give a short overview over the physiological principals that motivate ^{23}Na MRI with a focus on those relevant to the presented research. An in depth explanation can for example be found in Pape et al. (2023) and Speck-

mann et al. (2024) where the information in this section is taken from if not stated otherwise.

2.5.1 Sodium Ions in the Human Body

Na^+ is an important cation that plays a role in the homeostasis of the osmoregulation and the pH-regulation of the human organism. It is also involved in cell physiology, muscle contraction, heart activity and transmission of nerve stimuli (Heinrich et al., 2014).

In healthy cells the concentration of sodium ions in the intracellular space is about 5 mM to 15 mM, while it is about 140 mM to 150 mM in the extracellular space (Speckmann et al., 2024). The sodium–potassium pump, also known as Na^+/K^+-ATPase preserves this concentration gradient by utilizing the binding energy released during the hydrolysis of adenosine triphosphate (ATP) to adenosine diphosphate (ADP). This process is schematically depicted in Figure 2.5. For each conversion of ATP to ADP, three sodium ions are exported out of the cell and two potassium ions enter the cell (Speckmann et al., 2024). The Na^+/K^+-ATPase maintains a negative charge of the intracellular space compared to the extracellular space by not only working against the mentioned concentration gradient but also against the electrical resting potential. This process is important to reduce the intracellular osmolarity and thus prevent water influx. If the cell membrane integrity is disrupted or the energy metabolism is impaired, the concentration gradient is affected. The as a result forming Gibbs-Donnan equilibrium between the intra- and extracellular space results in osmotic swelling, which could lead to cell death. A schematic representation of the *Gibbs-Donnan effect* is shown in Figure 2.6. As the cell membrane is only letting small ions pass, the polyvalent macro-molecules (proteins) commonly found inside the cells can not pass through it. The concentration gradient between the intra- and extracellular space leads to chemical forces establishing an ion exchange until the concentration of ions in both compartments has the same value. The uneven distribution of the ions in the two compartments and the larger osmolarity in the intracellular space compared to the extracellular space results in osmotic pressure and an increased fluid level in the intracellular space. To counter this effect and prevent the associated osmotic swelling, the Na^+/K^+-ATPase is constantly transporting Na^+ out of the cell and K^+-ions into the cell. Furthermore, the diffusion of K^+ along its chemical gradient out of the cell creates a membrane potential which pushes Cl^- out of the cell. This contributes to the decrease in intracellular osmolarity to prevent water influx. This explains how the ^{23}Na concentration in the human body is regulating

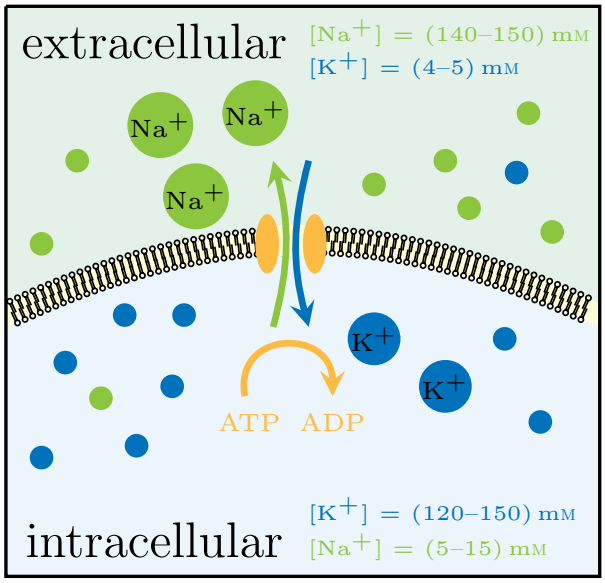

Figure 2.5: Schematic of the Na^+/K^+-ATPase. The energy from the conversion of ATP to ADP is used to export three sodium ions out of the cell and two potassium ions into the cell. In the extracellular space there are more sodium ions, whereas there are more potassium ions within the cell.

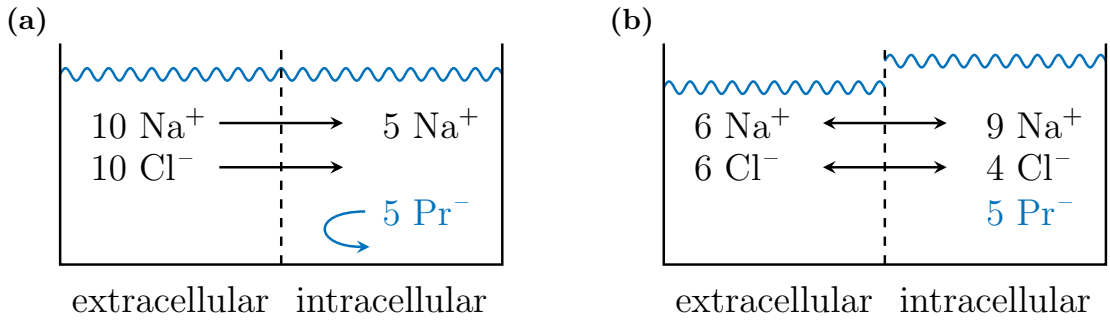

Figure 2.6: Schematic representation of the Gibbs-Donnan effect. Are two fluid compartments separated through a membrane (dashed line) that only lets small ions pass through and an impermeable protein (Pr^-) is present in one of the two compartments, an ion concentration imbalance is established between them. (a) shows the beginning after filling in the different fluids, while (b) shows the Gibbs-Donnan equilibrium with the resulting increased fluid level in the intracellular space due to osmotic pressure from the different particle concentrations. (Figure adapted from Pape et al. (2023)).

the extracellular volume.

To maintain the intracellular pH independently of the metabolic state of the cell, the naturally present sodium gradient between intra- and extracellular space is the prerequisite to transport H^+ ions from the cytoplasm into the extracellular space.

The measured sodium concentration consists of the weighted average of extra- and intracellular sodium content in the observed tissue. Hypoglycaemia, hypoxia, ischemia, or toxins are examples of what can lead to a degradation of the Na^+/K^+-ATPase due to an ATP deficiency (Konstandin et al., 2014). Pathological changes, which cause an expansion of the extracellular space or impair the Na^+/K^+-ATPase lead to an increase of the total sodium concentration in tissue (Maudsley et al., 1984). Determination of the tissue sodium concentration can thus be an indicator about the condition of the cells (Madelin and Regatte, 2013). ^{23}Na MRI as a non-invasive tool is particularly useful for such measurements, which is why several organs and other structures have been studied in vivo. Some of the possible applications are mentioned in the next section to give an overview over the versatility of potential uses.

2.5.2 Biomedical Applications of ^{23}Na MRI

This section will give a short insight into biomedical applications of ^{23}Na MRI, with a focus on the human torso. It is not exhaustive in the named resources nor applications and merely serves to provide insight into the extent of possibilities. For a more comprehensive overview Madelin and Regatte (2013) and Madelin, Lee, et al. (2014) can be consulted. As explained in more detail in section 2.5.1, the accurate determination of the ^{23}Na concentration in the human body is of diagnostic interest as the concentration of sodium ions indicates cell viability (Madelin, Lee, et al., 2014).

In the brain, ^{23}Na MRI studies investigated brain tumors (Ouwerkerk, Bleich, et al., 2003), strokes (Tsang et al., 2011) and neurodegenerative diseases such as Alzheimer's disease (Mellon et al., 2009), Huntington's disease (Reetz et al., 2012) and Multiple Sclerosis, during which the TSC increases inside demyelinated lesions (Huhn et al., 2019). In the case of a failed Na^+/K^+-ATPase, the ^{23}Na entering the cell can cause the concentration to be elevated by 300 % to 400 %, while the water concentration only rises by 12 % (Maudsley et al., 1984). The thus considerably

higher signal growth in ^{23}Na imaging compared to conventional ^{1}H MRI might help diagnosis.

In skeletal muscle, diseases such as diabetes, starvation, hypoxia and hypothyroidism can be linked to a decrease in Na^+/K^+-ATPase activity (Clausen, 2003).

There has been an interest in several different abdominal organs and structures. The repercussions of heart attacks due to an increased ^{23}Na content in nonviable myocardium were investigated with ^{23}Na MRI of the heart muscle (Sandstede et al., 2004; Bottomley, 2016). An increased myocardial sodium signal intensity was found in Conn's syndrome (Christa et al., 2019). Differentiation between benign and malignant breast lesions was performed with ^{23}Na MRI by Ouwerkerk, Jacobs, et al.; Zaric, Pinker, et al. and used to determine chemotherapy response (Zaric, Farr, et al., 2021). Sodium MRI was also investigated as a potential biomarker for prostate (Barrett et al., 2018) and lung cancer (Henzler et al., 2012). In the uterus, the treatment of uterine leiomyomata (uterine fibroids) alters the ^{23}Na levels, which means that ^{23}Na MRI can be used to investigate the molecular and metabolic pathways post treatment (Jacobs et al., 2009). The low ^{23}Na concentration in structures surrounding the joints leads to a high contrast in cartilage, that can be used to image osteoarthritis (Borthakur et al., 2006). Insko, Clayton, et al. (2002) show the feasibility of in vivo ^{23}Na MRI of the intervertebral disk (IVD) to evaluate proteoglycan content in the fibrocartilage. As the degeneration status of the IVDs is assumed to be linked to proteoglycans (Zbýň et al., 2016), for which there are currently no established clinical measurement routine, sodium MRI is a promising candidate for a biomarker to assess IVD degeneration.

The increase in extracellular sodium concentration from the renal cortex to the renal medulla is called cortico-medullary sodium gradient. It functions as fluid homeostasis regulation, as it is the main reason for water reabsorption from the filtrate back into the plasma (Maril, Rosen, et al., 2006). Pathological changes within the kidney can disturb this balance. Therefore the cortico-medullary sodium gradient has been subject of many studies, ranging from studies without dietary restrictions (Haneder, Juras, et al., 2014) to studies after water deprivation as well as after a water load (Maril, Rosen, et al., 2006; Akbari et al., 2022). Water deprivation was found to induce a significant increase in gradient strength of 25 % (Maril, Rosen, et al., 2006). The use of quantitative ^{23}Na MRI to assess renal function ranges from applications for nephropathy and renal failure to radiation therapy (Zöllner et al., 2016) and kidney transplantation (Madelin and Regatte, 2013). For further evaluation of an impaired transplanted kidney, a biopsy is often required which poses the risk of complications due to the invasive nature of this method.

A non-invasive imaging method such as ^{23}Na MRI could help to reduce the need for invasive methods (Moon, Furlan, et al., 2014) and is therefore an interesting tool to assess renal function.

3 Materials and Methods

This chapter gives an overview over the hardware components used in the experimental setup and the pulse sequences applied for MR imaging. The post-processing steps to generate quantitative ^{23}Na MR images are subsequently explained in detail.

3.1 Hardware

In this section the hardware utilized for phantom and in vivo MR measurements during the course of this research work is introduced.

3.1.1 MR Scanner

All measurements were conducted on a 7 Tesla whole-body research MR system (MAGNETOM 7T, Siemens Heathcare GmbH, Erlangen, Germany) at the German Cancer Research Center (DKFZ) in Heidelberg (Figure 3.1). The static magnetic field strength B_0 of this scanner is 6.98 T, directed in the (-z)-direction and the inner bore diameter of the tomograph is $d = 59.5$ cm. The integrated AS095-gradient system leaves enough room to integrate a custom-built pTx system with 32 coil elements, 32 transmit channels and 32 amplifiers for ^{1}H RF excitation (see section 3.1.3).

Additionally to the proton amplifiers, the MR scanner has a broadband amplifier (Dressler HF Technik GmbH, Stolberg, Germany) for a radio frequency range from 14 MHz to 130 MHz. This allows measurements of X-nuclei, such as ^{23}Na ($\nu_0(^{23}\text{Na})$ = 78.6 MHz) but also ^{13}C, ^{17}O, ^{31}P and ^{35}Cl, which will not be further discussed here. The scanner used in the context of the here presented research work has one transmit channel for X-nuclei and 32 receive channels, enabling a separate

Figure 3.1: 7 T whole-body MR system (MAGNETOM 7T, Siemens Healthineers AG, Erlangen, Germany).

processing of the RF receive signals originating from multi-channel coils, such as the ^{23}Na body coil described in section 3.1.2.

3.1.2 ^{23}Na Body RF Coil

Within this work, the aTSC in the human torso was measured using a custom-built torso ^{23}Na RF coil. This section will focus on the aspects of the coil that are relevant for the presented research but a much more in depth discussion can be found in Platt (2018). The oval-shaped birdcage coil with a large FOV of $(400\,\mathrm{mm})^3$, custom-built for torso examinations (Figure 3.3b) was used for phantom as well as for in vivo ^{23}Na MR measurements. The coil shape was tailored to have a high filling factor for the torso of adults (Platt, T. M. Fiedler, et al., 2016), while fitting into the MR tomograph with an inner bore diameter of $d = 59.5\,\mathrm{cm}$. Conventional birdcage coils consist of two round conductor loops, the so-called end rings, connected by four or a multiple of four of equidistantly spaced rods, creating a structure that resembles a birdcage. Birdcage coils have the advantage of a circularly polarized B_1-field perpendicular to the rotational axis of the coil. For spin excitation and signal reception, this field can be combined with the conventional MR tomograph with a static magnetic field B_0 along the bore.

For higher Larmor frequencies and larger birdcage coils, the wavelengths are in the range of the coil size, thus making birdcage coils less suitable. At higher field strengths, mostly small-sized birdcage coils, e.g. for the head, or other coil designs

are used for this reason. However, with a Larmor frequency of 78.6 MHz, this is not the case for ^{23}Na body coils at 7 T.

The coil used is fitted into two halves of an acrylic oval-shaped hollow cylinder. Due to the oval shape and the opening mechanism, the rods near the opening for splitting the coil had to be shifted and the coil is not rotationally symmetric as most other birdcage coils. In order to achieve homogeneous transmit (B_1^+) and receive (B_1^-) field distributions, the RF coil has four ports for feeding in and receiving RF signals. Close to the rods, strong field inhomogeneities are present. For in vivo measurements, the arms are positioned outside of the coil over the head.

3.1.3 ^{1}H Body RF Coil

For the ^{1}H MR measurements, a custom-built 32-channel pTx add-on system (Orzada, Solbach, et al., 2019) was used for transmission as well as reception. The in Figure 3.2 shown coil system is currently the only ^{1}H body coil behind the bore worldwide. The first version was installed in Essen (Orzada, Solbach, et al., 2019) but was later removed. The second version of this body coil system is integrated into our research scanner. Importantly, the use of the single-channel operation mode of the original MRI system is not affected by the add-on system (Orzada, Solbach, et al., 2019).

The 32 antenna elements are placed in three rings between the bore liner and the gradient coil. This configuration allows the simultaneous use of the local ^{23}Na RF coil (shown in Figure 3.3b) and the remote ^{1}H RF coil. Previously, the combination of the 32-channel pTx system for ^{1}H MRI and the ^{23}Na RF coil for sodium MRI was not possible, which is why certain parts of this thesis will not employ the ^{1}H RF coil but focus solely on ^{23}Na MRI.

3.1.4 Phantom

To validate the measurement and correction routines before conducting volunteer measurements, a 10 L canister (hünersdorff GmbH, Ludwigsburg, Germany) filled with 35 mM of NaCl (Sigma-Aldrich, St. Louis, United States of America) and demineralized water was used as a homogeneous phantom. It is approximately

Figure 3.2: Picture of the custom-built 32-channel ^{1}H RF coil resting on the bore liner. Here, the setup is shown outside of the scanner bore.

(a) **(b)**

Figure 3.3: (a) shows a picture of the canister used as phantom for validation measurements and (b) depicts the positioning of the canister on top of the reference vial setup (see section 3.1.5) in the ^{23}Na RF body coil used (see section 3.1.2).

30.6 cm long, 16 cm wide and 27 cm high with rounded edges and corners (see Figure 3.3).

3.1.5 Reference Vial Setup

For the concentration determination, a fixed reference vial setup was developed as part of this work. Requirements for the setup were determined to include the following:

- respiratory motion should not influence vial placement
- vials should be large enough to reduce the influence of PVE (see section 2.2.7) on the determined signal intensity

- the setup should take up as little space as possible within the ^{23}Na RF coil (see section 3.1.2) to restrict volunteers as little as possible
- placement of the vials within the ^{23}Na RF coil should be in a region of small B_1 inhomogeneities
- susceptibility artifacts should be considered
- automatic segmentation of the reference vials in order to speed up post-processing
- exchange of the used reference vials for quantification in case a different range of concentrations was needed

In order to meet these criteria, the positioning of the vials within the coil was tested in experiments. From these experiments, the placement of each vial was chosen to be between two rods of the ^{23}Na RF coil to minimize the influence of transmit and receive field inhomogeneities, despite their placement in the peripheral part of the RF coil's FOV. A design of an interchangeable compartment, which works like a drawer along with the drawer housing that serves as the volunteer's laying surface was developed. The setup was placed in a fixed position below the subject to minimize the impact of respiratory motion on the vial placement and thus the results in the vials. For this, the drawer housing and lower part of the compartment were shaped to fit the rounding of the ^{23}Na RF coil. Both were built in-house and are manufactured out of acrylic glass and displayed in Figure 3.3b underneath the phantom (see section 3.1.4) and Figure 3.5a within the lower part of the ^{23}Na RF coil.

The reference vials used within the compartment were chosen to be fairly large to reduce the influence of partial volume effects on the parts used for concentration determination that could otherwise lead to an overestimation of the signal intensities after correction. To minimize the height of the setup, oval-shaped reference vials (Rixius AG, Mannheim, Germany) were used, keeping the overall structure of the vial setup at a maximal height of 52 mm within the coil. The bottles contain a nominal volume of 250 mL with a length of 59.8 mm, a width of 38 mm and a height of 169 mm.

Within the interchangeable compartment, four symmetrically arranged oval-shaped reference vials filled with demineralized water and known concentrations of sodium (Sigma-Aldrich, St. Louis, United States of America) are embedded in a mixture of 35 mM NaCl, 2 % agarose (Art.-Nr. 2267.4, Carl Roth GmbH + Co. KG, Karlsruhe, Germany) and demineralized water to reduce susceptibility artifacts and to improve B_0 shimming capabilities (Gerhalter, Gast, Marty, Uder, et al., 2020). For phantom measurements, vials containing 20 mM, 30 mM, 40 mM and 50 mM

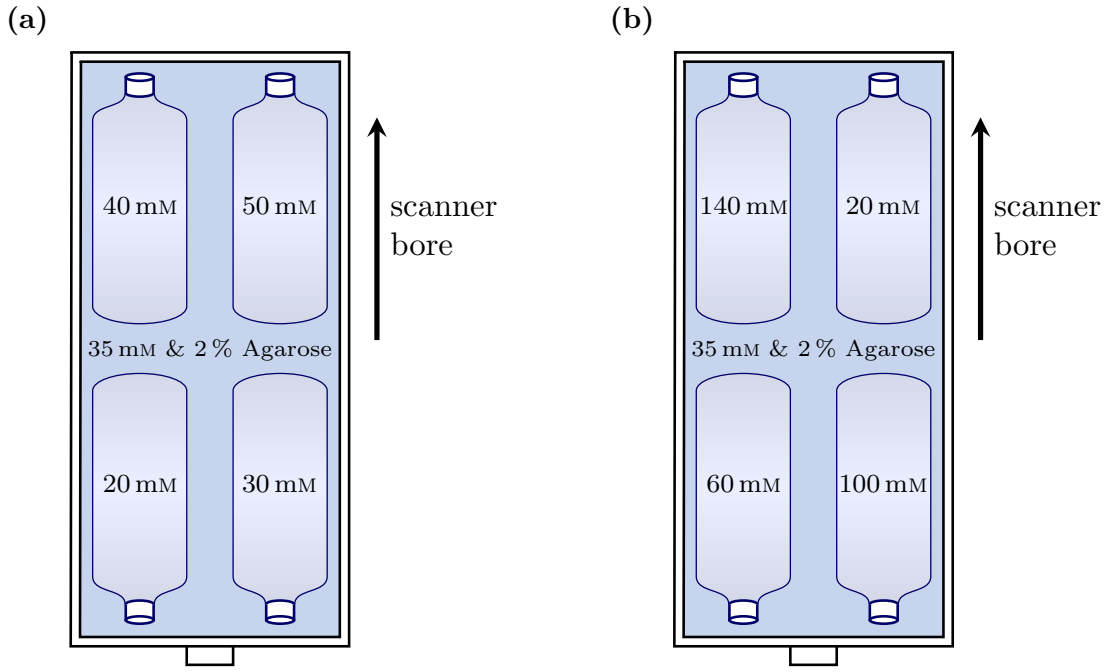

Figure 3.4: Schematic of the reference vial setup showing the reference vial placement for (a) phantom and (b) in vivo measurements.

NaCl (Sigma-Aldrich, St. Louis, United States of America) and demineralized water were used. For in vivo measurements, vials with sodium concentrations of 20 mM, 60 mM, 100 mM and 140 mM were used to span the expected range of naturally occurring ^{23}Na within the torso. Figure 3.4 displays the arrangement of the vials within the setup for the phantom (Figure 3.4a) and in vivo measurements (Figure 3.4b). In order to guarantee reproducible vial placement within the compartment, the in Figure 3.5b shown separator was build that fits the drawer compartment. The four cut-outs can be used to place the reference vials into the compartment before removing the separator and filling the compartment with agarose gel.

Since the reference vials are always positioned at the same location within the coil, the same masks in the reference vials can be used in every examination for the concentration determination and do not have to be segmented every time. Vial placement for each in vivo measurement was checked with ^{1}H MRI data and shifted in case the volunteers had slightly moved the setup while lying down. This adjustment was never more than 2 voxels.

Figure 3.5: Picture of (a) the reference vial setup within the lower part of the ^{23}Na RF coil (see section 3.1.2), showing the reference vial placement and of (b) the separator used for reproducible reference vial placement.

3.1.6 Drinking Bag

To drink inside the scanner during the water load experiment described in section 4.3.1, the drinking bag (Bbaiyule, ASIN: B09Z6NJ645) shown in Figure 3.6 filled with approximately 1 L of water (Na^+: 20 mg L^{-1}) was positioned inside the bore. It allowed the volunteer to drink without changing their position during the measurement.

3.2 Pulse Sequences

A pulse sequence is the combination of RF excitations, gradients and signal acquisitions. This section is explaining the pulse sequences used for ^{1}H and ^{23}Na MRI in the context of the presented research and their characteristics.

In non-selective 3D techniques all spins of the sample volume located in the sensitive part of the coil are excited at once and contribute to the acquired signal. In contrast, with selective 3D techniques as well as with 2D techniques only spins of a specific slice or slab are excited and contribute to the signal (see section 2.2.2).

Figure 3.6: Drinking bag used to drink inside the scanner without changing positions. It was used for the experiment described in section 4.3.1 where change in the kidney before during and after a water load were investigated.

3.2.1 ^{23}Na MR Imaging

3.2.1.1 Calibration of the Reference Voltage

Before each ^{23}Na MR measurement, the relationship between the applied voltage and the resulting flip angle has to be established. While the assessment of the reference voltage U_{ref} is integrated into the measurement routine for ^{1}H MRI, it has to be performed manually for ^{23}Na MRI for each combination of RF antenna and load. The load affects the B_1 field strength of the coil and thus, in combination with the pulse duration τ and the gyromagnetic ratio γ, the flip angle α (see equation 2.19). Due to the connection of the reference voltage and the flip angle, the reference voltage calibration is also called flip angle calibration.

U_{ref} is defined as the voltage of a rectangular excitation pulse of length $\tau = 1\,\text{ms}$ needed to invert the equilibrium magnetization ($\alpha = 180°$). This reference voltage is then used to determine the correct pulse voltage U_{pulse} for each pulse of the pulse sequence depending on the associated pulse shape and duration for a specific nominal flip angle α. In case of a rectangular pulse, U_{pulse} is proportional to α and inversely proportional to τ.

To perform the calibration, the examined volume is globally excited and the signal is read out with a gradually increasing pulse voltage. The reference voltage can then be obtained from the pulse duration and the period of a sinus fit to the

resulting signal. The first maximum of the signal at $U_{\max}$ is equal to the signal of an RF pulse with a nominal flip angle of $\alpha = 90°$. For a pulse duration of $\tau = 2\,\text{ms}$, $U_{\max} = {}^{U_{\text{ref}}}/_{4}$.

For the presented research work the calibration was carried out with the following parameters: $T_{\text{E}}\,/T_{\text{R}} = 1.1\,\text{ms}/400\,\text{ms}$, $\tau = 2\,\text{ms}$, $U_{\text{pulse}} = 0\,\text{V}$ to $400\,\text{V}$, measurement points = 32, averages = 1. This resulted in reference voltages in the phantom of $(1262.9 \pm 4.3)\,\text{V}$ and in vivo of $(1353.7 \pm 28.9)\,\text{V}$.

3.2.1.2 Density-Adapted 3D Projection Reconstruction Sequence

MR imaging of nuclei with a spin ≥ 1 is especially challenging due to the short relaxation times caused by the electrical quadrupole moment of the nuclei (see section 2.1.6). For this reason sequences with a short echo time T_{E} are needed to assess as much as possible of the fast decaying signal e.g. to enable spin density weighted MRI and a quantification of the aTSC. This can be achieved with projection imaging, where data acquisition always starts in the center of k-space as for example with the density-adapted 3D projection reconstruction sequence (DA-3DPR). For the DA-3DPR sequence, data acquisition can start immediately after the rectangular excitation pulse and the dead time of about 50 µs, which is the time the scanner needs to switch between transmit and receive case (Nagel, 2009).

All ^{23}Na acquisitions, except the reference voltage calibration, were performed using the DA-3DPR, developed by Nagel, Laun, et al. (2009) and depicted in Figure 3.7. In the beginning, the magnetization is excited with a non-selective RF pulse with the pulse duration τ. The readout gradient is applied after the echo time T_{E} and is divided into three different sections. First it is linearly increasing, followed by a plateau area and then it is decreasing, following a trajectory that ensures a more uniform k-space coverage than standard radial readouts. After the repetition time T_{R}, the depicted scheme is repeated (not shown in the figure) and the next projection along a new k-space line is acquired center-out.

As with conventional 3D radial sequences, the radial projections are spaced homogeneously in k-space for the standard acquisition scheme, which can be achieved with an algorithm by Rakhmanov et al. (1994). For this algorithm, the endpoints of the recorded projections lie helical on the surface of the k-space volume.

Conventional 3D radial sequences maintain a constant readout gradient ampli-

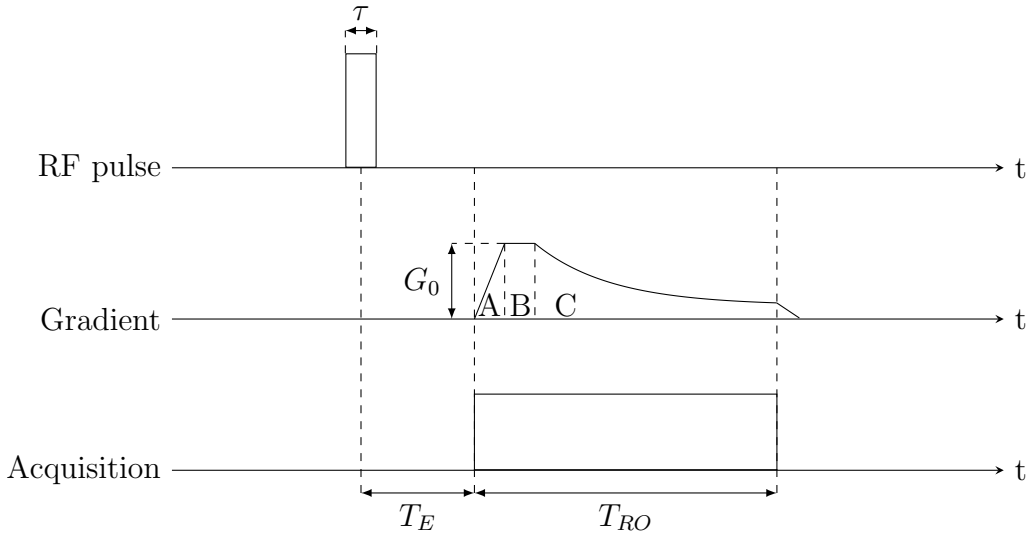

Figure 3.7: Sampling scheme of the DA-3DPR sequence. The readout gradient can be divided into three parts: A: a linear part, B: trapezoidal part and C: the density-adapted section (Figure adapted from Nagel, Laun, et al. (2009)).

tude, causing non-uniform k-space coverage (Konstandin et al., 2014) as each of the measurement points has an equal distance to the next acquired point on the current projection (Figure 3.8a). This leads to an oversampled k-space center while outer k-space is sampled more sparsely, resulting in a loss of SNR (Nagel, Laun, et al., 2009). To achieve a more uniform k-space coverage and thus increased SNR, density-adapted gradient (Nagel, Laun, et al., 2009) can be used, where the outer parts of the projections are sampled with decreasing distance between measurement points to keep the number of scanned points per volume constant, while an inner sphere of k-space is sampled without density adaption due to hardware restrictions (Figure 3.8b).

DA-3DPR shows a gain of 34 % in SNR compared to conventional radial acquisition (Konstandin et al., 2014) and lower dependence on B_0 inhomogeneity than conventional 3D radial sequences (Nagel, Laun, et al., 2009), which is beneficial for ^{23}Na MRI which suffers from lower in vivo SNR compared to ^{1}H MRI. The lower dependence on B_0 inhomogeneity is specifically beneficial as the scanner does not support B_0 shimming for single-resonant ^{23}Na RF coils to adjust B_0 for the imaged object.

The DA-3DPR sequence can achieve ultrashort T_{E} (UTE) times which limits the influence of T_2^* on the quantification. To reduce the influence of the T_1 decay, a

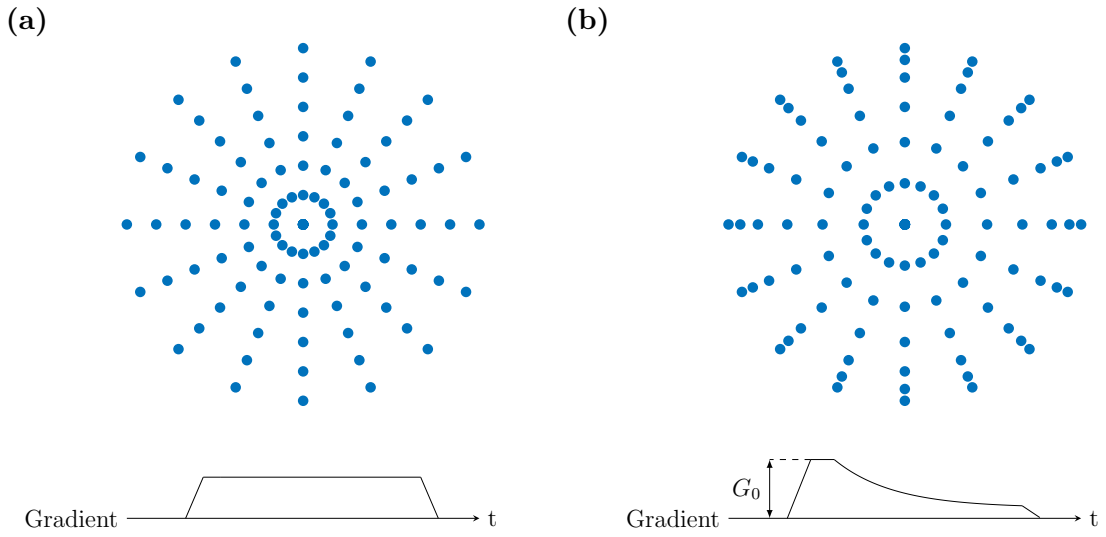

Figure 3.8: Radial readout sampling scheme with the conventional trapezoidal readout gradient (a) and density adapted readout with corresponding gradient (b). The decreasing sampling density in the peripheral part of k-space for the conventional radial readout can be counteracted by reducing the amplitude of the gradient during readout and thus acquiring points in k-space with a smaller distance between them for a fixed dwelltime. The 2D case is illustrated for clarity but the same principle can be applied in 3D.

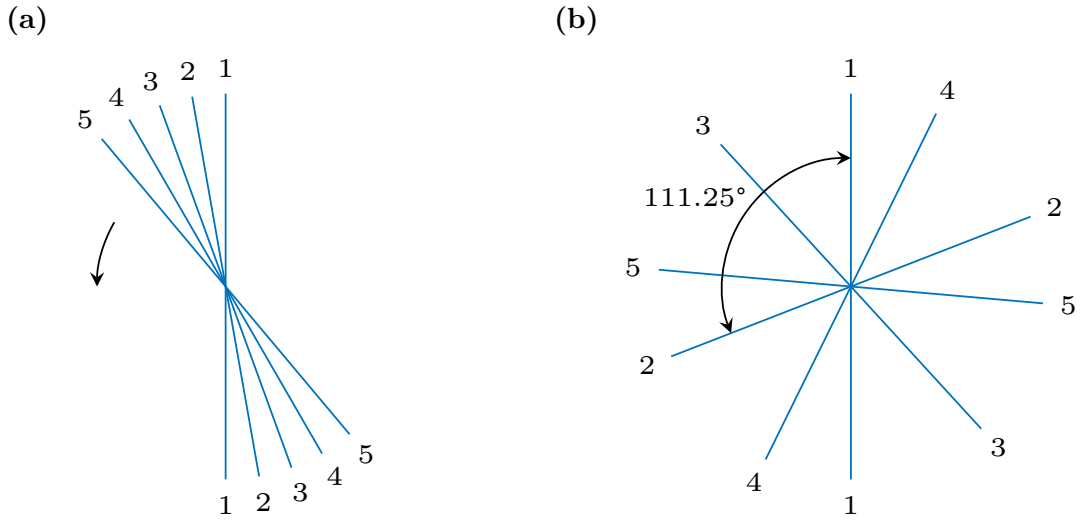

Figure 3.9: Radial readout trajectories linearly incrementing spokes (a) and distributing the spokes based on golden angles (b). In the shown 2D case, the golden angle between two spokes is 111.25°.

long repetition time (T_R) was chosen.

Additionally, two points in k-space center were acquired before the gradient starts which could in the future be used for retrospective respiratory sorting of the ^{23}Na data (Platt, Umathum, et al., 2018).

3.2.1.3 Golden Angle Imaging

Non-Cartesian k-space trajectories such as radial or spiral are showing a smaller dependency on respiratory motion compared to cartesian readout schemes (Lauzon et al., 1996) but still suffer from blurring artifacts. Instead of sampling linearly by incrementing each spoke by a certain angle to cover all of k-space, the 3D-Golden-Angle (GA) distribution by Chan et al. (2009) distributes the projections pseudo-randomized (Figure 3.9). The calculation is based on the 2D golden means from a method by Winkelmann et al. (2007), leading to a more uniform coverage of k-space through time.

Utilizing GA sequences gives the possibility of retrospective sorting into different subsets while still ensuring a fairly homogeneous distribution of projection for any

time interval. This was utilized in section 4.3.1, where data was divided into subsets in a sliding window fashion to assess the aTSC in the kidneys during a water load, while remaining inside the scanner.

The golden angle projection scheme was used for all ^{23}Na acquisitions, except the reference voltage calibration.

3.2.1.4 B_1^+ Mapping

As the signal is proportional to the flip angle α, it is important to know the spatial deviations from the target flip angle to compensate for the variations and enable an accurate quantitative measurement. From equation 2.19 it can be deducted, that the flip angle distribution results from the transmit field distribution B_1^+ . To obtain the B_1^+ map for correction of the quantitative ^{23}Na MR images, the double angle method by Insko and Bolinger (1993) is used.

The same spin-density weighted pulse sequence is recorded twice with only the nominal flip angle changing between the two acquisitions (α_1 and $\alpha_2 = 2\alpha_1$). Since the method assumes complete relaxation, repetition times T_R have to be chosen long compared to the longitudinal relaxation time T_1. As the separation of T_{1l} and T_{1s} is challenging due to the noise level of ^{23}Na MRI and exchange between sodium pools is fast relative to T_1, a mono-exponential relaxation model for the longitudinal magnetization is commonly assumed in literature (e.g. Kratzer et al., 2021; Madelin, Jerschow, et al., 2012). With this assumption, equation 2.24 for $t = T_\mathrm{R}$ yields:

$$M_\parallel(T_\mathrm{R}) = M_0 \cdot \left(\cos(\alpha) \cdot \mathrm{e}^{-\frac{T_\mathrm{R}}{T_1}} + 1 - \mathrm{e}^{-\frac{T_\mathrm{R}}{T_1}}\right) \tag{3.1}$$

Therefore, 95 % of the longitudinal magnetization are relaxed after $T_\mathrm{R} = 3 \cdot T_1$ and 99 % after $T_\mathrm{R} = 5 \cdot T_1$ for a 90° excitation pulse. With T_R shorter than 4-5 times the T_1 of the imaged tissue, saturation effects can lead to intensity variations reflecting T_1 effects rather than transmit/receive effects, which can negatively impact the correction (Wang et al., 2005).

From the proportionality of the recorded signal intensities (I_1 and I_2) to the flip angle, Insko and Bolinger (1993) calculate the flip angle map from the ratio:

$$r_{1,2}(\mathbf{r}) = \frac{I_1(\mathbf{r})}{I_2(\mathbf{r})} = \frac{\sin(\alpha_1)}{\sin(2 \cdot \alpha_1)} = \frac{\sin(\alpha_1)}{2 \cdot \sin(\alpha_1)\cos(\alpha_1)} = \frac{1}{2 \cdot \cos(\alpha_1)} \tag{3.2}$$

to be

$$\alpha_{\text{map}}(\mathbf{r}) = \arccos\left(\frac{1}{2 \cdot r_{1,2}(\mathbf{r})}\right). \tag{3.3}$$

For a rectangular RF pulse of duration τ, equation 2.19 leads to

$$B^{+}_{1,\,\text{map}}(\mathbf{r}) = \frac{1}{\gamma\tau} \cdot \arccos\left(\frac{1}{2 \cdot r_{1,2}(\mathbf{r})}\right). \tag{3.4}$$

The division of two images in equation 3.2 to calculate the B_1^+ map with the double angle method can lead to extreme values within the flip angle map, especially in regions with low signal intensity, where noise amplification and division by near-zero values may introduce artifacts and inaccuracies. When evaluating the sodium concentration in a phantom or in vivo, these areas should not be considered, as they do not reflect the real RF field distribution. For the phantom used during this study, these outlier values were not within the investigated region of interest. For in vivo measurements, this was only relevant in z-direction, where the outermost voxels are less reliable.

A pulse sequence with alternating excitation (Felz et al., 2023) was employed for later measurements instead of the above described approach of acquiring two images with a different flip angle one after the other. Here α_1 and α_2 were applied in an interleaved manner for excitation. Additionally, two readouts with different echo times were performed after each excitation to allow simultaneous acquisition of B_0 maps without prolonging the measurement time. The resolution of the ^{23}Na B_1^+ maps was in this case chosen to be $(\Delta x)^3 = (20\,\text{mm})^3$ to reduce measurement time, which is sufficient as B_1 maps usually do not change fast on small spatial scales (Platt, Umathum, et al., 2018). As shorter T_R times were utilized to further decrease the scan time, they were chosen such that the respective steady state magnetization following equation 3.1 was similar after each excitation for a fixed T_1.

3.2.2 ^{1}H MR Imaging

As described in section 2.4, achieving a homogeneous excitation fields is complicated by the dielectric currents in tissue producing wavelength effects, which are particularly prominent at high frequencies (Collins et al., 2011). For this reason, static pTx (see section 2.4.1) was utilized for the acquisition of ^{1}H images in the context of this reasearch work.

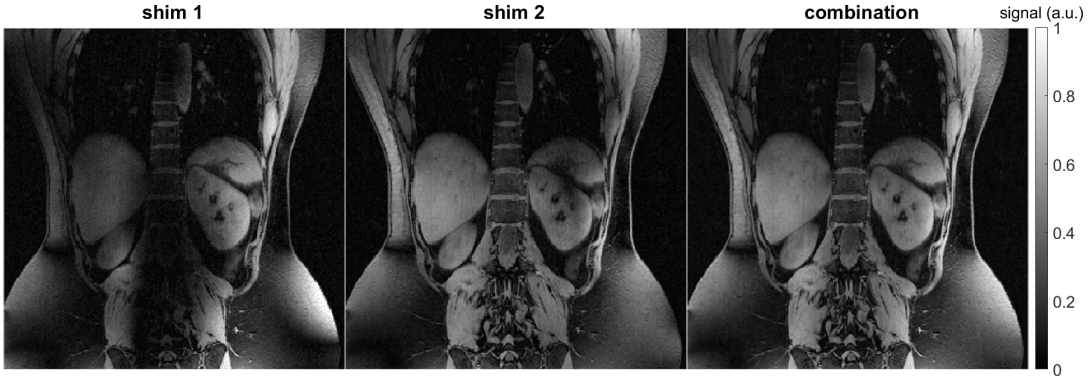

Figure 3.10: Coronal view of the same slice for the two acquired TIAMO shim modes and the combined ^{1}H MR image. The signal dropouts in different regions for the two shims reduces the signal dropout severity in the combined image as can for example be observed in the left kidney for the here shown slice.

Since the acquisition time of ^{23}Na images for quantification was long to facilitate accurate determination of the aTSC, B_1^+ shimming for ^{1}H MRI was refrained from. Instead, a TIAMO shim (see section 2.4.2) by applying two modes optimized for a torso-simulating polyvinylpyrrolidone phantom mimicking the dielectric tissue parameters of the human body (Platt, Umathum, et al., 2018) was used with the assumption of the resulting ^{1}H images to be sufficient for image segmentation of central abdominal structures (see section 3.3.6).

Figure Figure 3.10 shows an example of how these two shim modes can look like in a volunteer. The two modes show signal dropouts in different regions, which reduces the severity of signal dropouts in the combined image. This can be seen particularly well in the left kidney for the shown slice.

For measurements where ^{1}H MRI was performed, a localizer utilizing the described TIAMO shim was used for position control and to determine the B_0 shimming volume. Then, initial B_0 shimming of the whole phantom and vial setup for phantom measurements, and of the whole body for in vivo measurements was performed.

A 3D ^{1}H GRE sequence with radial phase-encoded (RPE) acquisition (GRE-RPE) (Buerger et al., 2012) that has been adapted to 7 T (Dietrich et al., 2021) in combination with the in section 3.1.3 described pTx body coil was applied utilizing the same TIAMO shim to acquire high-resolution in vivo ^{1}H images for the segmentation of different abdominal structures.

The SAR (see section 2.1.7) was limited by limiting the input power per channel. Therefore, a custom safety supervision system as described by T. Fiedler et al. (2024) was used, which automatically shuts off if any channel exceeds the 10 s or 6 min power limit for the torso, which was predefined according to electromagnetic (EM) simulations.

3.3 Image Reconstruction & Post-Processing

Quantitative ^{23}Na MR imaging is influenced by respiratory motion, partial volume effects (see section 2.2.7) as well as inhomogeneities of the static magnetic field, the transmit and the receive field distribution. To obtain reliable ^{23}Na concentration values, theses influences have to be considered or corrected for. In this section the steps applied in the reconstruction and post-processing of the MR images are described. If applicable, the ^{23}Na data was first divided into subsets (see section 3.3.1), followed by the reconstruction of the images utilizing filters depending on the image type (see section 3.3.1.1) and zerofilling (see section 3.3.1.2). After the combination of the different channels (see section 3.3.1.3), the resulting images were then corrected for T_1 effects (see section 3.3.3), B_1^+ (see section 3.3.4.1) and B_1^- (see section 3.3.4.2). The apparent sodium concentration was then determined in measurement-specific volumes of interest (VOIs) as described in section 3.3.8. If ^{1}H images were acquired, they were reconstructed (see section 3.3.2) separately for the two acquired modes (see section 3.3.1.3) due to memory constraints and then SOS combined. After they were used for segmentation as described in section 3.3.6, they and the resulting masks were interpolated to have the same resolution as the ^{23}Na MR images (see section 3.3.7).

3.3.1 Image Reconstruction of ^{23}Na MR Data

To transform ^{23}Na MR data from momentum into position space, a non-uniform fast fourier transform (NUFFT) introduced by Fessler et al. (2003) was used. To counteract the non-homogeneous sampling density of the data, a density compensation was performed. Datasets for ^{23}Na B_1^+ maps were Gauss-filtered (σ = 20 mm), ^{23}Na image data was filtered with a Hamming filter (see section 3.3.1.1).

To evaluate the influence of a water load on the renal aTSC (see section 4.3.1), ^{23}Na MR data was retrospectively sorted into subsets in a sliding window approach using

Matlab (The MathWorks Inc., Natick, MA, USA, Version R2024b). Due to the 3D golden angle imaging approach (see section 3.2.1.3), the created data subsets are approximately uniformly sampled in k-space (Chan et al., 2009; Feng et al., 2016; Resetar et al., 2015). Full datasets and subdivided datasets were reconstructed separately.

3.3.1.1 Filter

Filters are often employed to smooth the MR signal, increase the SNR and reduce artifacts (R. Stobbe et al., 2008). As described in section 2.2.7, this comes at the expense of broadening the PSF. In the presented research work, datasets for ^{23}Na B_1^+ maps were Gauss-filtered ($\sigma = 20\,\text{mm}$), while ^{23}Na image data was filtered with a Hamming filter. Both are window functions that are multiplied with the raw data in k-space. The Gauss-filter is calculated as

$$F_{\text{Gauss}} = \exp\left(-\frac{k^2}{2\sigma}\right) \tag{3.5}$$

where the variance σ can be chosen to adjust the filter width. The Hamming-filter is given by

$$F_{\text{Hamming}} = \frac{25}{46} + \frac{21}{46} \cdot \cos\left(\frac{2\pi k}{W}\right) \tag{3.6}$$

where k is the distance from the k-space center and $W = 2k_{\text{max}}$ defines the window width. Another common filter is the Hanning filter which is given as

$$F_{\text{Hanning}} = \frac{1}{2}\left(1 - \cos\left(\frac{2\pi k}{W}\right)\right). \tag{3.7}$$

3.3.1.2 Zerofilling

The image resolution Δx of the acquired image and the matrix size M used in the reconstruction influence the reconstructed FOV (e.g. $FOV_{\text{reco}} = \Delta x \cdot M = 5\,\text{mm} \cdot 80 = 400\,\text{mm}$). *Zerofilling* can be used to scale up the matrix size by filling the peripheral k-space areas with zeros, resulting in an image resolution that is higher than the acquired nominal resolution (e.g. $FoV'_{\text{reco}} = \Delta x' \cdot M = 2.5\,\text{mm} \cdot 160 = 400\,\text{mm}$). The resulting image is however smoother than an image that was acquired with a nominal resolution equivalent to the image resolution of the zerofilled

image. Zerofilling thus enhances the apparent spatial resolution by mitigating partial volume effects (see section 2.2.7) without requiring additional data. For this reason, zerofilling was employed for the ^{23}Na data. ^{23}Na image data was zerofilled with a zerofilling factor of two as this yields a gain in information due to the Fourier transform capturing all "true" data from the FID signal (Bartholdi et al., 1973). Higher zerofilling factors offer no further benefit as the Fourier coefficients are completely correlated. For the datasets for ^{23}Na B_1^+ maps, higher zerofilling factors were employed to generate the same Matrix size after reconstruction as for the image data.

3.3.1.3 Combination of Multi-channel Coil Data

When a multi-channel receive coil is used for MR imaging, the separately recorded data points from each channel can be combined to one data set.

For the ^{23}Na RF coil data, the combination was done with the sum-of-squares (SOS) method. The intensity of the combined image I_{total} is computed as the square of the voxelwise summation over the quadratic intensities of the N separate channels I_i:

$$I_{\text{total}} = \frac{1}{N} \cdot \sqrt{\sum_{i=1}^{N} I_i^2}. \tag{3.8}$$

As the sensitivity maps of the individual coils are not needed to combine multiple channels, this approach is one of the easiest and most widely used methods. The phase information is lost in this approach, generating a pure magnitude image.

3.3.2 Image Reconstruction of ^{1}H MR Data

For the ^{1}H data, SENSE (Pruessmann et al., 1999) was utilized, which is one of the most widely used parallel imaging methods (see section 2.2.8) and is performed in image space after reconstruction of data from the individual coils. To reduce the measurement time, some lines of k-space are skipped during image acquisition, resulting in a smaller FOV for each coil and thus aliasing as parts of the image are folded over each other. Contrary to the coil combination employed for ^{23}Na images, coil sensitivity maps are an important part in the SENSE method as each aliased image from a single coil is a superposition with different weights according

to the local coil sensitivity. The sensitivity maps can thus be used to combine the aliased images from each coil in a matrix inversion.

For a cartesian sampling of k-space, the matrix to perform the signal separation is calculated as

$$U = (S^H \mathbf{\Psi^{-1}} S)^{-1} S^H \mathbf{\Psi^{-1}} \tag{3.9}$$

where S is the sensitivity matrix, the superscript H denotes the transposed complex conjugate and $\mathbf{\Psi}$ is the receiver noise matrix, describing the levels and correlation of noise in the receiver channels. As long as the inversion of equation 3.9 is possible, the unfolding can be performed. This means the number of coils must be larger than the number of voxels that need to be separated. Pruessmann et al. (1999) can be consulted for a more in depth mathematical explanation.

The two acquired TIAMO modes (see section 2.4.2) were reconstructed separately due to memory constraints and then SOS combined according to equation 3.8.

3.3.3 Correction of T_1 Relaxation Effects

The equilibrium signal of a Fast Low Angle Shot (FLASH) sequence, such as the 3D-DAPR sequence (see section 3.2.1.2), is given by

$$S \propto M_0 \cdot \sin(\alpha) \cdot \frac{1 - \mathrm{e}^{-T_R/T_1}}{1 - \mathrm{e}^{-T_R/T_1} \cos(\alpha)} \cdot \mathrm{e}^{-T_E/T_2^*} \tag{3.10}$$

with the longitudinal equilibrium magnetization M_0, the flip angle α, the relaxation times T_1 and T_2^* of the measured object and the sequence parameters T_E (echo time) and T_R (repetition time).

The ^{23}Na T_1 time in the reference vials and phantom is longer than in tissue and does not allow for a full relaxation of the longitudinal part of the magnetization with the utilized sequence parameters. For $T_{1,\mathrm{NaCl}} = 55\,\mathrm{ms}$ (Nagel, Lehmann-Horn, et al., 2014), $5 \cdot T_{1,\mathrm{NaCl}} = 275\,\mathrm{ms} > T_\mathrm{R} = 150\,\mathrm{ms}$. Therefore T_1 relaxation effects were corrected in the reference vials and the phantom with a correction factor of 0.965 for a nominal flip angle of 61°. Since $T_\mathrm{R} = 150\,\mathrm{ms} \approx 5 \cdot T_{1,\mathrm{kidney}} = 5 \cdot 34\,\mathrm{ms}$ with $T_{1,\mathrm{kidney}}$ taken from Maril, Margalit, et al. (2004), full relaxation was assumed in human tissues. The correction factor resulting from the flash equation would be 0.994 for this T_1 time.

As the longitudinal equilibrium magnetization in the not fully relaxed regions is

smaller than M_0, the signal in the reference vials is underestimated and the resulting concentration in the in vivo data is overestimated without a T_1 correction. After the T_1 correction, the quantitative ^{23}Na image is still influenced by inhomogeneities in transmit (B_1^+) and receive (B_1^-) fields of the utilized coil (Gast et al., 2023), for which the corrections are described below.

3.3.4 Corrections of Transmit and Receive Field Influences (B_1)

3.3.4.1 B_1^+ Mapping and Correction

To generate a constant flip angle throughout the investigated region, most excitation pulses require a homogeneous B_1^+ field. Since the signal of spin density weighted MRI depends on the flip angle, inhomogeneities within the transmit field should be corrected for. Here, larger B_1 inhomogeneities lead to stronger influences on the acquired ^{23}Na data and Lommen et al. showed that B_1^+ corrections are more prone to errors with such larger variations. The B_1 fields of the utilized ^{23}Na RF coil (see section 3.1.2) have the advantage that the variations in the fields are not as pronounced (Platt, Umathum, et al., 2018).

The in section 3.2.1.4 described double angle method was thus used to measure B_1^+ fields in the context of the here presented research work. The positioning within the coil and the coil loading are the same for the B_1^+ map and the quantitative measurement as they are acquired one after the other. In earlier measurements, the classical way of acquiring two additional ^{23}Na images with flip angles α_1 and $\alpha_2 = 2 \cdot \alpha_1$ was employed, while later measurements utilized a pulse sequence with alternating excitation (Felz et al., 2023).

Relative B_1^+ maps were calculated by dividing the B_1^+ maps (α_{map}) by the flip angle α_1. These were then multiplied by the nominal flip angle α used for the quantitative ^{23}Na measurement to generate the correction factor

$$CF(\boldsymbol{r}) = \sin\left(B_{1,\mathrm{rel}}^+(\boldsymbol{r}) \cdot \alpha\right) = \sin\left(\frac{\alpha_{\mathrm{map}}(\boldsymbol{r})}{\alpha_1} \cdot \alpha\right). \tag{3.11}$$

^{23}Na image data was then corrected for B_1^+ effects by dividing by this correction factor.

3.3.4.2 B_1^- Mapping and Correction

The for this research utilized ^{23}Na RF coil (see section 3.1.2) does not share the exact same hardware for transmission and reception. This means that different field patterns are to be expected for transmit and receive field, prohibiting the use of the principle of reciprocity, which states $\boldsymbol{B_1^-} = \boldsymbol{B_1^+}$ (Hoult, 2000).

Since an inhomogeneous receive field B_1^- influences the quantification of the sodium concentration, a correction is recommended. For a homogeneous phantom of constant spin density ρ, the receive sensitivity B_1^- can be determined from the measured signal S and the flip angle α:

$$B_1^-(\boldsymbol{r}) \propto \frac{S(\boldsymbol{r})}{\sin(\alpha)}. \tag{3.12}$$

The agreement of measurement and simulation in a homogeneous phantom has been shown by Platt (2018).

Measuring B_1^- maps in vivo is challenging without a standard birdcage coil (Volz et al., 2012) or a separate transmit channel (Moortele et al., 2009) due to varying spin density. Therefore the B_1^- field distributions were simulated in a phantom model and in human voxel models using the electromagnetic field simulation software CST Studio Suite 2020/2021 (Dassault Systèmes, Vélizy-Villacoublay, France) for the in section 3.1.5 described setup.

B_1^- maps were extracted and regridded onto a homogeneous grid for the individual channels and sum-of-squares (SOS) combined.

The oval-shaped reference vials were approximated as two cylinders with a diameter of 38 mm and length of 152 mm and a cuboid connecting them with a width of 22 mm. The phantom was constructed from a cuboid with a width of 170 mm and a length of 270 mm between two ellipsoidal cylinders of the same length, a height of 16 cm and a width of 15 cm (see Figure 3.11). The corresponding dielectric properties for each of the different compartments were measured as described in section 3.3.5.

To estimated B_1^- maps for in vivo measurements, a male ("Duke", 34 years, 174 cm, 70 kg, tissue resolution $2\times2\times2\,\mathrm{mm}^3$) and a female ("Ella", 26 years, 160 cm, 58 kg, tissue resolution $2\times2\times2\,\mathrm{mm}^3$) anatomical voxel model (Christ et al., 2009) with tissue parameters from Gabriel et al. (1996), originally created as an anatomical

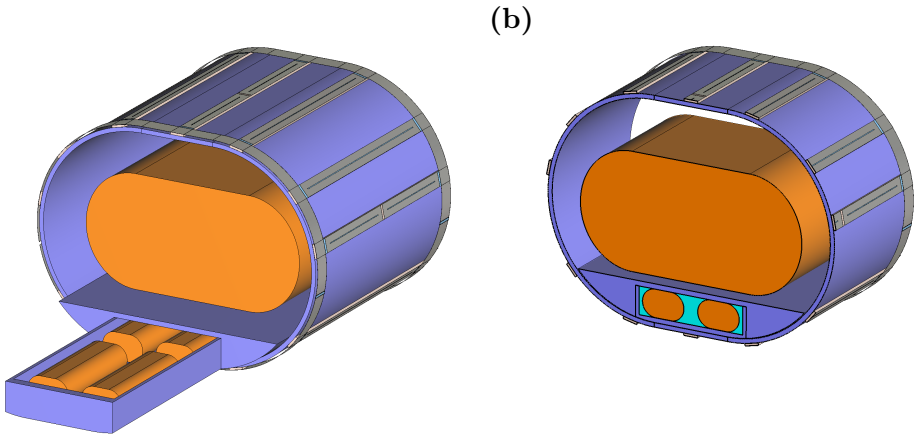

Figure 3.11: Simulation model of the reference vials and phantom in the ^{23}Na body coil for the B_1^- field determination. (a) depicts a 3D view with the calibration drawer outside of the setup and without agarose gel for demonstration purposes and (b) depicts the axial view of the positioning of the phantom and the reference vials in the ^{23}Na body coil.

model for dosimetric simulations, were used. The human voxel models were placed inside the coil on top of the reference vial setup with the kidney region positioned central inside the coil (see Figure 3.12). To fit the volunteer's anatomy, Ella was used both unscaled and scaled up isometrically by 12 %, while Duke was scaled up isometrically by 3 %.

3.3.5 Measurement of Dielectric Properties

The dielectric properties of the contents of the reference vial setup and the phantom were measured using the Dielectric Assessment Kit (DAK) with the DAK-12 Probe Geometry (Schmid & Partner Engineering AG (SPEAG), Zurich, Switzerland) shown in Figure 3.13. Each of the investigated liquids and the gel were in transparent containers (PET wide neck bottles, transparent 500 mL (neoLab Migge GmbH, Heidelberg, Germany)) which were brought into contact with the fixed probe with the use of a plastic lifting table to prevent cable movement between calibration and measurements. The probe is mounted on a mounting arm and connected to a E5061B ENA Series Vector Network Analyzer (Agilent Technologies, Santa Clara, CA, USA) for measurements of the complex reflection coefficient.

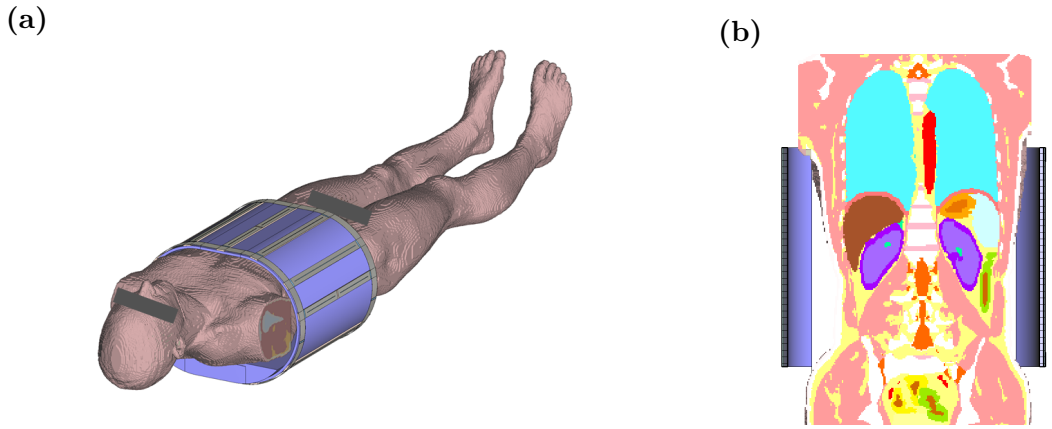

Figure 3.12: The 3D view of the placement of the isometrically by 3 % scaled human voxel model Duke and the reference vial setup in the ^{23}Na body coil is shown in (a). A section of the same model in coronal view, with the kidneys placed central inside the ^{23}Na RF coil, is shown in (b).

The measured coefficient is then converted into the complex permittivity

$$\hat{\varepsilon} = \varepsilon' - i\varepsilon'' = \varepsilon' - i\frac{\sigma}{\nu} \tag{3.13}$$

of the investigated material by the DAK software (Version: DAK 2.0.0.462). Here ε' and ε'' are the real and the imaginary part of the permittivity, respectively and σ is the conductivity.

Measurements were conducted for a frequency of $\nu = 79\,\text{MHz}$ and measurement settings in the DAK software were chosen according to the DAK Best Practices (*DAK V2.4 Application Note: DAK/DAKS Best Practices* 2017):

Source Power	0 dBm
IF Bandwidth	100 Hz
Averaging	10
Frequency Segments	10 MHz to 300 MHz in steps of 1 MHz

Deionized (DI) water at a temperature of 23.3 °C was used as the calibration liquid and the short-circuit measurement was performed with a copper strip (see Figure 3.13b), while the open-circuit measurement was performed without any load (see Figure 3.13a).

The rounded values presented in Table 4.1 were used for the electromagnetic field simulations of the receive field maps as described in section 3.3.4.2.

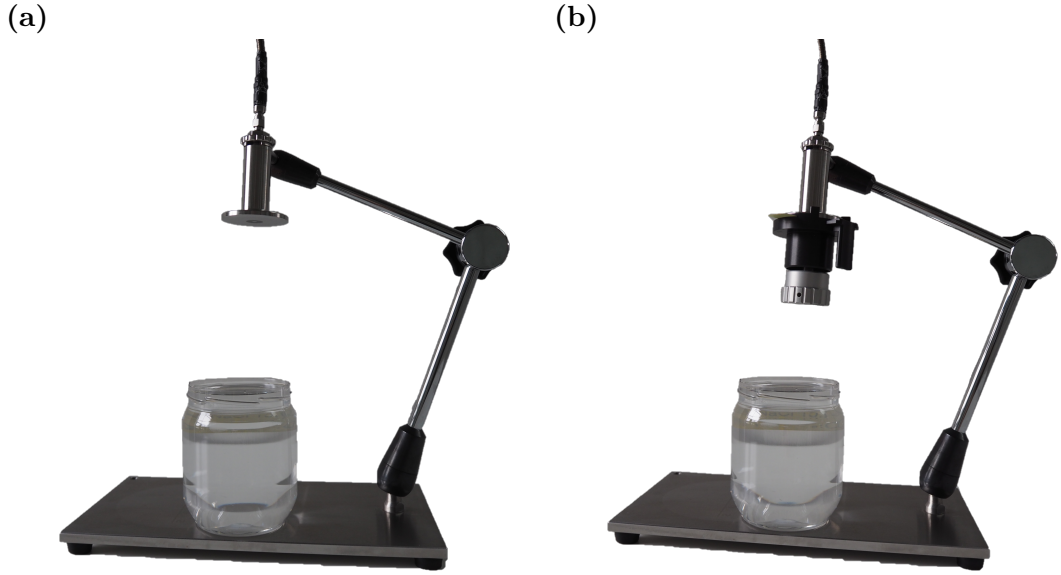

Figure 3.13: Dielectric Assessment Kit for the measurement of dielectric properties. (a) shows the open measurement (without any load) of the DAK and (b) shows the short measurement where inner and outer conductor are short-circuited with a copper strip.

3.3.6 Image Segmentation

Image segmentation is a method in digital image processing and analysis that partitions an image into multiple segments or regions, typically based on voxel characteristics. This technique can be used for various purposes, such as separating the foreground from the background or grouping voxel regions with similar features. In medical imaging, common applications include masking different tissue types, e.g. the human kidney or liver.

For this thesis, image segmentation was used to create binary masks for the reference vials used for concentration determination as described in section 3.3.8, to generate VOIs to evaluate phantom data and to segment different abdominal structures in vivo.

Since the reference vials are always positioned at the same location within the coil, the same masks in the reference vials can be used in every examination for the concentration determination and do not have to be segmented every time. To create the masks for the reference vials, a rectangular region of interest was placed inside each transversal 2D slice that contained the reference vial. The combination

of these regions was used to create a VOI as binary mask for each reference vial, which was then reused for all phantom and in vivo measurements. The masks for the 160×160×160 Matrix had a size of 5984 voxels per reference vial, corresponding to 93.5 mL. The masks were positioned in the central part of the vials to minimize partial volume effects and had less extension in the z-direction to ensure that the concentration determination was reliable. ^{1}H images were used to confirm the placement of the reference vial or to slightly shift the masks in case the volunteers had moved the reference vial setup while getting into position. For the water load experiment in section 4.3.1, images were reconstructed with a different matrix size and masks for the reference vials were adjusted accordingly. They contained 3276 voxels per reference vials, corresponding to 88.5 mL.

To fully automate the evaluation of phantom data, a mask of the full phantom VOI was created the following way. As for the in vivo data, a mask was generated from the B_1^+ data, containing only the values that were above a factor of 0.8 to 1 times the mean of the 90°. The factor was chosen depending on the application. For phantom measurements, a factor of 1 was sufficient to contain the whole phantom VOI, while the factor was reduced for in vivo measurements. In order to exclude any region that belongs to the reference vial setup from this mask, their known placement could be used to set all values below the phantom or volunteer to zero in the mask. This region is automatically determined depending on the reconstructed matrix size. After generating a mask that only contains the phantom, the outermost voxels in each direction were excluded from the mask to ensure that no partially volumed voxels were evaluated. When evaluating the mean value in the whole phantom, higher values in the central region of the uncorrected phantom concentration maps are partially compensated for by the lower apparent concentrations in peripheral regions. As the evaluated VOIs in future in vivo segmentations would additionally be much smaller, two smaller VOIs, one placed in the peripheral part of the phantom and one in a central position, were additionally evaluated. They each had a size of $16 \times 11 \times 11 = 1936$ voxel, corresponding to 30.25 mL for the reconstructed matrix sizes of $160 \times 160 \times 160$ voxel and shared one slice in the coronal direction for presentation purposes. Their placement is shown in Figure 4.2a.

For the segmentation of different abdominal structures for in vivo measurements with available ^{1}H data, MITK (Snapshots/2024-10-25, German Cancer Research Center (DKFZ), Heidelberg, Germany) was applied to the reconstructed ^{1}H data. Here, the MedSAM (Segment Anything in Medical Images) tool (Ma et al., 2024), a specialization of the the Segment Anything Model (SAM) tool (Kirillov et al., 2023) was used to create 2D masks in every slice of the ^{1}H image for small structures or

up to every three to four slices for bigger organs such as the liver. The SAM tool is a segmentation AI model that uses input prompts specifying what to segment in an image to allow to segment unfamiliar objects and images without the need for additional training. It is included in newer versions of MITK and was used to make the image segmentation less operator-dependent. 2D interpolation was used for the remaining slices to create 3D binary masks for the different target structures. All masks were saved as labels for one group in MITK, which guarantees that each voxel is only part of one mask. The created masks were then exported and used for concentration determination within the segmented regions as described in section 3.3.8. To generate the same matrix size as the ^{23}Na data, the masks were interpolated as described in section 3.3.7.

For the ^{23}Na in vivo data without ^{1}H MRI, VOIs were drawn in the same manner in MITK on the uncorrected ^{23}Na MR images as previously described for ^{1}H data.

3.3.7 ^{1}H Image Interpolation

As the proton data was acquired with a higher resolution than the ^{23}Na data (see Table 4.2) to enable the segmentation of smaller structures with higher accuracy as described in section 3.3.6, the ^{1}H data and the created masks had to be interpolated to the same matrix size as the ^{23}Na images for the quantification of the ^{23}Na concentration in the VOIs. After this they could be overlayed without image registration. Forgoing image registration has the advantage to prevent shearing, rotation or size scaling that does not stem from actual changes between scans.

For the masks that were segmented in the ^{1}H images in MITK as described in section 3.3.6, the intermediate voxels that were generated through this process were set to zero to not widen the masks of small regions and thus increase partial volume effects.

3.3.8 Concentration Determination

The sodium concentration was derived from spin density weighted images with a self-developed semi-automated segmentation tool in Matlab. The masks for the reference vials were created once as described in section 3.3.6 and could then be reused for future measurements. This increased the speed of the evaluation and removed the influence of the operator. In case of a phantom measurement, the

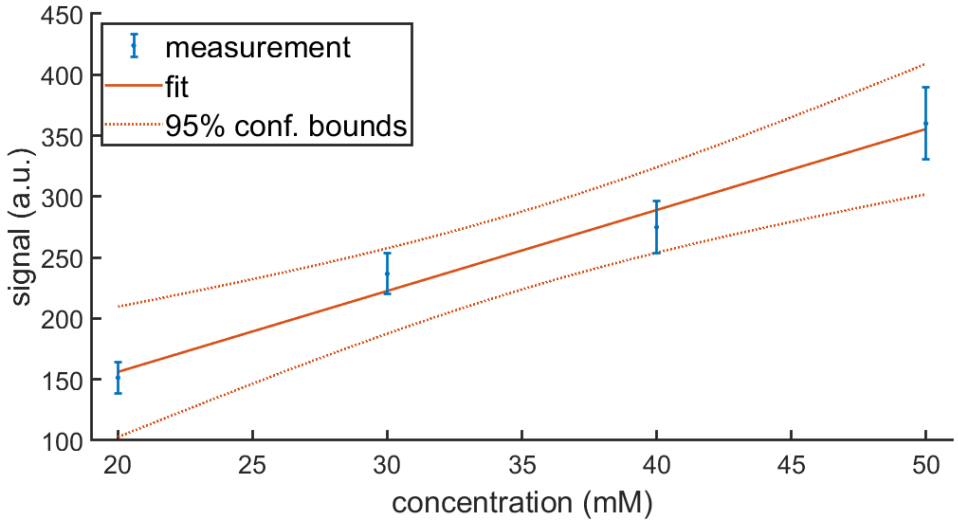

Figure 3.14: Exemplary linear regression fit of the reference vial signal intensities and the known concentrations within the vials used to assign a sodium concentration value to each voxel.

segmentation tool was fully automated, while in vivo measurements required the input of masks created in MITK as described in section 3.3.6.

Figure 3.14 shows an exemplary linear regression fit of the reference vial signal intensities and the known concentrations within the vials. The fit is used to assign a sodium concentration value to each voxel. This was repeated for an uncorrected image, an image that was T_1 corrected, an image that was T_1 and B_1^+ corrected and an image that was T_1, B_1^+ and B_1^- corrected, to evaluate the influence of the corrections on the determined apparent sodium concentration as described in section 3.3.9.

To assess how well the regression model fits the data, the R^2 value and the adjusted R^2 value ($R^2_{\text{adj.}}$) was calculated according to the following formulas:

$$R^2 = 1 - \frac{SSE}{SST} \tag{3.14}$$

$$R^2_{\text{adj.}} = 1 - \left(\frac{n-1}{n-p}\right) \cdot \frac{SSE}{SST} \tag{3.15}$$

where SST the sum of squared total (differences between the observed values and the mean of the observed values), SSE is the sum of squared error, n the number

of observations ($n = 4$ in the case of the here presented reference vial setup) and p the number regression coefficients ($p = 2$ for a linear fit, as the intercept is included).

The closer to 1 R^2 is, the more variability is explained by the linear regression model. As R^2 increases with the number of predictor variables in the regression model, $R^2_{\text{adj.}}$ adjusts for this number, which makes it more useful for comparing between models with differing number of predictor variables. As the number of external reference vials used by other sites varies, the adjusted $R^2_{\text{adj.}}$ will be used to assess the fit in the context of the here presented research work. This value can also be used to quickly realize problems in evaluations concerning the concentration determination.

Evaluation of the concentration in VOIs was performed after their segmentation as described in section 3.3.6 by calculating the mean, the standard deviation and the coefficient of variation (see section 3.3.9).

3.3.9 Influences of the Correction Approaches

Deviations from the known ground truth value of the concentration of the with a solution of a fixed sodium concentration filled phantom, can be attributed to different effects that need to be corrected in order to obtain the true concentration map.

To assess the homogeneity of the apparent sodium concentration (aSC) in the phantom after the different corrections, the coefficient of variation (CV) is used. The CV is defined as the ratio of the standard deviation σ to the mean $\bar{x}$ and is a measure for the relative dispersion in a distribution:

$$CV = \frac{\sigma}{\bar{x}}. \tag{3.16}$$

Since the mean of the concentration in different VOI vary and the standard deviation is dependent on concentration levels, the coefficient of variation instead of the standard deviation is used to compare the influence of the different correction approaches.

4 Results

In the following chapter the measurements performed to test the proposed setup and post-processing workflow for the non-invasive determination of the aTSC in a large FOV of the human torso via ^{23}Na MRI at 7 T are presented. Dielectric properties were measured for subsequent setup-specific B_1^- simulations to correct the acquired quantitative ^{23}Na MR images. Phantom measurements were used to validate the applied B_1^+ and B_1^- corrections before applying them to in vivo studies. A first in vivo study investigated the feasibility of time-resolved sodium MRI to investigate changes in the renal aTSC during a water load event. The objective of the second in vivo study was the combination of ^{1}H and quantitative ^{23}Na MR imaging at 7 T in a large FOV in the human torso under free breathing. After showing the feasibility in phantom and in vivo measurements, the aTSC was determined in several abdominal structures for three healthy volunteers.

4.1 Dielectric Properties

The dielectric properties of each reference vial liquid, the gel in the reference vial setup and the phantom content were determined for a frequency of $\nu = 79$ MHz as described in section 3.3.5. The in Table 4.1 listed results were used for the electromagnetic field simulations of the receive field map B_1^- as described in section 3.3.4.2. The resulting setup-specific B_1^- fields could then be used for corrections of the quantitative ^{23}Na image data.

4.2 Phantom Measurements

Phantom measurements were conducted to validate the post-processing workflow before applying the corrections to in vivo data. The phantom described in section 3.1.4 was used. As the need for a T_1 correction applies to all compartments

Table 4.1: Dielectric properties of the fluids and gel in the reference vial setup and phantom for a frequency of $\nu = 79\,\mathrm{MHz}$. ε' is the real part of relative permittivity, σ is the conductivity.

$[Na^+]$ ($\mathrm{mmol\,L^{-1}}$)	Agar conc. (%)	ε'	σ ($\mathrm{S\,m^{-1}}$)
20	0	79	0.22
30	0	79	0.33
35	0	79	0.38
35	2	79	0.39
40	0	79	0.44
50	0	79	0.54
60	0	79	0.64
100	0	79	1.00
140	0	79	1.39

filled with NaCl solution, the influence of the T_1 correction can only be investigated in vivo.

4.2.1 ^{23}Na MRI

A newly filled phantom and reference vial setup was used to guarantee knowledge of the accurate ground truth. It was measured three times in order to test repeatability. The second measurement was performed 12 days after the initial measurement and the third measurement was performed immediately after the second measurement. The in Table 4.2 listed acquisition parameters for the quantitative ^{23}Na MR image and the ^{23}Na B_1^+ maps were used. The phantom ^{23}Na reference voltages (see section 3.2.1.1) were 1258 V to 1267 V.

The B_1^+ and B_1^- corrections (see section 3.3.4) yield improved homogeneity within the phantom (see Figure 4.1). Figure 4.1a shows the increased homogeneity after the applied B_1^+ and after the B_1^+ and B_1^- correction. Figure 4.1b shows line plots that were drawn through a central slice in each of the in Figure 4.1a shown directions. The B_1^+ and B_1^- correction increased the homogeneity as can be seen from the flatter curves. After the B_1^+ and B_1^- correction, the aTSC along the evaluated lines corresponds well to the ground truth of 35 mM within the phantom.

As described in section 3.3.9, the CV was calculated for a VOI of the whole phantom, which was determined as described in section 3.3.6 and is depicted in Figure 4.2a. The CV decreases from 0.34 before the corrections to 0.23 after the B_1^+ correction and to 0.13 after the B_1^+ and B_1^- correction for the first measurement. For the second and third measurement the CV decrease was similar, starting at 0.36 before the corrections and decreasing to 0.25 and 0.24 after the B_1^+ correction and 0.13 and 0.14 after the B_1^+ and B_1^- correction, for the second and third measurement respectively.

Two smaller cuboid VOIs that are also shown in Figure 4.2a were placed in the peripheral and central part of the phantom to evaluate the performance of the corrections. The results are visualized in Figure 4.2b for the three measurements and show the under- (peripheral cuboid) and overestimation (central cuboid) of the aSC in the uncorrected data. Before correction, the deviation from the ground truth value of 35 mM is −5 mM and 22 mM for the peripherally placed cuboid VOI and the centrally placed cuboid VOI for the first measurement, respectively. After the B_1^+ and the B_1^- correction, the total difference from the ground truth is −1.5 mM and 0.05 mM for the peripherally placed cuboid VOI and the centrally placed cuboid VOI, respectively and thus within one standard deviation from the ground truth. The deviation from the ground truth in the uncorrected central cuboid VOI is slightly bigger for the second and third measurement compared to the first measurement, but comparable after the B_1^+ correction. For the peripheral cuboid VOI, the CV decreases from 0.15 before the corrections to 0.10 after the B_1^+ correction and to 0.06 after the B_1^+ and B_1^- correction for measurement one and two. For measurement three, the values are 0.13, 0.09 and 0.05, for the uncorrected data, the B_1^+ corrected data and the B_1^+ and B_1^- corrected data. The CV within the central cuboid VOI decreases slightly from 0.043 before the corrections to 0.040 after the B_1^+ correction and to 0.037 after the B_1^+ and B_1^- correction for the first measurement. The decrease was in a similar range for the second and third measurement.

The corrections reduce the mean CV for the four reference vials on average from 0.20 before the corrections to 0.14 after the B_1^+ and 0.09 after the B_1^+ and B_1^- correction for the first measurement. For measurement two and three the mean CV for the four reference vials reduced from 0.24 / 0.22 before the corrections to 0.16 / 0.14 after the B_1^+ and 0.09 / 0.08 after the B_1^+ and B_1^- correction, respectively. The adjusted R^2 value for the concentration fits is always high with a minimum of 0.92 before the corrections for measurement three, 0.99 after the B_1^+ correction for all measurements and a minimum of 0.97 after the B_1^+ and B_1^- correction for measurement one.

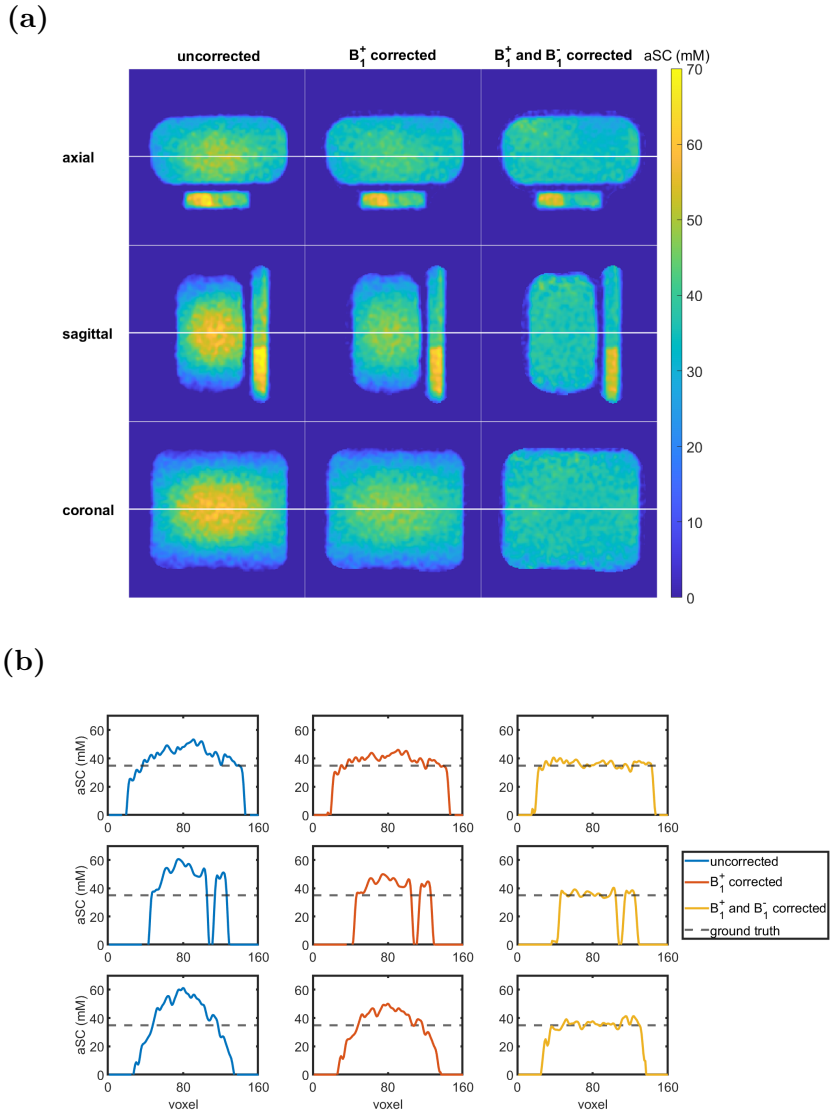

Figure 4.1: Influence of the applied corrections on the apparent sodium concentration (aSC) of a phantom filled with a homogeneous concentration of NaCl solution. The first column of (a) shows the uncorrected data, the second column the B_1^+ corrected data and the last column the B_1^+ and B_1^- corrected data for the first measurement. The plotted slices for the first two rows were chosen slightly off-center to show the concentration difference within the reference vials. (b) shows line plots through a central slice in each of the in (a) plotted directions before corrections (blue), after the B_1^+ correction (red) and after both B_1^+ and B_1^- correction (yellow).

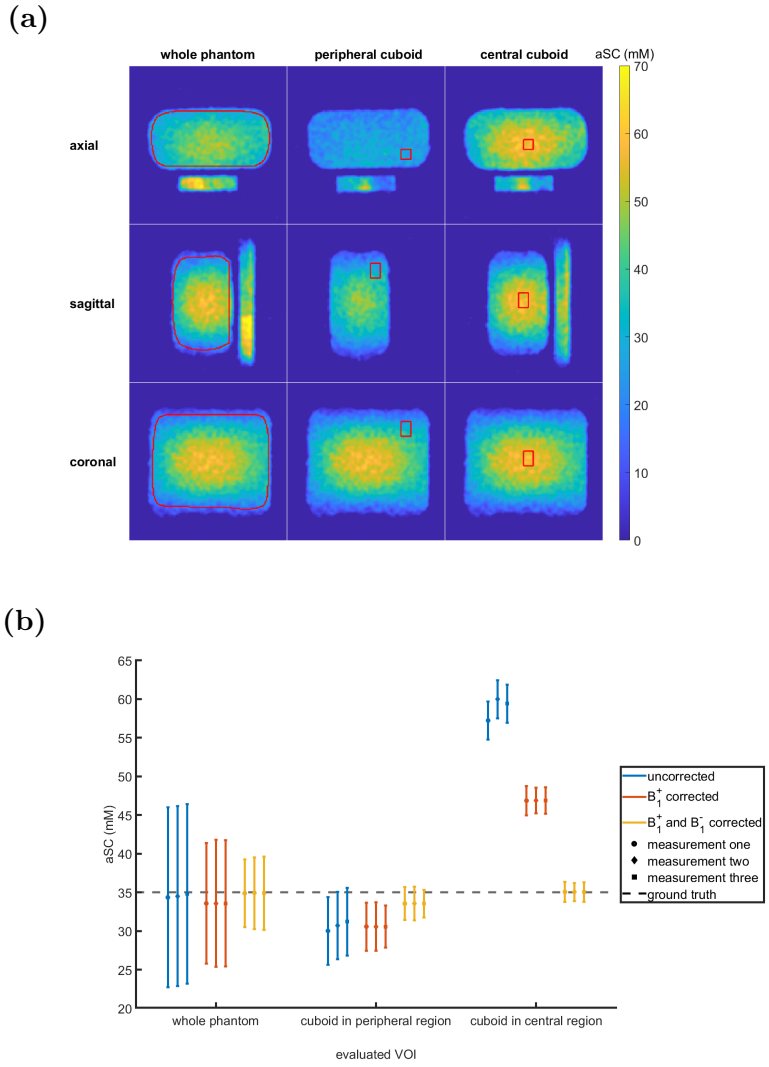

Figure 4.2: (a) shows the placement of the VOI within the phantom. The VOI for the whole phantom (left) is automatically determined from the measured B_1^+ map, the simulated B_1^- map and the placement of the reference vials. The slices in the first two rows were chosen slightly off-center to depict the concentration difference within the reference vials. The placement of the additionally evaluated cuboid VOI in the peripheral (middle) and central (right) part of the phantom are shown for different slices in the axial and sagittal view but in the same coronal slice (last row). (b) shows the comparison of the determined aSC within the phantom before corrections (blue), after the B_1^+ correction (red) and after both B_1^+ and B_1^- correction (yellow) for the three in (a) shown VOI for each of the measurements as denoted by different markers.

Between the three measurements depicted in Figure 4.2b, the mean determined aSCs within the three VOI before corrections are (35 ± 7) mM, (31 ± 2) mM and (58.9 ± 1.3) mM, with the standard deviation determined from Gaussian error propagation. After B_1^+ corrections the aSC for all VOI shows a smaller standard deviation, thus showing increased homogeneity. For the three VOI the determined aSCs are (34 ± 5) mM, (31.0 ± 1.7) mM and (47.4 ± 1.0) mM. After additionally correcting with the setup-specific simulated B_1^- map, the mean determined aSC within the whole phantom VOI was (35 ± 3) mM. For the smaller VOIs in the peripheral and central part of the phantom the mean was found to be (33.8 ± 1.2) mM and (35.1 ± 0.7) mM, respectively. Thus, after applying the corrections from measured B_1^+ maps and the setup-specific simulated B_1^- maps, the aSC determined in the whole phantom as well as in smaller VOIs in peripherial and central parts of the FOV was within one standard deviation of the ground truth value of 35 mM with a maximal difference of 3.4 %. In all cases the variation between the three measurements was found to be small with a standard deviation of 0.2 mM for the whole phantom VOI and 0.3 mM and 0.06 mM for the peripheral and central cuboidal VOI, respectively.

4.2.2 ^{23}Na and ^{1}H MRI

Phantom measurements of ^{23}Na and ^{1}H data in the same acquisition were acquired to test the alignment of the data in order to forgo image registration.

Proton images were acquired as described in section 3.2.2. The phantom ^{23}Na reference voltage (see section 3.2.1.1) was $U_{\text{ref}} = 1267$ V. The acquisition parameters are listed in Table 4.2.

Figures 4.3 and appendix A1 to A2 show that the ^{23}Na and ^{1}H MR data match in position after the reconstruction of the ^{23}Na and ^{1}H data (see section 3.3.1 and 3.3.2) and interpolation of the ^{1}H data (see section 3.3.7). Each line plot through the phantom for the ^{23}Na and ^{1}H MR images shows a good correspondence of the border of the phantom and reference vial setup between the ^{23}Na and ^{1}H MR data. This allowed overlaying the images without image registration.

Table 4.2: Acquisition parameters and reconstruction settings for the different employed sequences for the phantom and in vivo measurements of combined ^{23}Na and ^{1}H MRI.

	Quantitative ^{23}Na image	**^{23}Na B_1^+ map (alternating excitation)**	**^{1}H 3D GRE-RPE static pTx**
T_E (ms)	1	1.65	2.04
T_R (ms)	150	106/168 (alternating)	4.23
Nominal FA (°)	61	45/90 (alternating)	11
Acquired isotropic nominal resolution (mm)	5	20	1.25
Number of projections	10000	1020	-
Number of RPE lines	-	-	1536
Radial samples	256	256	-
Acquisition time (min:s)	25:00	4:39	17:20
Pulse duration (ms)	1.8	3	1
Readout duration (ms)	5	3.33	-
Bandwidth (Hz/Px)	-	-	1042
Acquired data points in k-space center	2	2	-
B_1^+ shim mode	-	-	TIAMO (2 modes)
Zerofilling factor	2	8	-
Filter	Hamming	Gauss (σ=20mm)	-
reconstructed FOV (mm^3)	400 × 400 × 400	400 × 400 × 400	400 × 400 × 400

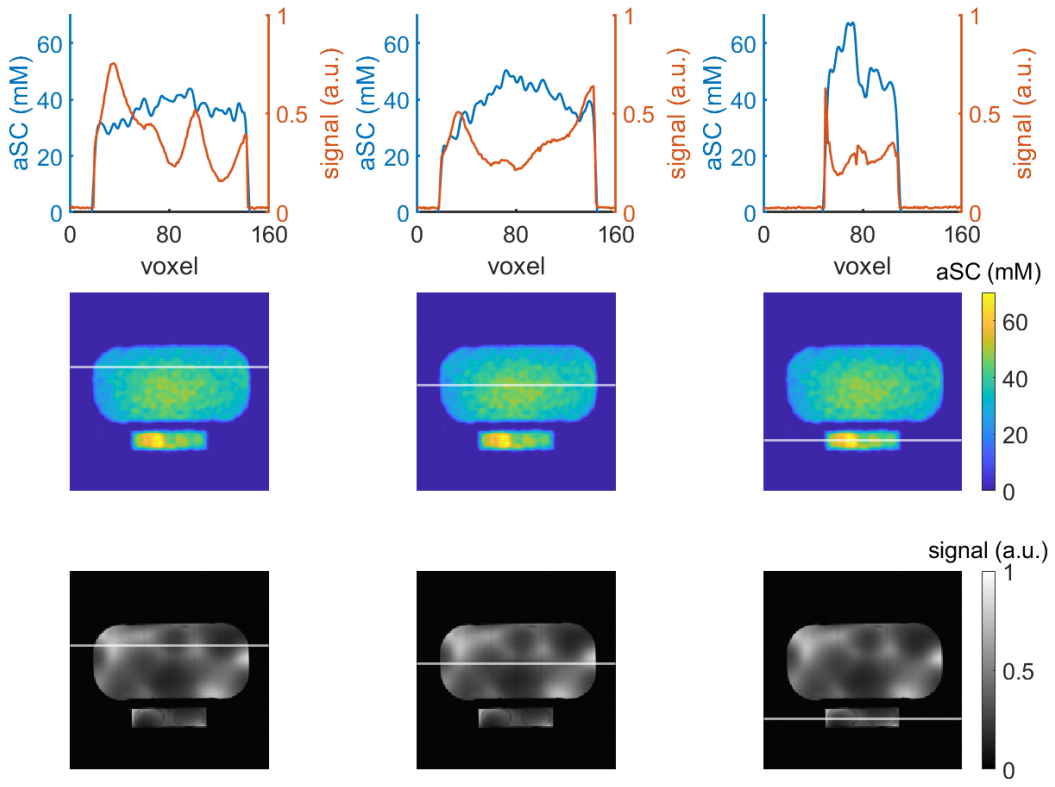

Figure 4.3: Alignment of ^{23}Na and ^{1}H images in the phantom for the left-right direction in a transversal slice. The line plot in the first row displays the values in the uncorrected ^{23}Na (blue line) and ^{1}H (orange line) MRI along the white line in the second and third row, respectively. For each plotted line through the phantom, the border of the phantom and reference vials in the ^{23}Na image corresponds well to those in the ^{1}H image. In the third column, where the values depicted are only in the reference vials, the sodium images, as expected, show a clear difference between the two reference vials with differing concentrations despite remaining inhomogeneities in the uncorrected image.

Table 4.3: Acquisition parameters and reconstruction settings for the ^{23}Na in vivo water load measurements.

	^{23}Na B_1^+ map	**Quantitative ^{23}Na image (long)**	**Quantitative ^{23}Na image (short)**
T_E (ms)	1.65	1	1
T_R (ms)	150	100	100
Nominal FA (°)	45/90	61	61
Acquired isotropic nominal resolution (mm)	10	6	6
Number of projections	4100	36000	9000
Radial samples	256	256	256
Acquisition time (min:s)	10:15/10:15	60:00	15:00
Pulse duration (ms)	3	1.8	1.8
Readout duration (ms)	5	5	5
Acquired data points in k-space center	0	2	2
Zerofilling factor	3.34	2	2
Filter	Gauss (σ=20mm)	Hamming	Hamming
reconstructed FOV (mm^3)	396 × 396 × 396	396 × 396 × 396	396 × 396 × 396

4.3 In Vivo Measurements

In vivo studies were approved by the ethics committee of the Medical Faculty Heidelberg, Germany (S-154/2014). Written, informed consent was obtained from all participants included in measurements prior to their examinations.

Earlier in vivo measurements were performed in a head first supine position, but in later measurements the feet first supine position was used in order to increase space for the arms above the head. Each position used for the specific measurement will be noted in the respective sections.

As the T_1 correction is applied to all reference vials in the same manner, the correction has no influence on the CV of the aSC within the reference vials or the R^2 of the determined fit. For this reason, these values are not reported separately and are equivalent to the reported values for the uncorrected case.

4.3.1 Renal ^{23}Na MRI Before, During and After a Water Load

Two healthy female volunteers (age: 32 and 27 years, weight: 85 kg and 65 kg, height: 180 cm and 177 cm) abstained from drinking or eating at least 13 hours prior to the ^{23}Na MRI to achieve water deprivation. Measurements were performed in the head first supine position. The ^{23}Na reference voltage (see section 3.2.1.1) was 1364.8 V and 1360.0 V for volunteer one and two, respectively. B_1^+ maps were measured first, followed by a 1 h DA-3DPR measurement and an additional 15 min DA-3DPR measurement. The measurements were performed in this order and subdivided like this as it was unclear how long the volunteers could stay in the scanner after the water load. 20 min into the 1 h measurement, the volunteers drank 629 mL and 1044 mL from a water (Na^+: 20 mg L^{-1}) reservoir (see section 3.1.6).

For the sliding window evaluation, the 1 h image and the 15 min image were concatenated and subsets of 4500 projections (7.5 min duration each) with an overlap of 2250 projections were reconstructed, separately applying a Hamming filter and a zerofilling factor of 2. For the reconstruction of the flip angle map measurements, a Gaussian filter and zerofilling to achieve the same matrix size and FOV as the quantitative images was applied. To reduce the undersampling in the subsets, imaging parameters were adjusted according to Table 4.3, choosing larger voxel sizes and a shorter repetition time.

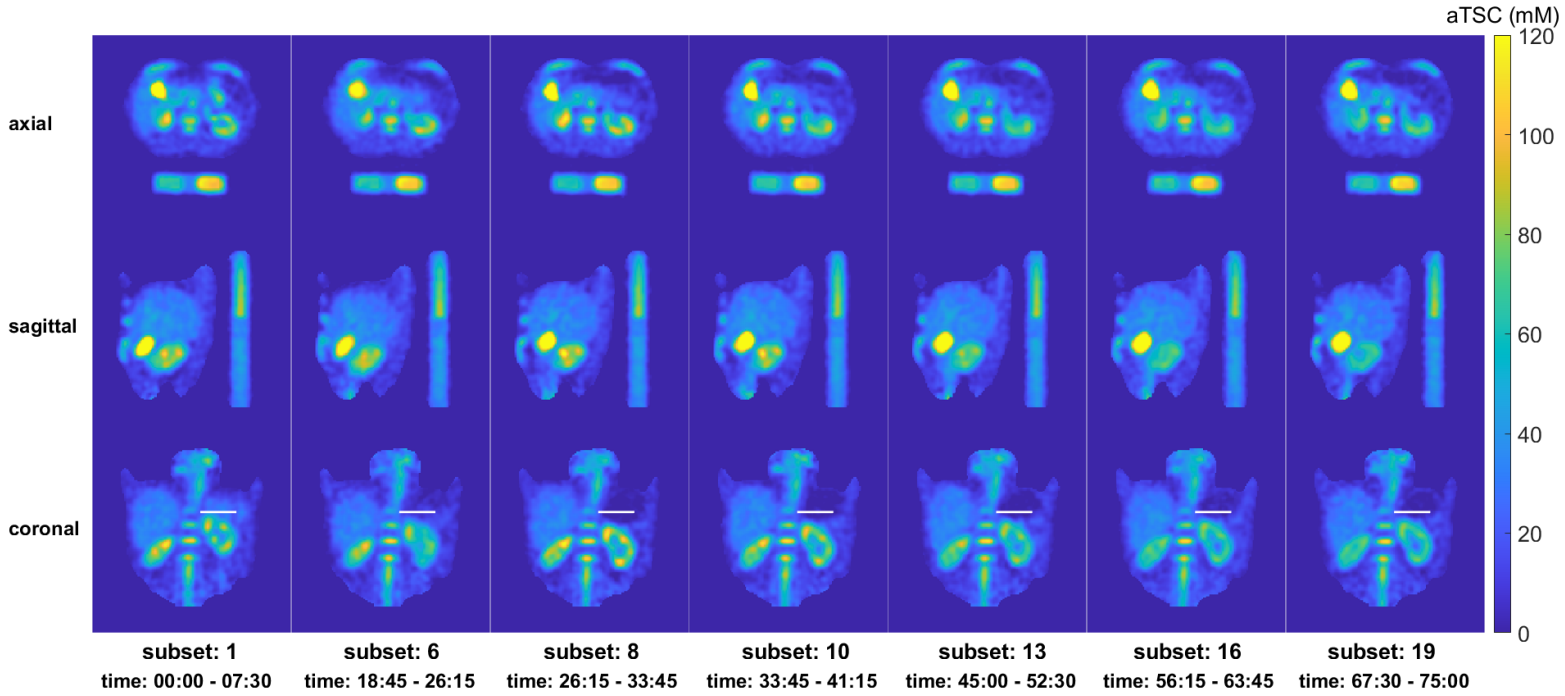

Figure 4.4: Quantitative ^{23}Na concentration maps for volunteer one for a selection of the evaluated subsets during the water load measurement. At t = 20 min, volunteer one drank 629 mL of water (Na^+: 20 mg L^{-1}). Slices in each orientation were chosen to visualize the kidneys. The high signal intensity in the axial and sagittal slices stems from the gallbladder. For the coronal slices, white lines were added to visualize the movement of the left kidney throughout the experiment.

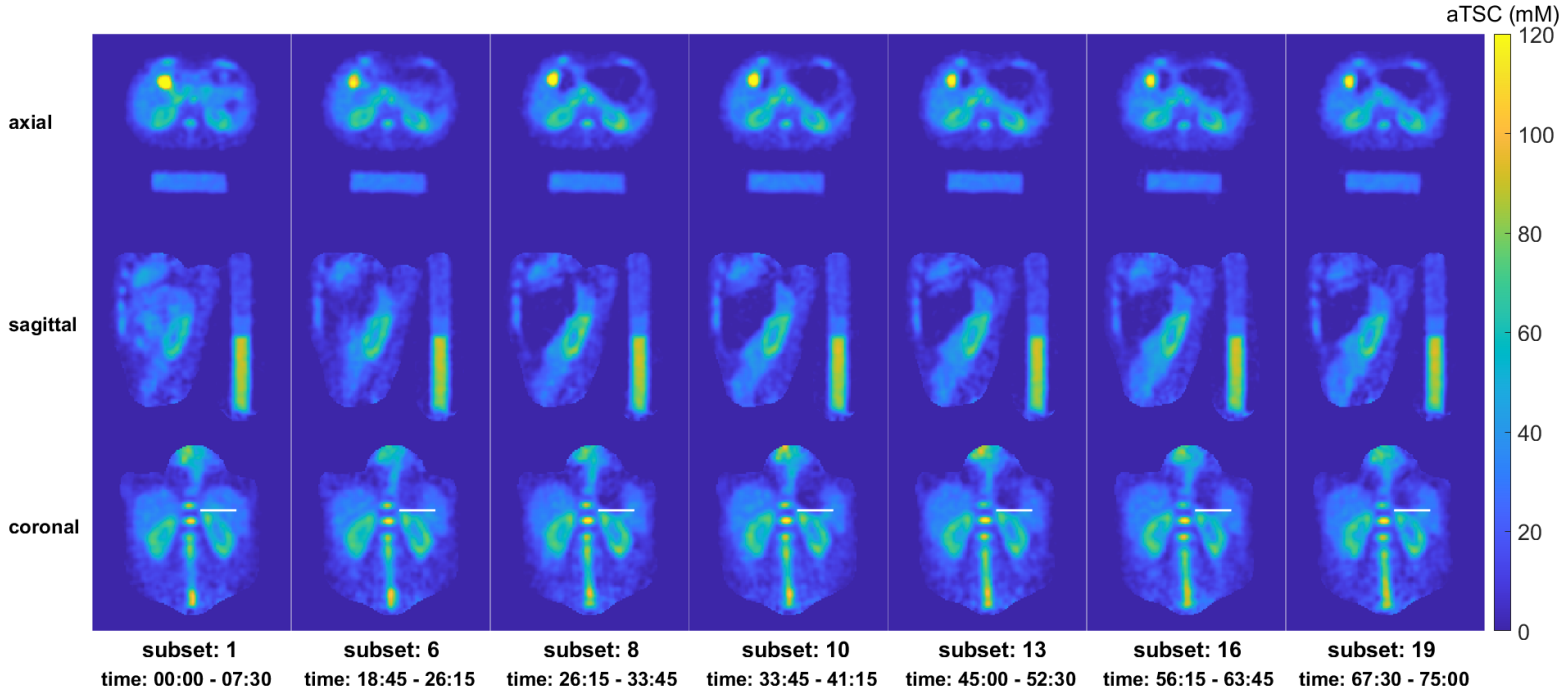

Figure 4.5: Quantitative ^{23}Na concentration maps for volunteer two for a selection of the evaluated subsets during the water load measurement. At t = 20 min, volunteer two drank 1044 mL of water (Na^+: 20 mg L^{-1}). Slices in each orientation were chosen to visualize the kidneys. The high signal intensity in the axial slices stems from the gallbladder. For the coronal slices, white lines were added to visualize that movement of the left kidney throughout the experiment in caudal direction was minimal compared to volunteer one.

Resulting images were corrected for T_1 relaxation effects in the reference vials (see section 3.3.3) as well as for B_1^+ (see section 3.3.4.1) and B_1^- effects (see section 3.3.4.2). Before corrections, the minimal adjusted R^2 for the linear regression fit in the reference vials of any subset of the measurement for volunteer one was 0.95. After the B_1^+ and B_1^+ and B_1^- correction it increased to 0.97 and 0.98, respectively. For volunteer two the minimal adjusted R^2 for any of the subsets was 0.97 before the B_1 corrections and 0.98 after the B_1^+ and 0.99 after the B_1^+ and B_1^- correction, respectively. The maximal CV for the mean of the four reference vials for any subset for volunteer one before corrections was 0.16. After the B_1^+ and after B_1^+ and B_1^- correction it decreased to 0.14 and 0.10, respectively. For volunteer two this value decreased from 0.15 before B_1 corrections to 0.13 and 0.09 after only B_1^+ and after B_1^+ and B_1^- correction, respectively.

The resulting quantitative ^{23}Na maps for some of the subsets for volunteer one are shown in Figure 4.4 and in Figure 4.5 for volunteer two. For the coronal slices, lines are added to show the displacement of the left kidney throughout the measurement time for volunteer one compared to a fairly stationary left kidney in volunteer two. Kidney placement between both volunteers was very similar, as can be seen by the white line which was placed at the same height for both volunteers. For the subsets after the water intake, a signal decrease can be seen in the stomach for both volunteers.

The regions of interest were drawn in each ^{23}Na MR image subset as described in section 3.3.6 and concentration maps were generated as described in section 3.3.8. As there was no visible change in organ position for the first three subsets in volunteer one, the same mask was used for these subsets. Exemplary masks for three different subsets are shown in Figure 4.6 and the number of voxels contained in the mask for each subset for the two volunteers is depicted in Figure 4.7. For volunteer one, the number of voxels in the mask slowly increases for later subsets, while the overall trend for volunteer two is opposite. Figure 4.7 also depicts the corresponding volume for the evaluated masks in mL on the right y-axis. Here, the volume of the mask corresponding to volunteer one's left kidney is the highest. The difference in evaluated kidney volume between left and right kidney for volunteer one is much more pronounced compared to volunteer two, where the changes over time are in the same order as differences between different subsets and between the two kidneys. The size of the masks for volunteer one varied between 146 mL to 173 mL and 179 mL to 212 mL for the right and left kidney, respectively, with smaller mask sizes primarily in the beginning. For volunteer two, the size of the masks ranged from 116 mL to 147 mL and 118 mL to 167 mL for the right and left kidney, respectively. The kidney volume was determined in ^{1}H images at 3 T

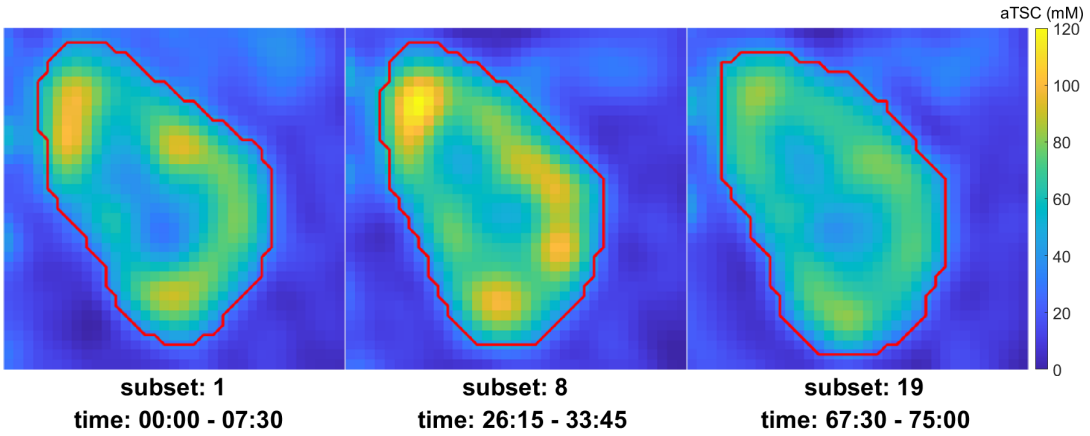

Figure 4.6: Close up of the left kidney of volunteer one for water deprivation (subset 1), shortly after the water load (subset 8) and at the end of the measurement (subset 19) with the respective masks for the shown slice central within the left kidney. The images were cut to align the kidneys, resulting in image parts that are shown to be shifted by 7 and 4 voxel in caudal direction for the 8^{th} and 19^{th} subset, respectively.

as described by Daniel et al., 2021. The volume for the right and left kidney of volunteer two was 157.2 mL and 135.3 mL, respectively. The resulting total kidney volume for both kidneys of 292.5 mL is well within their reported total kidney volume for healthy controls of (296 ± 38) mL measured in the 25 volunteers used for training the neural network in Daniel et al. (2021). The masks generated for each subset during the sliding window evaluation were thus in a similar size as expected from ^{1}H images despite the segmentation in ^{23}Na MR images.

The aTSC within the left and right kidney were evaluated for each subset and are plotted over the course of the measurement in Figure 4.8. The subsets containing projections during the water uptake are indicated by yellow shading. Values before the water intake are fairly constant at around (64 ± 21) mM and (60 ± 18) mM for the right and left kidney of volunteer one, respectively. During the water load, the aTSC in both kidneys of volunteer one decreases, followed by an increase for the two subsets after the water load and slow decrease thereafter. At the end of the measurement, the aTSC in the right and left kidney of volunteer one are (54 ± 13) mM and (55 ± 16) mM, respectively. It can also be seen that the standard deviation of the measured aTSC decreases as the aTSC decreases after the water load, which corresponds to a reduction in the cortico-medullary sodium gradient. For volunteer two, the small increase in the aTSC after the water load, quickly decreases back to a similar aTSC as before the water load. No big change in

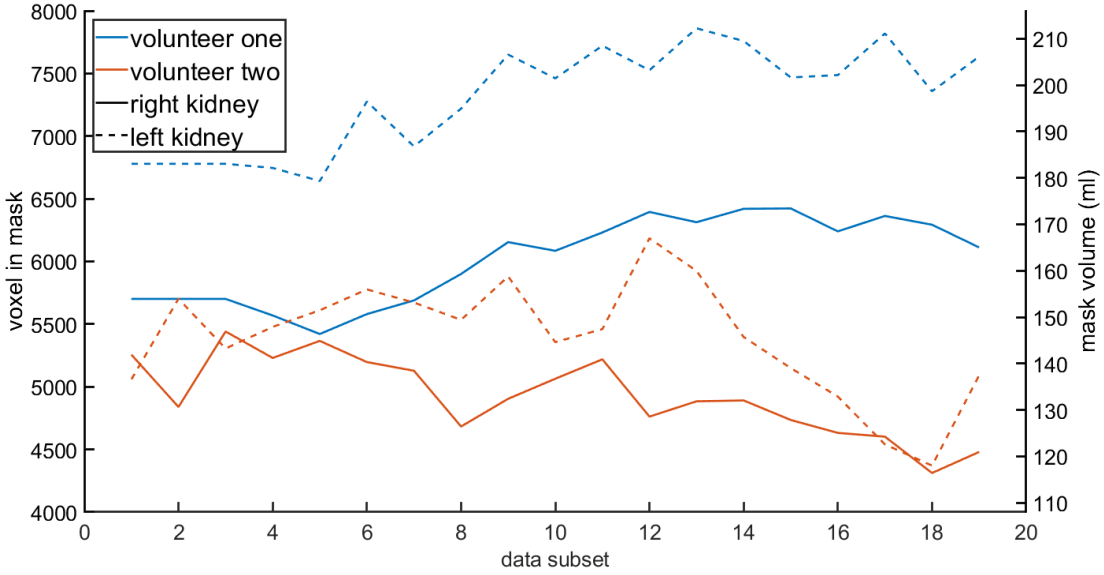

Figure 4.7: Number of voxels in the masks of the right (solid line) and left (dashed line) kidneys of volunteer one (blue) and two (orange) over the course of the water load experiment. The right y-axis displays the corresponding volume in mL.

the aTSC in either kidney could be observed. The aTSC before and after the water load are (55 ± 11) mM and (57 ± 11) mM for the right and (52 ± 12) mM and (53 ± 13) mM for the left kidney. The standard deviation is slightly smaller in the right kidney compared to the left kidney for both volunteers.

As the kidneys moved less for volunteer two, the same mask was evaluated for all subsets to evaluate the influence of the evaluated volume on the aTSC. The resulting aTSC for each subset are shown in Figure 4.9. Compared with Figure 4.8b larger standard deviations for the left kidney can be observed after the water load while the overall time evolution of the aTSC is similar. After an initial increase in aTSC shortly after the water load, the aTSC in both kidneys reaches values of before the water load within around 25 min and is slightly more stable throughout the later subsets compared to the time series with individual masks shown Figure 4.8b.

To assess the cortico-medullary sodium gradient further, line plots as shown in Figure 4.10 were evaluated on a voxel-by-voxel basis. Here, a prominent medulla of the left kidney was chosen for the first subset, the 8^{th} subset (shortly after the water load) and the last subset (19^{th} subset). Maril, Rosen, et al. (2006) report that the coronal plane is the optimum plane for visualizing the sodium distribution

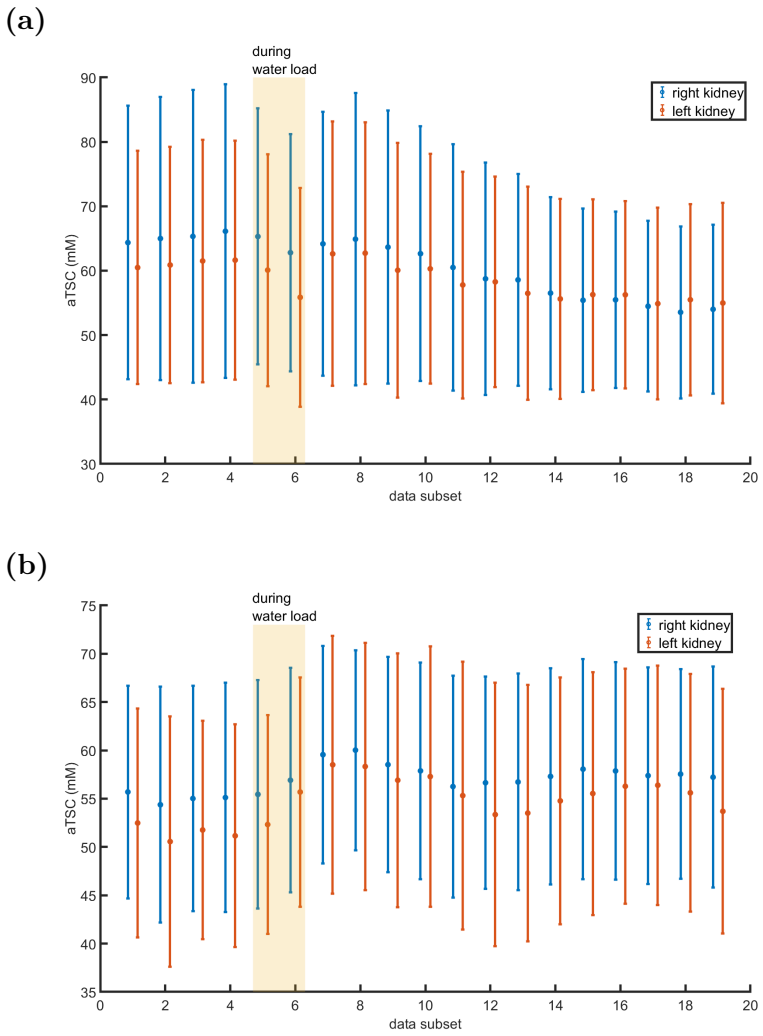

Figure 4.8: Change in concentration in the left and right kidney of volunteer one (a) and two (b) after T_1, B_1^+ and B_1^- corrections during the course of the water load measurement. Each data subset consists of 4500 projections, corresponding to a measurement time of 7.5 min and an overlap of 2250 projections. Datasets corresponding to the time of the water uptake are indicated by the shaded area. The error bars show the standard deviation within the evaluated VOI that was segmented for each subset.

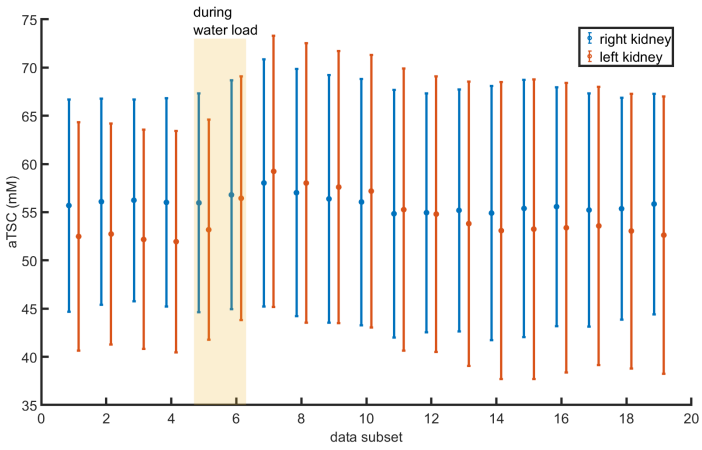

Figure 4.9: Change in concentration in the left and right kidney of volunteer one after T_1, B_1^+ and B_1^- corrections during the course of the water load measurement. Each data subset has a length of 4500 projections, corresponding to a measurement time of 7.5 min and an overlap of 2250 projections. Datasets corresponding to the time of the water uptake are indicated by the shaded area. The error bars show the standard deviation within the evaluated VOI that was segmented for the first subset.

in the human kidney, which is why this plane was chosen for this evaluation.

As the left kidney moved for the later times for volunteer one due to the water load (see Figure 4.4), the image parts that are shown in Figure 4.10a were shifted by 7 and 4 voxel for the 8^{th} and 19^{th} subset, respectively. As the reconstructed matrices have a resolution of 3 mm, this corresponds to a displacement of 2.1 cm and 1.2 cm in caudal direction. Movement in other directions was less pronounced.

As can be observed in the line plots in Figure 4.10a, the cortico-medullary gradient first increases shortly after the water load, before it decreases later during the measurement. While the value for the cortex stays between 52 mM to 58 mM, the aTSC in the observed medulla increases from 99 mM for water deprivation, to 120 mM shortly after the water load and then decreases to around 82 mM at the end of the measurement. This results in ratios of medulla to cortex aTSC of 1.71, 2.08 and 1.43 before, shortly after and long after a water load for volunteer one. For volunteer two the same evaluation was performed for the same subsets and is shown in Figure 4.10b. The left kidney stayed almost at the same position and only a shift of 1 voxel in medial direction was needed. Visually a generally lower aTSC within the medullae can be observed for volunteer two compared to

volunteer one. A slight increase of the aTSC in the medulla from 74 mM before the water load to 90 mM shortly after the water load can be observed, followed by a decrease to 80 mM at the end of the measurement. For the cortex, the respective values are 40 mM, 48 mM and 43 mM before, shortly after and long after the water load respectively. The ratios of medulla to cortex aTSC for volunteer two are 1.56, 1.89 and 1.69 before, shortly after and long after a water load. For both volunteers, the reported change is for a distance of 12 mm between cortex and medulla values.

4.3.2 ^{23}Na and ^{1}H MRI in a Large Field-of-View

To access the aTSC in several organs at once, quantitative ^{23}Na MRI was combined with ^{1}H MRI in a large FOV. The acquisition parameters are the same as those for the phantom measurements in section 4.2.2 listed in Table 4.2 with a total acquisition time of 46 min and 59 s.

Three healthy volunteers (2 female, 1 male, age: 35, 26 and 22 years, weight: 85 kg, 56 kg and 85 kg, height: 180 cm, 160 cm and 184 cm) abstained from drinking and eating for at least 9 hours before the measurements to generate a similar and more repeatable physiological state. The volunteer's kidneys were positioned approximately at the center of the ^{23}Na RF coil along the z axis, utilizing ^{1}H localizer images to verify the volunteer's position within the RF coil before starting the measurements. All sequences were acquired under free breathing without triggering and in a feet first supine position with arms and hands placed above the head. The range of the in vivo reference voltage U_{ref} was 1304 V to 1379 V.

The applied corrections improved the mean CV for the four reference vials on average from 0.15 before the corrections to 0.13 and 0.09 after the B_1^+ and after the B_1^+ and B_1^- correction, respectively. The mean adjusted R^2 for the concentration fits improved slightly from 0.990 before the B_1 corrections to 0.996 and 0.997 after the B_1^+ and after the B_1^+ and B_1^- correction, respectively.

The 3D ^{1}H image, the corresponding quantitative aTSC map after corrections as well as an overlay of both for one of the volunteers is shown in Figure 4.11. Figure 4.12 shows an overview for the other volunteers that were measured. The success of the overlay of the ^{1}H and ^{23}Na images can be assessed particularly well in the intervertebral discs (IVD), renal and reference vial areas.

The ^{1}H images before interpolation shown in Figure 4.13 were used for segmen-

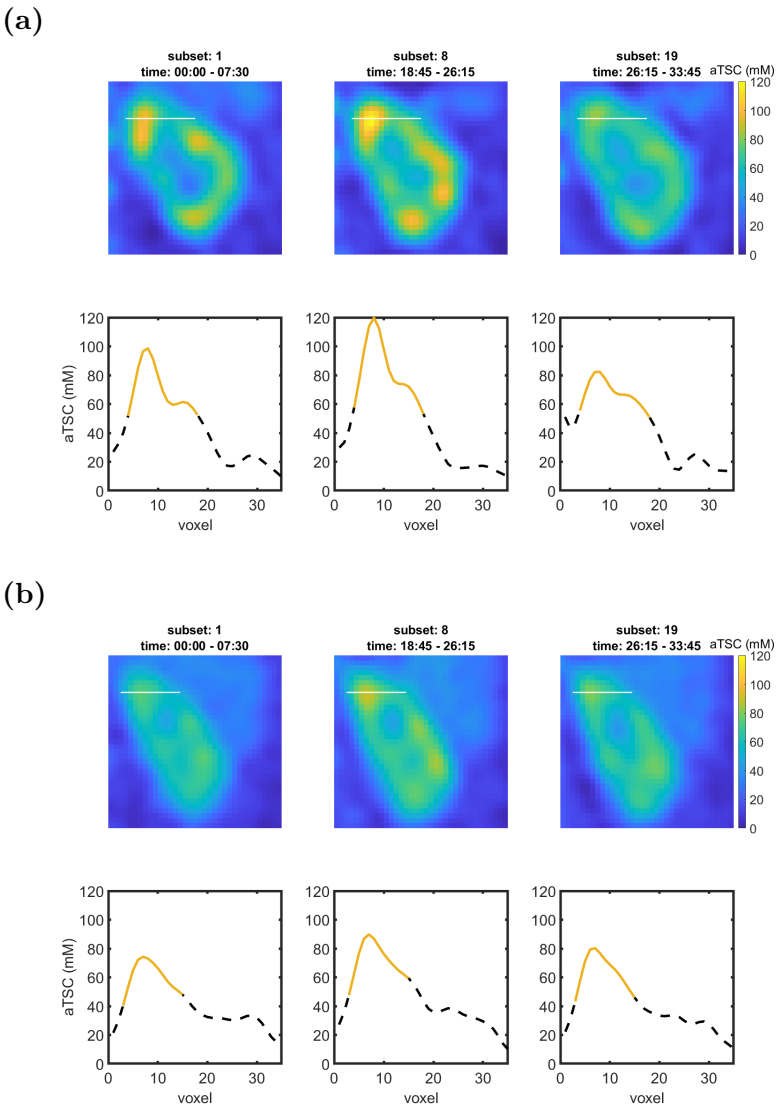

Figure 4.10: The first rows show close ups of a central slice of the left kidney of volunteer one (a) and two (b) for water deprivation (subset 1), shortly after the water load (subset 8) and at the end of the measurement (subset 19). The images were cut to align the kidneys, resulting in image parts that are shown to be shifted by 7 and 4 voxel, corresponding to 2.1 cm and 1.2 cm in caudal direction for the 8^{th} and 19^{th} subset for volunteer one, respectively. The second rows show line plots along the in the first row drawn white lines through a prominent medulla (solid line) and the surrounding cortex. The dashed lines show the values if the lines were elongated to cover the whole shown area.

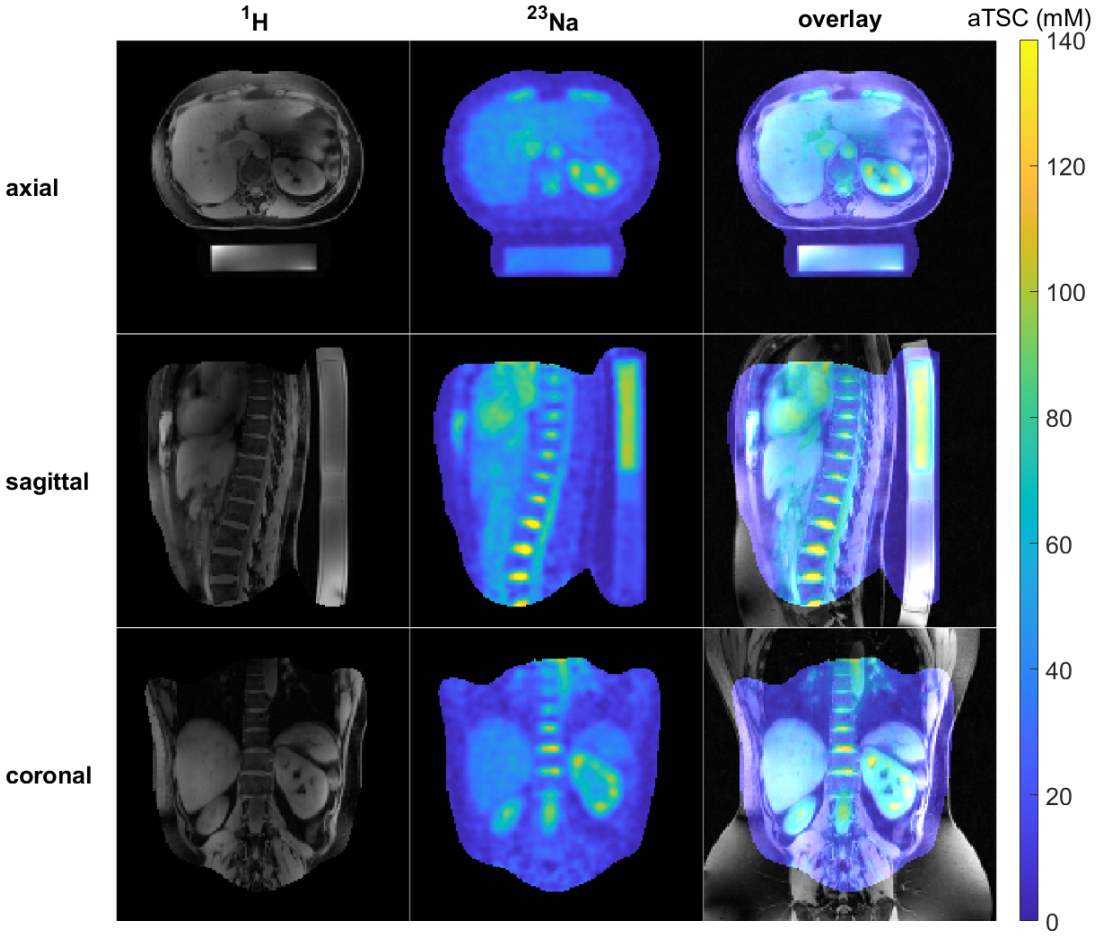

Figure 4.11: ^{1}H 3D GRE-RPE static pTx images (left), quantitative ^{23}Na images (middle), and overlay of both (right) for the first volunteer. The ^{1}H and ^{23}Na images are both masked with the same mask for easier comparison while the ^{1}H image in the right column is unmasked to show the full FOV.

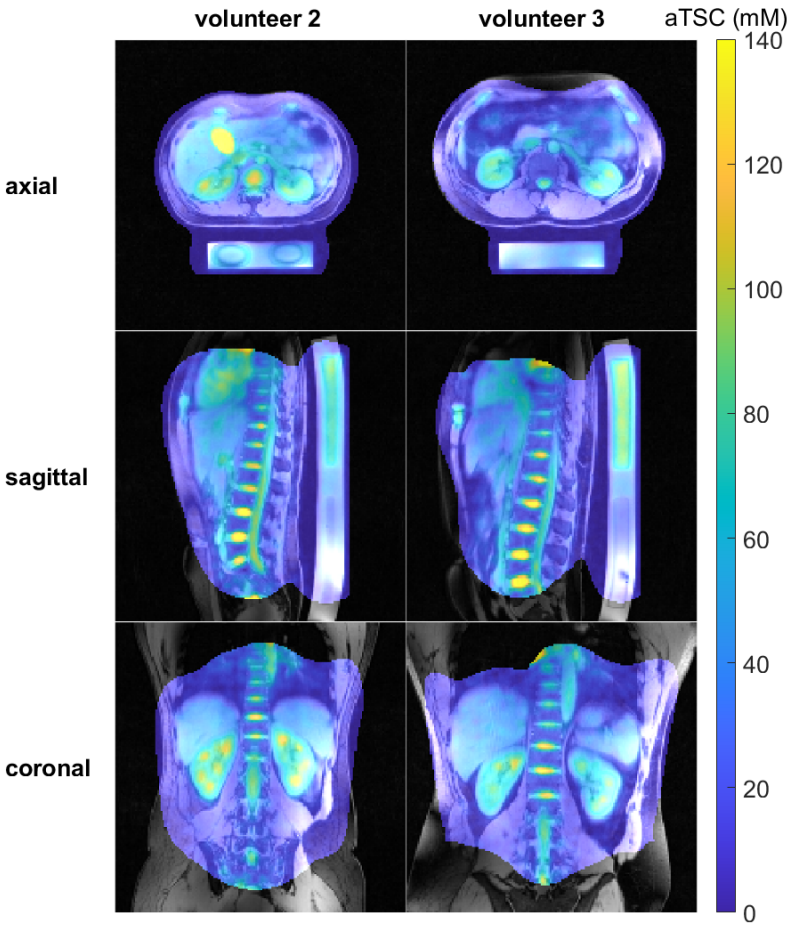

Figure 4.12: Overlay of ^{1}H 3D GRE-RPE static pTx images and quantitative ^{23}Na images for volunteer two and three.

tation of several abdominal structures with MITK as described in section 3.3.6. As can for example be seen in the upper parts of the liver in coronal view, there are some remaining signal variations due to transmit field inhomogeneities. Signal dropouts can for example be observed in the hip region of volunteer one and three in coronal view. Despite some remaining signal dropouts, the image quality was sufficient for segmentation of most organs and other structures without the need for many manual alterations. It should be noted that the IVC and gallbladder are frequently classified as liver tissue by the MedSAM algorithm (see section 3.3.6) if not segmented before the liver, as they are surrounded by liver tissue or are nearby, with a visible but not outstanding contrast.

The generated masks were interpolated to match the ^{23}Na image resolution, discarding voxels with values other than one due to the interpolation. The resulting masks were used to access the aTSC in the respective structure. For the research work presented here, masks were created for the liver, kidneys, inferior vena cava (IVC), CSF, spleen, gallbladder and IVD and the resulting aTSC values are summarized in Table 4.4, Table 4.5 and Table 4.6. An exemplary visualization is depicted in Figure 4.14 for volunteer two. Here the masks of the liver, kidneys and a subset of the IVDs are shown. In contrast to the overlay images in Figure 4.11 and 4.12, the ^{1}H MR image are not displayed in the masked regions to allow a visual assessment of the aTSC for the depicted organs and IVDs.

As can be observed from Table 4.4, the aTSC decreased through the T_1 correction and increased through the B_1^+ and B_1^- corrections. With the exception of the spleen, the aTSC for the female volunteers is larger compared to the male volunteer (volunteer three).

For volunteer one, the difference in aTSC determined by manually excluding visible blood vessels in addition to the IVC from the liver mask was investigated. Before corrections, the aTSC for the liver mask without blood vessels was (26 ± 8) mM. After the T_1 correction, the value decreased to (25 ± 8) mM. After the T_1 and B_1^+ correction, the aTSC in the liver was measured as (29 ± 9) mM. After all corrections, the aTSC for the liver mask without blood vessels was found to be (36 ± 11) mM. This is a change of $-5\,\%$ to the value of the aTSC for the liver mask with the blood vessels, but comes at the expense of more manual segmentation time per volunteer.

The aTSC after all corrections for each of the investigated abdominal structures in Table 4.4 for the three volunteers is displayed in Figure 4.15. The values for the IVDs were evaluated together and are, as the value for CSF, likely to be underesti-

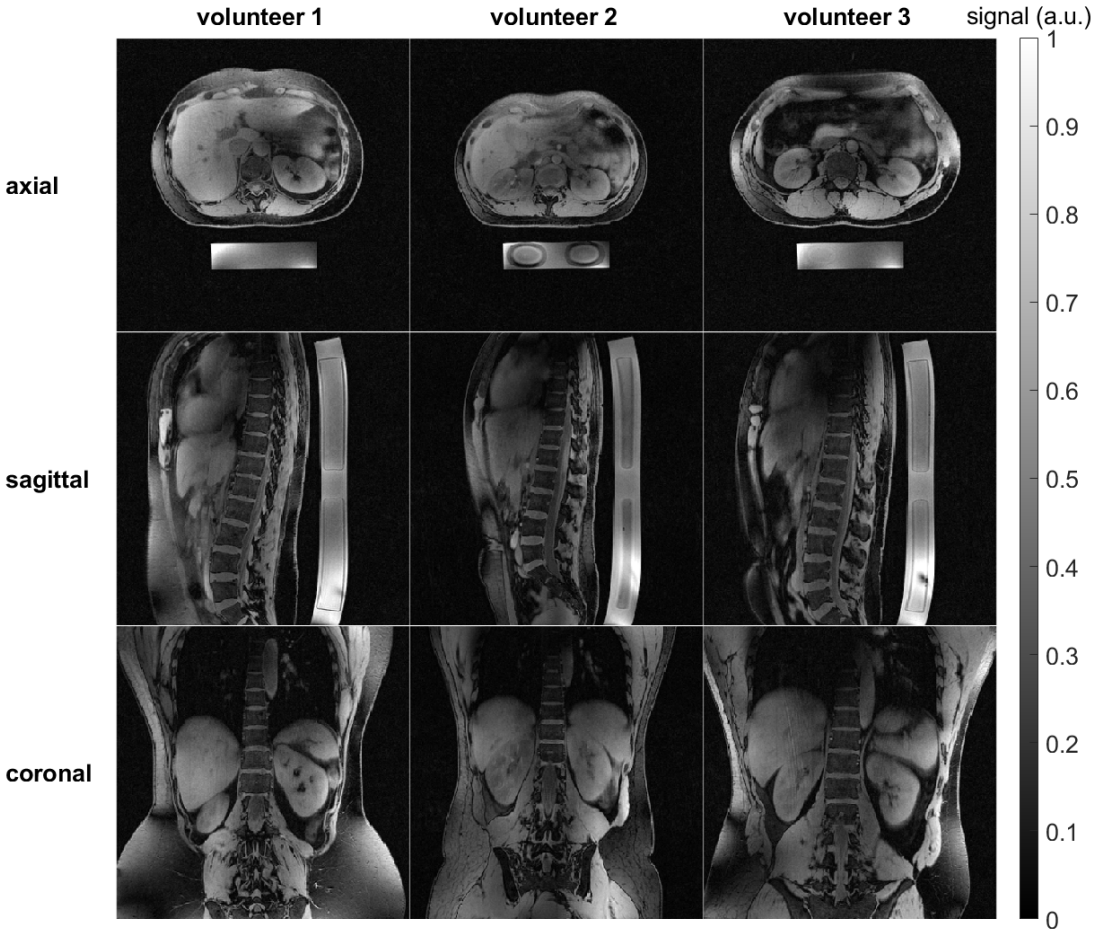

Figure 4.13: ^{1}H images before interpolation (acquired nominal resolution of $(1.25\,\mathrm{mm})^3$) for all three volunteers. These images were used for segmentation of different structures as described in section 3.3.6 to determine the aTSC in several abdominal structures in the human torso.

mated due to partial volume effects (see section 2.2.7). Figure 4.15 visualizes that the values for the determined aTSC are similar between the measured volunteers with the largest differences in the determined values for the gallbladder.

An overview over the mean for all volunteers and investigated VOIs can be found in Table 4.5 and Table 4.6 together with literature values for the investigated abdominal structures at 3 T and 7 T and by other measurement modalities.

Table 4.4: Summary of the obtained aTSC in the liver, kidneys, inferior vena cava (IVC), CSF, spleen and gallbladder of three healthy volunteers for the uncorrected data and data after the applied corrections.

volunteer no.	correction	liver (mM)	right kidney (mM)	left kidney (mM)	IVC (mM)	CSF (mM)	spleen (mM)	gallbladder (mM)
1	none	27± 8	54±14	42±11	57±11	62±15	21± 8	100± 22
1	T_1	26± 8	52±14	41±11	55±11	59±14	20± 8	97± 21
1	T_1 & B_1^+	31± 9	58±15	49±12	63±10	62±14	23± 9	117± 25
1	T_1, B_1^+ & B_1^-	38±11	66±16	64±15	78± 6	73±15	28±11	144± 33
2	none	26± 9	63±15	60±12	61±10	69±13	25±10	109± 24
2	T_1	25± 9	60±14	58±12	59±10	67±12	24± 9	105± 23
2	T_1 & B_1^+	29±10	63±15	64±13	66± 8	69±12	25±10	126± 27
2	T_1, B_1^+ & B_1^-	37±12	69±16	71±14	78± 7	77±12	31±11	145± 31
3	none	22± 8	48±12	46±12	46±13	52±14	22± 9	91± 25
3	T_1	21± 8	46±12	45±11	44±12	50±13	22± 9	87± 24
3	T_1 & B_1^+	27± 9	51±12	53±13	53±11	53±12	24±10	113± 32
3	T_1, B_1^+ & B_1^-	34±11	59±15	63±15	68± 7	67±13	30±12	127± 36

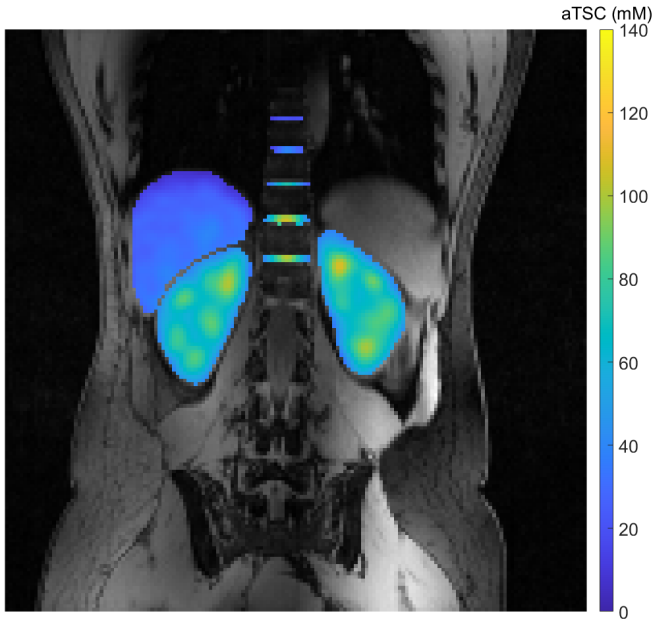

Figure 4.14: Exemplary visualization of the liver, kidney and a subset of the IVD masks for volunteer two. ^{1}H MR image are not displayed in the masked regions to allow a visual assessment of the aTSC for the depicted organs and IVDs.

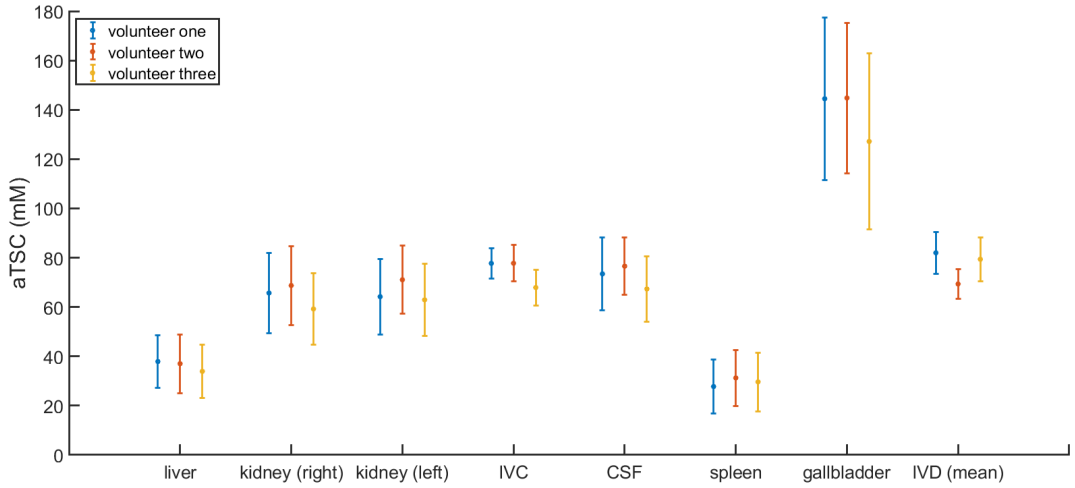

Figure 4.15: Plot illustrating the determined aTSC and standard deviation within the VOIs segmented in ^{1}H MR data after all corrections for the in Table 4.4 listed abdominal structures for the three measured volunteers. Values for CSF might be underestimated due to partial volume effects.

Table 4.5: Mean of the obtained aTSC in various organs and abdominal structures of three volunteers after corrections as well as corresponding literature values. The errors of the measured aTSC values are computed via Gaussian error propagation from the standard deviation in Table 4.4. Literature values are divided into in vivo measurements at 3 T and 7 T and concentration values determined from other modalities. Sources are provided as footnotes for readability of the table.

		aTSC literature values		
evaluated VOI	**measured aTSC (mM)**	**at 3 T (mM)**	**at 7 T (mM)**	**other modality (mM)**
liver	36 ± 6	41 ± 10 [1] 20.1 ± 0.9 [4]	27 ± 5 [2]	36.7 ± 3.4 [3]
kidney (right)	65 ± 9	71 ± 10 [1]		
kidney (left)	66 ± 8	79 ± 15 [1] 93 ± 9 [5]		
renal cortex		58 ± 17 [6] 72 ± 6 [5]	56 ± 2 [2] 32.2 ± 5.6 [7]	
renal medulla		99 ± 18 [6] 136 ± 7 [5]	81 ± 3 [2] 85.7 ± 16.0 [7]	
IVC	74 ± 4	83 ± 21 [1]		80 ± 8 [8] 81 ± 7 [8b]
CSF	72 ± 8	94 ± 18 [1] 135.2 ± 10.4 [10]		150.6 ± 10.9 [9]
spleen	30 ± 7	40 ± 9 [1]		31-34 [11]
gallbladder	139 ± 19	122 ± 42 [1]		122-164 [12] 141-164 [13]

[1] Birchall et al. (2024) [2] Lott, Behl, et al. (2019)
[3] Hooper et al. (1976) (flame photometry of rat livers) [4] James et al. (2015)
[5] Grist et al. (2020) (volunteers drank 500 mL water before imaging)
[6] Haneder, Kettnaker, et al. (2013) (no water or food intake restrictions)
[7] Haneder, Juras, et al. (2014) [8] Lott (2020) (ex vivo blood samples at 7 T)
[8b] Lott (2020) (laboratory blood values) [9] Harrington et al. (2010) (chromatography)
[10] Haneder, Konstandin, et al. (2011) (before water load, (135.5 ± 11.0) mM after water load) [11] Graham et al. (1982) (bovine spleen) [12] Furey (1966) [13] Liu et al. (2023)

Table 4.6: Mean and maximum of the obtained aTSC in the IVDs of three volunteers after corrections as well as corresponding literature values. The errors of the measured aTSC values are computed via Gaussian error propagation. Literature values are divided into in vivo measurements at 3 T and 7 T and concentration values determined from other modalities. Sources are provided as footnotes for readability of the table.

			aTSC literature values		
evaluated VOI	**measured aTSC (mM)**	**measured max. aTSC (mM)**	**at 3 T (mM)**	**max. value at 7 T (mM)**	**other modality (mM)**
Th8 / Th9	64 ± 10	94			
Th9 / Th10	65 ± 12	106	208 ± 10 [1]		
Th10 / Th11	70 ± 14	120	237 ± 12 [1]		
Th11 / Th12	73 ± 14	124	259 ± 16 [1]	197 [2]	
Th12 / L1	76 ± 15	131	297 ± 20 [1]	190 [2]	
L1 / L2	87 ± 19	160	305 ± 26 [1]	200 [2]	
L2 / L3	87 ± 19	164	342 ± 23 [1]	207 [2]	
L3 / L4	92 ± 22	192	313 ± 19 [1]	235 [2]	
L4 / L5			262 ± 14 [1]	218 [2]	
L5 / S1			216 ± 12 [1]		
mean	77 ± 5	137	327 ± 53 [3]		335 [4] 274.6 ± 18.9 [5]

[1] Çavuşoğlu et al. (2022) [2] Moon, Kim, et al. (2011) [3] Malzacher et al. (2016) (4 IVDs in the lumbar region) [4] Insko, Clayton, et al. (2002) (one volunteer at 4 T)
[5] Kamp et al. (2024) (ex vivo measurement of thompson grade 1 IVDs)

5 Discussion

The sensitivity of the tissue sodium concentration to changes in cell vitality and viability makes it a potential biomarker to access physiological changes in a variety of applications. Knowledge of the aTSC in healthy volunteers may help to differentiate normal levels of physiological change from changes due to diseases. The main goal of the presented work was thus the simultaneous quantification of the aTSC in several abdominal structures the human torso at 7 T in a large FOV.

In order to ensure an accurate quantitative aTSC measurement, the measured ^{23}Na signal must be corrected for the contrast mechanisms influencing signal intensity apart from the sodium concentration. To achieve this, a reference vial setup was designed and built and combined with several post-processing corrections to achieve repeatable quantification of the sodium concentration. The correction with a measured B_1^+ maps and setup-specific simulated B_1^- maps was validated in phantom measurements.

Two main studies were performed in vivo to demonstrate the feasibility of time-resolved quantitative ^{23}Na MRI to investigate renal aTSC changes during a water load event and the feasibility of combined large FOV quantitative ^{23}Na MRI and ^{1}H MRI in the same position. The aTSC was determined in several organs and abdominal structures in three healthy volunteers.

In the following chapter, the presented work is placed in the context of the current literature and the influences and limitations of the applied setup and corrections are discussed.

5.1 Reference Vial Setup

To quantify the aTSC, references of known concentration are required to assign quantitative values to the measured signal intensities. This can be achieved using

external references placed in the FOV of the ^{23}Na RF coil used or internal references within the body of known sodium concentration.

As part of this work, a fixed setup for external reference vials was designed and built with the primary aim of ensuring consistent placement within the ^{23}Na RF coil. This was achieved by positioning the vials below the subject, minimising the effect of respiratory movement on vial placement during in vivo measurements. In addition, the fixed position allows for automatic segmentation, reducing the influence of manual assessment and ensuring consistency with the simulated B_1^- maps used for correction. To allow the use of different ranges of sodium concentrations for the reference vials used, the set up was designed as a compartment containing the reference vials and a drawer housing acting as a laying surface. The four reference vials in the vial compartment are embedded in agarose gel to reduce susceptibility artefacts and improve B_0 shimming capabilities (Gerhalter, Gast, Marty, Uder, et al., 2020). The reference vials used were chosen to be relatively large to reduce the influence of partial volume effects (see section 2.2.7) on the parts used for concentration determination, as this could otherwise lead to overestimation of signal intensities. In order to minimise the height of the overall setup, oval reference vials were used, keeping the overall structure of the reference vial setup at a maximum height of 52 mm within the ^{23}Na RF coil.

The use of external reference vials for concentration determination, as presented here, has the disadvantage of reducing the space in the ^{23}Na RF coil, which could exclude some volunteers or patients from the measurement. In addition, the chosen placement of the vials at the edge of the FOV may lead to quantification errors, as B_0 and B_1 inhomogeneities are more pronounced. Appropriate correction methods can reduce these errors.

Internal references such as blood (Lott, Platt, et al., 2019) or cerebrospinal fluid (Wilferth, Mennecke, et al., 2022; Çavuşoğlu et al., 2022) are less susceptible to these errors due to their more central position within the RF coil. However, their limitations include a limited number of samples, partial volume effects, and potentially inaccurate relaxation times and ^{23}Na concentrations, as well as potential changes in aTSC due to disease (Meyer et al., 2019). For these reasons, external references were used for signal calibration. Alternatively, a separate scan with a phantom replicating the electrical properties of the human torso and an appropriate number of reference samples can be performed for signal calibration (Ouwerkerk, Weiss, et al., 2005). For this approach the coil loading needs to be correct as to be the same for both the phantom and in vivo measurements, which can be difficult to achieve in some cases.

Gast et al. (2023) note that evaporation of water during the preparation of agarose gels and variations in relaxation properties can introduce uncertainties in the determination of sodium concentration. As the agarose surrounding the reference vials is not used for the concentration determination in the presented setup, this is not of concern here. Nevertheless, reproduction of the agarose gel within the compartment is necessary to maintain good B_0 shimming capabilities as the agarose gel is exposed to the air when compartments are switched and thus deteriorates due to evaporation and mold growth (Hellerbach et al., 2013).

5.2 B_1^- Simulations

Performing EM simulations as described in section 3.3.4.2 is possible due to detailed knowledge of the custom-built ^{23}Na RF hardware (Platt, Umathum, et al., 2018). This allowed the simulation of setup-specific B_1^- maps to correct the ^{23}Na MR images.

As imaging of the entire upper abdomen, including organs such as the liver, kidney and spleen as well as parts of the lung was defined as an interesting area for quantitative ^{23}Na MR imaging, simulations of B_1^- maps were performed for a kidney placement centrally within the ^{23}Na RF coil. If other regions are of interest, such as parts of the thorax, the simulation model needs to be slightly modified by adjusting the positioning of the human voxel model within the ^{23}Na RF coil. An appropriate setup-specific B_0 map can then be simulated for the measurement and used to correct the quantitative ^{23}Na MRI.

So far, B_1^- simulations have been performed for one anatomic voxel model per gender, scaled isometrically to match the subject's anatomy where necessary. As can be seen for example in Figure 4.4 and 4.5, the shape and placement of the kidneys within the torso can still vary between volunteers. The same applies to other structures. As a result, the simulated B_1^- maps may fit some volunteers better than others. To investigate this influence, simulations with a wider range of anatomical voxel models could be performed and evaluated for their influence on the determined aTSC.

5.3 Phantom Measurements

The phantom measurements allowed to validate the post-processing workflow later used for the in vivo studies, showing a very good agreement between the measured values and the ground truth in quantitative ^{23}Na MR images after the applied corrections (see section 2.3). This section also provides an overview of the limitations of the phantom used.

In general, phantoms cannot reproduce all MRI-relevant properties, and for the phantom used here, the focus was on quantification of the sodium concentration. As ^{1}H images were not initially possible, the phantom was filled with a NaCl solution, which has unfavourable dielectric properties for ^{1}H MRI. As a result, the phantom was not perfectly suited for the ^{1}H measurements that were later included. In addition, shims were used for ^{1}H imaging that were not optimised for this phantom. This resulted in residual signal variations in the ^{1}H MR images due to transmit field inhomogeneities. In the future, specific shims for this phantom could be calculated and applied to potentially further reduce signal dropouts in the images. As these images were only used to assess the post-processing workflow in the present work, these signal dropouts did not interfere with this goal.

Designing a phantom for quantitative ^{23}Na measurements that mimics realistic tissue properties is difficult because the dielectric properties of tissue and phantom materials are frequency dependent and therefore different for ^{1}H and ^{23}Na at the same field strength. Therefore, phantom measurements were used to assess the homogeneity that could be achieved for ^{23}Na MRI within the FOV, but did not attempt to mimic relaxation parameters for ^{23}Na or ^{1}H MRI. Instead, ease of refilling was chosen, as a polyvinylpyrrolidone-filled phantom would probably not have been able to be emptied again for this phantom. A newer design of a phantom for quantitative ^{23}Na MRI with the setup presented here could be constructed to allow a large opening to allow refilling with more viscous materials.

Despite these limitations, the phantom measurement showed that the B_1^+ and B_1^- corrections could significantly improve the quantitative accuracy of the sodium concentration maps. The T_1 correction applied could not be validated in the phantom measurements because both the phantom and reference vials were filled with a NaCl solution. Homogeneity after the applied corrections was high throughout the whole phantom with a CV of at least 0.14. As the higher values in the central region of the uncorrected phantom concentration maps are partially compensated for by the lower apparent concentrations in the peripheral regions and the evaluated VOIs for in vivo segmentations are small compared to the whole phantom, two

smaller VOIs were additionally evaluated. Evaluation of the peripheral and central cuboidal VOIs showed the success of the corrections for different placements within the FOV. This was particularly evident for a centrally placed VOI which showed a strong overestimation without corrections with a difference of 22 mM from the ground truth of 35 mM.

After the applied corrections, the aSC within all evaluated VOIs was within one standard deviation of the ground truth value of 35 mM. The CV within the peripheral and central cuboidal VOIs was less than 6 % and 4 % after the B_1^+ and B_1^- corrections, respectively. The mean of the three measurements taken within the whole phantom VOI after the applied corrections was 35 ± 8. For the two smaller VOIs evaluated in the peripheral and central parts of the phantom, the mean aSC for the three measurements was 34 ± 4 and 35 ± 2. The variations between the three measurements were small with a standard deviation of 0.2 for the whole phantom VOI and 0.3 and 0.06 for the peripheral and central cuboidal VOI respectively.

The alignment of the quantitative ^{23}Na images and ^{1}H images was demonstrated, allowing to forgo image registration for subsequent in vivo measurements. This is advantageous as there are potential changes within the structures of interest when acquiring two different scans. Changes may be due to a different posture within a different coil and/or physiological differences between the two scans due to e.g. rectal and bladder filling, digestive processes, etc. This can make image registration of the ^{1}H and ^{23}Na MR images difficult, especially in a large FOV.

5.4 In Vivo Measurements

Two in vivo studies were presented as part of this work, demonstrating the feasibility of time-resolved quantitative ^{23}Na MRI to investigate renal changes during a water load event (see section 4.3.1) and the feasibility of combined ^{1}H and quantitative ^{23}Na MRI in a large FOV in the human torso (see section 4.3.2). This section discusses the advantages and disadvantages of the presented in vivo studies and provides an overview of the differences from previous studies while comparing the aTSC values obtained.

5.4.1 Image Reconstruction

All of the acquired data, except the localizer images, had to be reconstructed offline. This has the disadvantage that no part of the measurement can be repeated in the same session, as problems such as movement only become apparent after the measurement has been completed. Due to the large number of coil elements in the ^{1}H RF coil, the raw data requires a lot of storage space and currently takes about 2 h to reconstruct using the settings from Table 4.2.

5.4.2 Segmentation

Segmentation in the context of this work was performed using MITK as described in section 3.3.6. This section discusses the potential influence of image segmentation on the aTSC determined in the presented work and discusses the limitations of the chosen segmentation approach.

When segmenting in MITK with the MedSAM tool, it is advantageous to segment everything in the same slice without re-initializing the tool. This allows the time to the first prediction of the region of interest to be reduced, which helps to reduce the segmentation time slightly. The tool used performs segmentation in 2D and has been combined with 2D interpolation. This may result in peripheral parts (in the direction of segmentation) of the segmented organ having insufficient contrast to be segmented automatically. As a result, either manual segmentation is required for the particular slice or the number of slices included in the segmented direction is reduced. For organs with inhomogeneous aTSC distribution, this can lead to differences in the measured aTSC. For example, in the kidney, peripheral areas are part of the cortex, which has a lower aTSC compared to the medulla, which is more centrally located within the kidney. Masks containing less cortical areas may therefore overestimate the aTSC of the whole kidney. Delineation of the cortical area is very challenging because ^{23}Na MRI does not provide the necessary anatomical information and was acquired with low spatial resolution compared to ^{1}H MRI, which is usually used for segmentation. As the kidneys have a higher aTSC than the surrounding structures, differentiation between lower aTSC due to cortical tissue versus PVE cannot be confidently made in ^{23}Na-only MRI.

For the reasons described, the mask size differed for the different subsets of data throughout the water load experiment in section 4.3.1. This had little effect on the evaluation of the data with the same mask for volunteer two, where the movement

of the kidneys was less pronounced compared to volunteer one. As the movement of the left kidney of volunteer one was very pronounced with up to 2.1 cm caudal displacement, evaluation with individual masks for each subset is crucial for accurate evaluation of aTSC throughout the measurement. However, some influence of the mask size cannot be completely excluded.

The MedSAM tool works particularly well for structures with varying contrast to the surrounding tissue, such as the kidneys. Larger structures, such as the liver, required more manual adjustments. However, segmentation was faster than a fully manual approach when the entire organ or abdominal structure volume had to be segmented.

When segmenting multiple organs in the same group in MITK, their segmentation cannot overlap, which can be an advantage when segmenting structures that are close together and might otherwise be misclassified. This can happen because the tool used is a 2D tool, and contrast changes due to residual transmit field inhomogeneities in adjacent structures of similar contrast can make differentiation difficult for automatic calculation. For this reason, segmentation of, for example, the gallbladder and IVC prior to segmentation of the liver has been shown to be advantageous.

The segmentation of the data for the presented research was not performed by a radiologist, which might influence the resulting masks and thus the aTSC values generated with them. In addition, evaluation by a second observer could identify inter-observer variations in aTSC due to different segmentations.

5.4.3 Renal ^{23}Na MRI Before, During and After a Water Load

In this work a sliding window reconstruction of quantitative ^{23}Na MR images is applied in two healthy volunteers to investigate the renal changes in the aTSC not only after water deprivation and after the water load as for example performed by Haneder, Konstandin, et al. (2011), but also during and immediately after water intake.

It could be shown that time-resolved sodium MRI is feasible to investigate changes during a water load event. Acute water loading, as performed in this study, increases sodium excretion by reducing sodium reabsorption in the proximal segment of the nephron (Burnier et al., 2000). As the nephrons are located within the renal medulla, reduced sodium reabsorption leads to a decrease in the observed aTSC.

For volunteer one, the ratio of medulla to cortex aTSC was found to be 1.71 before the water load. Shortly after the water load the ratio increased to 2.08 before decreasing to 1.43 later during the measurement. The aTSC in the cortex was 52 mM, 58 mM and 56 mM before, shortly after and long after water loading. For the medulla, values of 99 mM, 120 mM and 82 mM were determined. Volunteer two on the other hand showed little changes in aTSC throughout the measurement. Visually, an overall lower aTSC was observed in the medulla of volunteer two. Water loading resulted in a slight increase in medullary aTSC from 74 mM before water loading to 90 mM shortly after water loading. At the end of the measurement, the aTSC in the medulla was 80 mM. The medulla to cortex ratios for volunteer two were 1.56, 1.89 and 1.69 before, shortly after the water load and at the end of the measurement. As no ^{1}H MR images were acquired for segmentation of the cortex and medulla region, the determination of the cortex edge in particular influences this ratio.

Comparison with literature values is hampered by the fact that reported values are not consistent between studies due to differences in post-processing protocols. Below, the results of the data presented are placed in the context of previous work and the main differences between the studies are highlighted.

At 3 T, Maril, Rosen, et al. (2006) measured the first in vivo medulla to cortex ratio of 2.4 ± 0.1 in six healthy volunteers. No concentration quantification was performed but SNR means for cortex, medulla and whole kidney regions of interest, segmented in ^{1}H images, were reported as 12.9 ± 1.2, 34.1 ± 3.1 and 20.8 ± 2.2 after water deprivation of 12 h. A ratio of 4.75:1 and 3.78:1 was found for the mean intensity between the tip of the medulla and the edge of the cortex with and without water deprivation. This represents an increase in the cortico-medullary gradient of 25 % after water deprivation of 12 h. In the context of this work, volunteers showed a reduced medulla to cortex ratio. As no ^{1}H MR data were acquired for this study, the determination of the cortical edge is challenging and may partially account for this difference. The FOV of the surface coil used in Maril, Rosen, et al. (2006) was only $(38 \times 38 \times 24)\,\mathrm{cm}^3$ and the coil sensitivity was corrected with a phantom measurement.

Haneder, Kettnaker, et al. (2013) found a mean increase from the renal cortex to the medulla of (58 ± 17) mM to (99 ± 18) mM for the 50 healthy volunteers studied at 3 T. There were no restrictions on water or food intake. For this study, the RF coils were changed for ^{1}H MR images and a falcon tube (0.6 % NaCl and 2 % agarose) was used for quantification of ^{23}Na concentration. The values obtained for the cortex of volunteer one fit very well with these literature values. Apart

from the increased aTSC shortly after the water load, a configuration not included in the Haneder, Kettnaker, et al. (2013) study, the values for the medulla also fit within the reported range. In volunteer two, aTSCs were more than one standard deviation lower in both cortex and medulla in the water-deprived state. As the inter-individual range of reported sodium concentrations was between 27 mM to 126 mM in the cortex and between 63 mM to 187 mM in the medulla, volunteer two may just be at the lower end of the aTSC in the kidney overall.

A multi-site study determined the aTSC at 3 T in twelve healthy volunteers split between two sites (Grist et al., 2020). They reported very similar sodium concentrations between both sites with an average of (136 ± 7) mM, (72 ± 6) mM and (93 ± 9) mM for the medulla, cortex and whole kidney for all volunteers. They performed B_1^+ corrections using the double angle method, but no B_1^- correction was applied. As each volunteer was required to drink 500 mL of water before imaging without a specification on the start time of the ^{23}Na image acquisition after the ingestion, the results are difficult to compare with the other literature given the potential drastic changes in aTSC in the renal medulla after a water load observed for volunteer one in the here presented work. Nevertheless, the reported values are generally higher than the aTSC values found here.

Recently, Akbari et al. (2022) reported a reduction in mean medulla-to-cortex ratios in fasted healthy volunteers undergoing water loading from 1.55 ± 0.11 before water loading to 1.31 ± 0.09 after water loading. The range of reported ratios before the water load was 1.35 to 1.70. Volunteer one is at the upper end, while volunteer two shows a ratio around their reported mean. The ten healthy volunteers ingested 15 mL of water per kilogram of body weight within 15 min. For the volunteers measured here, this would correspond to 1275 mL and 975 mL for volunteer one and two respectively. During the experiment, volunteers one and two drank 629 mL and 1044 mL respectively. While volunteer one drank about half of the amount described in Akbari et al. (2022), the measured value of 1.43 for the medulla to cortex ratio also showed a decrease long after the water load. As the first measurement point after water loading in Akbari et al. (2022) is 1 h after the water load, it makes sense that the measured value here is slightly elevated in comparison. Volunteer two consumed a similar amount of water to that used in the study, but at the end of this measurement the medulla to cortex ratio did not show the same decrease as in volunteer one. This may be due to a later decrease that was not captured by the measurement performed here.

At 7 T, after abstaining from food and drink for one hour before the scan, an increase in SNR from the cortex to the medulla from 32.2 ± 5.6 to 85.7 ± 16.0 was

found by Haneder, Juras, et al. (2014). The maximum difference in SNR from the cortical value is observed at 16 mm for most of their volunteers, suggesting that the cortical value chosen here may be overestimated, as it was only 12 mm from the maximum within the medulla for both volunteers. The SNR in the medulla reported in this study is a factor of 2.66 higher than the reported SNR in the cortex, which was not found in the presented results. Depending on the physiological state, the aTSC in the medulla of volunteers one and two was a factor of 1.43 to 2.08 and 1.56 to 1.89 higher than their aTSC in the cortex, respectively. These values fit better with the reported aTSC difference between cortex and medulla of a factor of 1.7 at 3 T without dietary restriction in the Haneder, Kettnaker, et al. (2013) study.

For volunteer one, there was pronounced kidney movement of up to 2.1 cm displacement after the water load in the left kidney, most likely due to the stomach filling and the placement of the stomach relative to the left kidney. For this reason, the volumes of interest in each kidney were segmented individually for each subset evaluated. Adjusting the VOIs to the subsets has the disadvantage of increasing operator influence on VOI placement when performing ^{23}Na only measurements. Even with the semi-automated segmentation performed with the MedSAM tool in MITK (see section 3.3.6), the created masks showed volume changes between 27 mL and 49 mL. The smallest change was observed in the right kidney of volunteer one and the largest in the left kidney of volunteer two. As the masks for the kidneys were segmented for each subset, some variation in aTSC can be expected to be due to a difference in the masks used. However, evaluation of the aTSC for volunteer two using the same mask for all subsets did not change these findings. A combination with ^{1}H MRI in the same positioning of the volunteer or patient could improve registration or, in the case of simultaneous multi-nuclei acquisition, allow an overlay without registration. This type of interleaved acquisition acquires both nuclei within a single T_{R} by alternating excitation pulses and signal readouts, and has been shown for example by Wilferth, Müller, et al. (2022) and Bruin et al. (2015). The near-simultaneous data acquisition minimizes registration errors due to motion that can occur in sequentially acquired scans. This type of interleaved acquisition is particularly attractive for this application, as the water load event can cause the kidneys to move throughout the measurement. However, this is currently not easily achievable with our setup due to hardware and software limitations.

B_1^+ maps were acquired only at the beginning of the measurements. If the experiment were repeated, a shorter B_1^+ mapping sequence, such as that used for the in vivo measurements combined with ^{1}H MRI (see section 4.3.2), could be acquired

at multiple points to investigate the variation due to organ motion and subsequent aTSC changes.

Evaluation of a larger number of volunteers could help to understand normal levels of change in aTSC before, during and after a water load event. In addition to abstaining from food and drink for a period of time, other influences may be relevant such as general diet, fitness or hormonal changes during the menstrual cycle in female volunteers as in the presented research. Therefore more data is needed to investigate the response to a water load in the human kidney, ideally in combination with ^{1}H MRI in the same position.

5.4.4 ^{23}Na and ^{1}H MRI in a Large Field-of-View

The results presented in section 4.3.2 demonstrate the feasibility of full body width quantitative ^{23}Na MRI combined with ^{1}H MRI in the human torso with a large z-coverage at reasonable scan times. This section provides an overview of previous studies on quantitative or qualitative ^{23}Na MRI in the torso at 3 T and 7 T and individual differences to the presented setup and post-processing workflow.

The high field strength of 7 T is advantageous for ^{23}Na MRI to generate adequate SNR in an acceptable measurement time. For ^{1}H MRI, the high operating frequency at 7 T leads to signal dropouts due to the inhomogeneity of the transmit field. In this work, pTx (see section 2.4.1) and TIAMO (see section 2.4.2) were used to improve the homogeneity.

As no ^{1}H B_1^+ maps were acquired in this study, a TIAMO shim optimized in a tissue-simulating phantom was used to acquire ^{1}H MR data. This resulted in residual signal dropouts in the ^{1}H MR images, which were particularly pronounced in the phantom due to the unfavourable dielectric properties of the NaCl solution in the phantom (see Figure 4.3). Remaining signal dropouts could potentially be located in the region of interest of the in vivo measurements, making image segmentation for certain structures difficult or impossible. In the future, phantom- or subject-specific optimisation of the TIAMO shims could further minimize 7 T-related ^{1}H signal dropouts. Furthermore, the ^{1}H images are not intensity corrected. However, the ^{1}H MR image quality acquired for the presented volunteers is sufficient for segmentation of various central abdominal structures (e.g. liver, kidney, IVC, cerebrospinal fluid, spleen, gallbladder and IVDs), so that improved ^{1}H MR image quality is not necessary here.

The presented setup is unique in the way it enables full body width quantitative ^{23}Na MRI combined with ^{1}H MRI in the human torso. An overview of previous studies and how they differ from the present approach is discussed below. Wetterling et al. (2012) investigated ^{23}Na MRI in the human torso qualitatively and without ^{1}H imaging. At 3 T, the integrated ^{1}H body coil was combined with a ^{23}Na surface coil to investigate the cortico-medullary signal gradient in the kidneys qualitatively (Akbari et al., 2022; Lemoine et al., 2024; Maril, Rosen, et al., 2006), and quantitatively (Haneder, Konstandin, et al., 2011) or the prostate quantitatively (Hausmann et al., 2012). Some groups performed quantitative ^{23}Na MRI and registered ^{1}H MR data that was acquired with a different coil setup (Haneder, Kettnaker, et al., 2013) or at a different scanner (Lott, Platt, et al., 2019).

As the integrated ^{1}H 32-channel pTx body coil and the local ^{23}Na body coil can be used in one examination in the presented setup, a simple overlay of the acquired 3D datasets of the ^{1}H and the quantitative ^{23}Na data eliminates the need for a registration. Eliminating the need for a registration to acquire the ^{1}H images increases the accuracy of the anatomical information that can be obtained. In two examinations, e.g. with two different local RF coils, a change in subject positioning and physiological state between the ^{1}H and ^{23}Na measurements could lead to inaccurate image registration and aTSC determination (Gast et al., 2023).

Dual-nuclei coils share this advantage but usually have a small FOV (Moon, Furlan, et al., 2014; Graessl et al., 2015; Haneder, Budjan, et al., 2015; Boehmert et al., 2019; Ianniello et al., 2019; Ruck et al., 2024; Schmidt et al., 2022) and can therefore only examine a single organ at a time, whereas the setup presented here allows simultaneous quantification in several structures at the same time. In other studies, the acquired FOV in z-direction was larger, but the acquisition time was kept short by acquiring only 3 slices for ^{23}Na, limiting the acquisition to the IVDs only (Çavuşoğlu et al., 2022). While Wetterling et al. (2012) performed whole body ^{23}Na MRI, they did not quantify the aTSC nor include ^{1}H MRI.

Due to the large distance of the ^{1}H RF coil from the investigated subject in the presented setup, the receive sensitivity is low compared to local RF coils (Grimm et al., 2024). To improve the SNR, additional ^{1}H receive coils would have to be adapted to the available space in the bore where the ^{23}Na RF coil is already located. For the structures studied in this research, the SNR was sufficient for image segmentation. Furthermore, the placement of the ^{1}H RF coil behind the scanner bore has the advantage that the coil for the lower SNR nucleus is placed closer to the subject, whereas other setups for combined ^{1}H and ^{23}Na MRI have the opposite order (Ruck et al., 2024). This leaves enough room to place external

reference vials within a fixed position of the ^{23}Na RF coil in the presented setup, even when combined with ^{1}H MRI. As discussed in section 5.1, the reference vials for the presented setup were chosen to be large to reduce the influence of PVE. Previous studies have mostly used small external reference vials for correction due to space limitations (Haneder, Kettnaker, et al., 2013; Moon, Furlan, et al., 2014).

In the post-processing workflow presented, B_1^+ is measured, while B_1^- is simulated for ^{23}Na MR image corrections. This is an advantage over studies that only measure B_1^+ and assume $B_1^- = B_1^+$ (Birchall et al., 2024; Vaeggemose et al., 2023) where this assumption may not hold true (Vaidya et al., 2016) or measure B_1^+ in a phantom for B_1^+ and B_1^- correction (Malzacher et al., 2016; Moon, Furlan, et al., 2014).

The utilized free-breathing acquisition was performed with sequences less prone to artifacts due to respiratory motion for both ^{23}Na and ^{1}H measurements, but was not respiratory sorted, so respiratory motion blurs the reconstructed images. Retrospective respiratory sorting of image data, as described for example in Platt, Umathum, et al. (2018), could be performed in the future to investigate the influence of respiratory motion on the segmentation and accuracy of the determined aTSC. The implementation of XD-GRASP (Feng et al., 2016), which uses compressed sensing (Lustig et al., 2007) on data sorted into multiple motion states may not only account for motion in the ^{23}Na MR data but could also help to reduce scan time.

Another way to reduce the measurement time and thus some of the motion (e.g. due to digestion or muscle relaxation) would be to interleave the ^{1}H and ^{23}Na data acquisition (Lopez Kolkovsky et al., 2022) using the long T_R of sodium for the ^{1}H acquisition as done for example in Wilferth, Müller, et al. (2022) and Bruin et al. (2015). Due to hardware and software limitations, this is currently not easily achievable with our setup. A further reduction in the overall scan time opens up the possibility of measuring a wider range of subjects and patients.

The focus of this work was to collect data that would allow an accurate estimation of the aTSC with the presented setup (e.g. by applying long T_R). In the future, it could be investigated how reducing the scan time for the ^{23}Na MR image affects the determined aTSC. The effect of undersampling the ^{1}H MR images on the segmentation and thus the aTSC could also be investigated to potentially further reduce the measurement time.

Knowledge of the aTSC in a large FOV could, for example, help to monitor the progress of chemotherapy in patients with widespread metastases (Wetterling et al., 2012). Another possible application is the study of the cardiorenal syndrome (Ronco et al., 2008). Here, simultaneous acquisition of the heart and kidneys could save scan time and improve understanding of the interdependence of the two organs. In addition, a large FOV allows previously unstudied regions of the body, such as the pancreas and stomach, to be examined without the need for an additional scan.

The cited measurement for the liver aTSC at 7 T (Lott, Behl, et al., 2019) did neither correct for relaxation effects in the reference vials used, nor B_1^- effects, and had no ^{1}H data for segmentation. Their measured range for the aTSC in the liver was 22 mM to 31 mM for three volunteers, which is similar to the range measured here without B_1^- correction (see Table 4.4). At 3 T, James et al. (2015) reported values of (20.1±0.9) mM for two healthy volunteers. They used a short T_R of 12 ms and performed B_1 corrections with a homogeneous phantom for a multi-channel surface coil. The here presented aTSC for the liver are higher than those reported in this study. In a recent study at 3 T, Birchall et al. (2024) measured the aTSC in the liver for 19 volunteers. As an overlay of the acquired images was not possible in their case due to gradient non-linearities, B_1^+ and B_1^- correction factors were determined after segmentation in the flip angle maps and registration onto the quantitative images. Their reported values of (41 ± 10) mM are in good agreement with the liver aTSC measured in this research. Measurements in rats reported liver sodium concentrations of (36.7 ± 3.4) mM for a study population of ten healthy rats (Hooper et al., 1976).

The values measured in the whole kidney are in good agreement with those recently measured at 3 T (Birchall et al., 2024). As the volunteers drank water before the evaluation in Grist et al. (2020), the higher values reported in their study cannot be adequately compared, as already discussed in section 5.4.3. Reported values for the aTSC in the cortex and medulla span a wide range and are reported for different physiological states. Given the number of measured volunteers in Haneder, Kettnaker, et al. (2013), this study may best capture the variability in healthy subjects.

The value in the IVC can be compared with the values measured in ex vivo blood samples at 7 T and their corresponding laboratory values (Lott, 2020). They reported a concentration of (81 ± 7) mM and (80 ± 8) mM for the ^{23}Na-MRI and laboratory measurements, respectively. The aTSC measured here of (74 ± 4) mM is also in a similar range to the reported value of (83 ± 21) mM at 3 T (Birchall

et al., 2024).

Data on the aTSC in the human spleen are limited. At 3 T, Birchall et al. (2024) reported (40±9) mM, which is higher than the in the context of this work measured (30 ± 7) mM. However, a study analyzing bovine spleen tissue reported sodium content ranging from 720.7 ppm to 781.5 ppm (Graham et al., 1982) for the whole spleen. Given the molar mass of ^{23}Na of 22.99 g mol^{-1}, this results in a range of 31 mM to 34 mM for the aTSC of the bovine spleen, which is in good agreement with the mean determined here for three volunteers.

For the gallbladder, the measured mean value of (139 ± 19) mM is slightly higher than that reported by Birchall et al. (2024), but still within one standard deviation. Furey (1966) and Liu et al. (2023) state that bile has sodium concentrations similar to plasma and report values of 145 mM with a range of 122 mM to 164 mM and a range of 141 mM to 165 mM, respectively. In both cases, the aTSC for the gallbladder determined in this research is in good agreement.

For CSF and IVD, the aTSC values obtained are lower than those reported in the literature. Both compartments are small compared to the examined organs and for some of the IVDs the masks were only two to three voxel thick in the uninterpolated ^{1}H images (see Figure 4.14 for a visualization of the IVD masks in one volunteer after interpolation). Therefore, PVE may have a greater effect in the CSF and IVD VOIs, leading to an underestimation of aTSC. The generated masks are also over the entire IVDs, whereas some aTSC values are reported for the inner nucleus or a maximum value within the VOI. Choosing only the maximum value within the VOI can reduce PVE but this approach is more susceptible to potential outliers, especially in more peripheral regions where B_1 corrections may introduce artifacts. As the vial concentrations for the in vivo measurements were chosen to fit the expected range of concentrations investigated in the abdominal organs, the fit obtained could deviate more in the regions of higher concentrations, which could increase the uncertainty of the determined concentration in the IVDs. In future investigations, more measurements could be performed with different vial concentrations (e.g. up to 300 mM) to investigate the potential improved accuracy of the determined aTSC in the IVDs.

Despite the potential underestimation of the values obtained for the IVDs and CSF, the advantage of the proposed setup, which allows the simultaneous determination of aTSC in a large abdominal region, is demonstrated. The comparison of aTSC values determined individually for different organs can improve the accuracy of the post-processing workflow. This comparison is not possible if the aTSC is only

known in one structure. An example of this is concentration determination, where the known concentration of CSF is used to determine the aTSC in the IVDs. In this case, the resulting aTSC values in the IVDs could potentially be within the expected range, while the concentration map would estimate unrealistic values for e.g. the liver. This is usually not investigated, even in cases where the FOV would allow comparison with another organ or abdominal structure. The presented setup can thus be used to investigate the influence of future additional correction methods on a range of aTSCs. The acquired ^{1}H images could, for example, be used for a future partial volume correction as previously described by Niesporek et al. (2015). This approach aims to increase the accuracy of the determined aTSC in small regions adjacent to regions with a very different aTSC, which are currently under- or overestimated due to the large voxel sizes.

Comparison with literature values is complicated not only by different physiological states, but also by often unknown segmentation volumes. For the liver, the placement of the IVC must be taken into account, otherwise the higher aTSC will lead to an overestimation of the aTSC for the kidney. For the values reported here, smaller blood vessels are still included in the mask, as their influence is smaller due to their smaller size, as shown for one subject (see section 4.3.2).

Apart from the spleen, aTSC were lower in the male volunteer than in the two female volunteers. As the male volunteer was also younger, several factors could have a potential influence and more volunteers should be studied. Repeatability studies are also needed to investigate intra- and inter-volunteer variability.

As the ^{1}H images are currently acquired after the ^{23}Na images, slight changes due to movement during the scan and physiological changes such as bladder and rectal filling may still lead to differences in organ placement in the ^{1}H and ^{23}Na images. To reduce these effects, all volunteers were measured after fasting for at least 9 h. To further minimize this effect and reduce the measurement time, ^{1}H and ^{23}Na MRI could be performed in an interleaved fashion in a next step. Currently, a manual switch has to be made to switch from ^{23}Na to ^{1}H MRI, as the safety monitoring for ^{1}H MRI is custom-built, while the scanner-internal safety monitoring is used for ^{23}Na MRI. It is therefore currently not possible to interleave the ^{1}H and ^{23}Na pulse sequences.

Gradient non-linearities over the large FOV used for the measurements in this work contribute to a distortion of the ^{1}H images at the periphery, as can be seen in Figure 4.13. The usual corrections for this have been disabled to allow the superposition of ^{1}H and ^{23}Na data. However, it should be noted that this effect

reduces the accuracy of the overlay in peripheral regions. As the gradient nonlinearities are small for the gradient used here, this effect is not as pronounced as in other systems. Birchall et al. (2024), who determined aTSC for several organs at 3 T using a large FOV, commented on this. In their case, it was not possible to overlay the images, and B_1^+ and B_1^- correction factors were determined after segmentation in the flip angle maps, in addition to segmentation in the quantitative images.

5.5 Further Potential Influences

Lott, Platt, et al. (2019) found a minimal effect of B_0 correction on myocardial aTSC for the ^{23}Na RF coil used in this research, using blood as an internal reference. Gerhalter, Gast, Marty, Uder, et al. (2020) showed a more significant effect of B_0 correction in the leg muscle, possibly due to the use of external reference vials with relatively high off-resonance values. Although B_0 field inhomogeneity for sodium imaging has a relatively small frequency range (Gerhalter, Gast, Marty, Uder, et al., 2020), implementing it as an additional correction could further improve quantification accuracy. However, the homogeneity achieved within the phantom and reference vials was high and quantification worked well for the whole phantom as well as for two smaller volumes placed in the peripheral and central parts of the phantom (see section 4.2.1).

In the context of the research presented here, magnetization was assumed to be stationary, whereas this is not the case, at least in regions such as the inferior vena cava. Non-stationary magnetization accumulates a different phase in different parts of the FOV due to B_0 inhomogeneities. The accumulated phase contributions of the magnetisation arising from velocity or acceleration will be misinterpreted as arising from the spatial coordinate. This can lead to non-stationary magnetisation being imaged at the wrong location.

6 Summary and Conclusion

A fixed reference vial setup was developed to allow automatic determination of ^{23}Na concentration maps using the presented measurement routine and post-processing workflow. Phantom measurements with the presented reference vial setup and the performed T_1, measured B_1^+ and setup-specific simulated B_1^- corrections confirmed the ground truth ^{23}Na concentration value of 35 mM in both large and smaller volumes placed in the peripheral and central regions of the phantom with a maximum difference of 3.4 % for the VOI in the peripheral region. A maximum standard deviation of 0.3 mM between three measurements was observed in the peripheral region of the VOI.

Time-resolved quantitative ^{23}Na MRI during a water load experiment was investigated in two healthy volunteers. The ratios of medulla to cortex aTSC for volunteers one and two are 1.71, 2.08 and 1.43 and 1.56, 1.89 and 1.69 before, shortly after and long after water loading respectively. For both volunteers, the reported change is for a distance of 12 mm between cortex and medulla.

The feasibility of combined ^{1}H and quantitative ^{23}Na MR imaging at 7 T in a large FOV in the human torso under free breathing was demonstrated in three healthy volunteers. Reconstruction of ^{1}H and ^{23}Na data in the same position allows for a simple overlay of the two 3D datasets and thus segmentation in the anatomical ^{1}H images. The large FOV of $(400 \times 400 \times 400)\,\mathrm{mm}^3$ is advantageous when multiple structures are of interest. With an acquisition time of approximately 47 min, aTSC was measured in the liver, kidneys, IVC, CSF, spleen, gallbladder and IVDs of three volunteers. The mean aTSC determined for the three volunteers in the liver was (36 ± 6) mM. In the left and right kidney, the mean values were (65 ± 9) mM and (66 ± 8) mM, respectively. In the inferior vena cava, an aTSC of (74 ± 4) mM was measured. For the spleen, to the best of my knowledge, the first aTSC values at 7 T were reported as (30 ± 7) mM. In the gallbladder, the mean aTSC for the three volunteers was measured as (139 ± 19) mM. For the IVDs, higher values were found in the lumbar region with an average over the IVDs from Th8/Th9 to L3/L4 of (78 ± 5) mM for all volunteers. Good agreement with literature values was found for the determined mean aTSC for the liver, kidneys, IVC, spleen and gallbladder.

Values for CSF and IVDs are lower than literature values, which may be due to partial volume effects.

The presented workflow is a first step towards establishing a baseline of healthy aTSCs in various abdominal structures simultaneously. In the future, this could serve as a non-invasive biomarker to study a multi-organ interactions and investigate changes due to physiological processes in multiple regions of the body simultaneously.

Next steps could be towards decreasing the measurement time to allow a wider range of volunteers and patients to be measured. Possible possible methods include interleaving the ^{1}H and ^{23}Na acquisitions or the implementation of more advanced reconstruction algorithms that allow the measurement time to be reduced without loss of aTSC accuracy. A partial volume correction could be implemented to reduce the current underestimation of the aTSC in small structures such as the IVDs and CSF.

7 Appendix

Appendix of Section 4.2.2

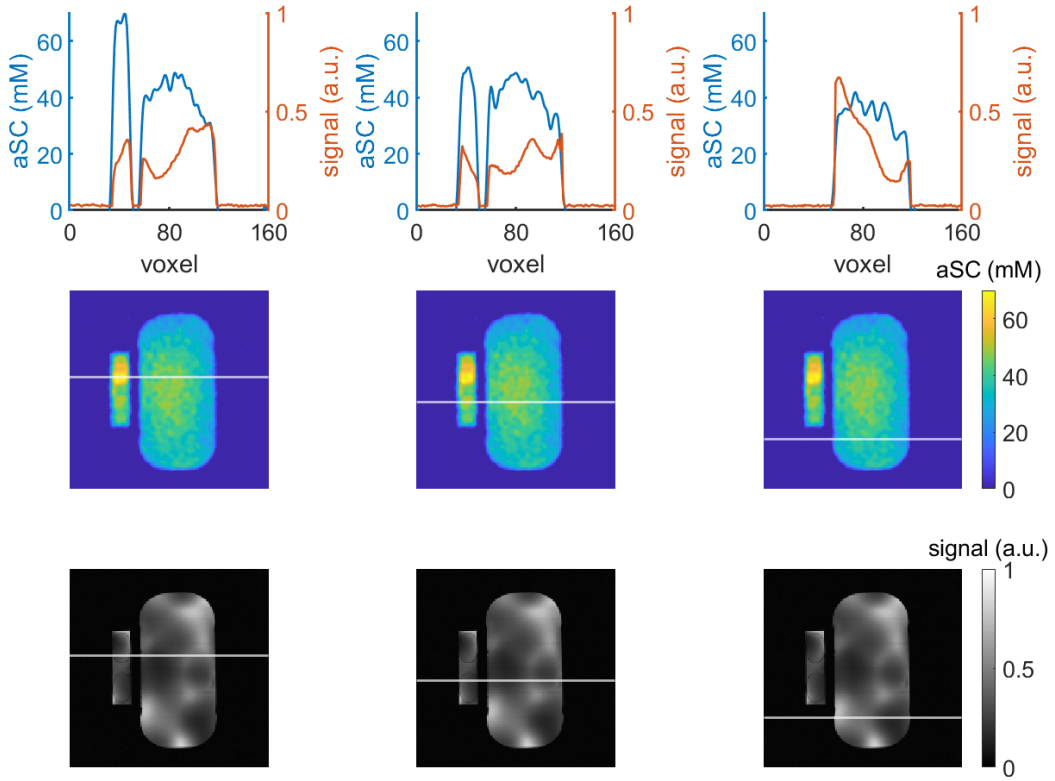

Figure A1: Alignment of ^{23}Na and ^{1}H images in the phantom for the anterior-posterior direction in a transversal slice. The line plot in the first row displays the values in the uncorrected ^{23}Na (blue line) and ^{1}H (orange line) MRI along the white line in the second and third row, respectively. For each plotted line through the phantom, the upper border of the phantom and reference vials in the ^{23}Na image correspond well to those in the ^{1}H image. In the third column, where the values are only in the phantom, the images are aligned well.

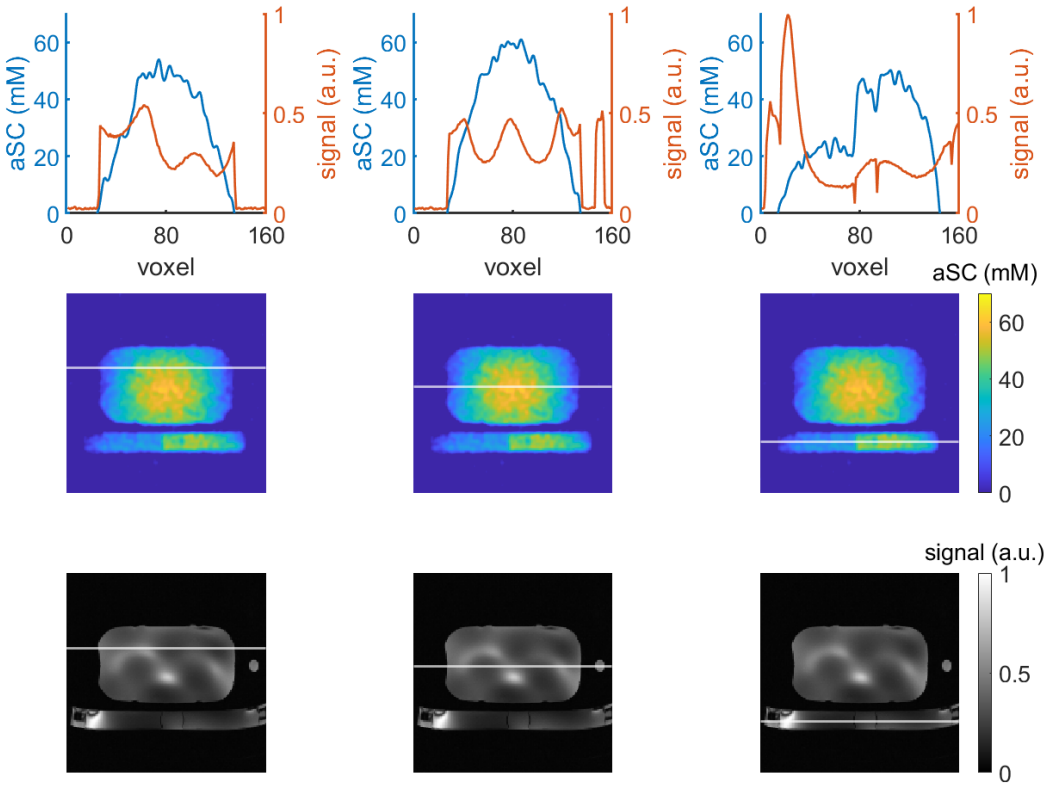

Figure A2: Alignment of ^{23}Na and ^{1}H images in the phantom for the cranial-caudal direction in a sagittal slice. The line plot in the first row displays the values in the uncorrected ^{23}Na (blue line) and ^{1}H (orange line) MRI along the white line in the second and third row, respectively. For each plotted line through the phantom, the ^{23}Na and ^{1}H image are well aligned. In the third column, where values within the reference vial setup are plotted, the signal decrease towards the edges in the ^{23}Na image leads to a line plot mismatch. For high |z|-values, gradient non-linearity artifacts can be observed in the ^{1}H MR images.

Publications

Parts of this work appear in the following conference contributions and publications:

Invited Talk

- **Anna K. Scheipers** "Quantitative Abdominal Sodium MRI at 7 T in Large Field-of-View" *ISMRM (International Society for Magnetic Resonance in Medicine) Joint Workshop of the Ultra-High Field MR & Brain Function Study Groups, Annapolis, MD, USA* (2025)

Conference Talks

- **Anna K. Scheipers**, Stephan Orzada, Johannes Grimm, Jana Losch, Thomas M. Fiedler, Armin M. Nagel, Sebastian Schmitter, Mark E. Ladd and Tanja Platt "Quantitative Abdominal Sodium MRI Combined with 32-Channel Proton pTx MRI at 7 T in a Large Field-of-View" *Proceedings of the 32nd Annual Meeting of the ISMRM, Singapore* (2024), Abstract 0522

- **Anna K. Scheipers** "Quantitative ^{23}Na MRI in the human torso" *X-nuclei User meeting, Prague, Czech Republic* (2023)

Conference e-Poster Presentations

- **Anna K. Scheipers**, Armin M. Nagel, Laurent Ruck, Lena V. Gast, Mark E. Ladd and Tanja Platt "Quantitative sodium MRI of the human kidneys at 7 T – Before, during and after water load via sliding window evaluation" *Proceedings of the 31st Annual Meeting of the ISMRM, Toronto, Canada* (2023), Abstract 7691

Study Group Presentations

- **Anna K. Scheipers** "Quantitative Abdominal Sodium MRI Combined with 32-Channel Proton pTx MRI at 7 T in a Large Field-of-View" *Abstract Nominee for Trainee Award during the Study Group Business Meeting of the ISMRM body MRI study group at the 32nd Annual Meeting of the ISMRM, Singapore* (2024), **1st place**

- **Anna K. Scheipers** "Quantitative Abdominal Sodium MRI Combined with 32-Channel Proton pTx MRI at 7 T in a Large Field-of-View" *Abstract Nominee for Trainee Award during the Study Group Business Meeting of the ISMRM X-nuclei study group at the 32nd Annual Meeting of the ISMRM, Singapore* (2024), **3rd place**

- **Anna K. Scheipers** "Quantitative sodium MRI of the human kidneys at 7 T – Before, during and after water load via sliding window evaluation" *Abstract Nominee for Trainee Award during the Study Group Business Meeting of the ISMRM high field study group at the 31st Annual Meeting of the ISMRM, Toronto, Canada* (2023), **1st place**

- **Anna K. Scheipers** "Quantitative sodium MRI of the human kidneys at 7 T – Before, during and after water load via sliding window evaluation" *Abstract Nominee for Trainee Award during the Study Group Business Meeting of the ISMRM renal study group at the 31st Annual Meeting of the ISMRM, Toronto, Canada* (2023), **1st place**

- **Anna K. Scheipers** "Quantitative sodium MRI of the human kidneys at 7 T – Before, during and after water load via sliding window evaluation" *Abstract Nominee for Trainee Award during the Study Group Business Meeting of the ISMRM X-nuclei study group at the 31st Annual Meeting of the ISMRM, Toronto, Canada* (2023), **2nd place**

Submitted Research Article

Parts of this thesis have been submitted to the journal of Magnetic Resonance in Medicine:

- **Anna K. Scheipers**, Johannes Grimm, Jana Losch, Stephan Orzada, Thomas M. Fiedler, Armin M. Nagel, Sebastian Schmitter, Mark E. Ladd and Tanja Platt "Quantitative Abdominal Sodium MRI Combined with 32-Channel Proton pTx MRI at 7 T in a Large Field-of-View"

Further Publications

Publications that are not included in this work:

- Jana Losch, **Anna K. Scheipers**, Johannes Grimm, Armin M. Nagel, Stephan Orzada, Sebastian Schmitter, Mark E. Ladd and Tanja Platt "Quantification of Apparent Tissue Sodium Concentration (aTSC) in the Healthy Liver via ^{23}Na and ^{1}H MRI at 7 T" *Proceedings of the 33rd Annual Meeting of the ISMRM, Honolulu, Hawai'i, USA* (2025)

- **Anna K. Scheipers**, Laurent Ruck, Armin M. Nagel, Sabine M. Matuschik, Mark E. Ladd, Tanja Platt and Lena V. Gast "Performance Comparison of Two RF Coils for Abdominal Sodium MRI at 7 T" *ISMRM Workshop on MR Imaging of X-Nuclei (^{23}Na & Friends), Marseille, France* (2023), Poster 6

- Laurent Ruck, Tobias Wilferth, Tanja Platt, **Anna K. Scheipers**, Christoph Kopp, Michael Uder and Armin M. Nagel "Time-resolved abdominal sodium MRI during uptake of saline solution at 7 Tesla" *ISMRM Workshop on MR Imaging of X-Nuclei (^{23}Na & Friends), Marseille, France* (2023)

- **Anna K. Scheipers**, Daniel Paech, Armin M. Nagel, Mark E. Ladd and Tanja Platt "Comparison of Measured and Setup-Specific Simulated B_1^+ Fields for Abdominal Sodium MRI at 7 T" *ISMRM Workshop on Ultra-High Field MR* (2022), Poster 64

- **Anna K. Scheipers**, Daniel Paech, Armin M. Nagel, Mark E. Ladd and Tanja Platt "Quantitative Sodium MRI of the Intervertebral Discs at 7 T" *Proceedings of the 30th Annual Meeting of the ISMRM, London, England* (2022), Abstract 4370

Bibliography

Abragam, A. (1961). *The Principles of Nuclear Magnetism*. Clarendon Press. 666 pp. ISBN: 978-0-19-852014-6.

Akbari, Alireza et al. (2022). "Functional Sodium MRI Helps to Measure Corticomedullary Sodium Content in Normal and Diseased Human Kidneys". In: *Radiology* 303.2, pp. 384–389. ISSN: 0033-8419. DOI: 10.1148/radiol.211238.

Barrett, Tristan et al. (2018). "Quantification of Total and Intracellular Sodium Concentration in Primary Prostate Cancer and Adjacent Normal Prostate Tissue With Magnetic Resonance Imaging". In: *Investigative Radiology* 53.8, pp. 450–456. ISSN: 0020-9996. DOI: 10.1097/RLI.0000000000000470.

Bartholdi, E and R. R Ernst (1973). "Fourier spectroscopy and the causality principle". In: *Journal of Magnetic Resonance (1969)* 11.1, pp. 9–19. ISSN: 0022-2364. DOI: 10.1016/0022-2364(73)90076-0.

Bernstein, Matt A., Kevin F. King, and Xiaohong Joe Zhou (2004). *Handbook of MRI Pulse Sequences*. Elsevier. 1041 pp. ISBN: 978-0-08-053312-4.

Birchall, Jonathan Richard et al. (2024). "Quantitative 23Na magnetic resonance imaging in the abdomen at 3 T". In: *Magnetic Resonance Materials in Physics, Biology and Medicine* 37.4, pp. 737–748. ISSN: 1352-8661. DOI: 10.1007/s10334-024-01167-6.

Bloch, F. (1946). "Nuclear Induction". In: *Physical Review* 70.7, pp. 460–474. ISSN: 0031-899X. DOI: 10.1103/PhysRev.70.460.

Bloembergen, N., E. M. Purcell, and R. V. Pound (1948). "Relaxation Effects in Nuclear Magnetic Resonance Absorption". In: *Physical Review* 73.7, pp. 679–712. ISSN: 0031-899X. DOI: 10.1103/PhysRev.73.679.

Boehmert, Laura et al. (2019). "Cardiorenal sodium MRI at 7.0 Tesla using a 4/4 channel 1H/23Na radiofrequency antenna array". In: *Magnetic Resonance in Medicine* 82.6, pp. 2343–2356. ISSN: 1522-2594. DOI: 10.1002/mrm.27880.

Borthakur, Arijitt et al. (2006). "Sodium and T1rho MRI for molecular and diagnostic imaging of articular cartilage". In: *NMR in Biomedicine* 19.7, pp. 781–821. ISSN: 1099-1492. DOI: 10.1002/nbm.1102.

Bottomley, Paul A. (2016). "Sodium MRI in human heart: a review". In: *NMR in Biomedicine* 29.2, pp. 187–196. ISSN: 1099-1492. DOI: 10.1002/nbm.3265.

Brown, Robert W. et al. (2014). *Magnetic Resonance Imaging: Physical Principles and Sequence Design*. John Wiley & Sons. 976 pp. ISBN: 978-0-471-72085-0.

Bruin, Paul W. de et al. (2015). "Time-efficient interleaved human 23Na and 1H data acquisition at 7 T". In: *NMR in Biomedicine* 28.10, pp. 1228–1235. ISSN: 1099-1492. DOI: 10.1002/nbm.3368.

Budinger, Thomas F. et al. (2016). "Toward 20 T magnetic resonance for human brain studies: opportunities for discovery and neuroscience rationale". In: *Magnetic Resonance Materials in Physics, Biology and Medicine* 29.3, pp. 617–639. ISSN: 1352-8661. DOI: 10.1007/s10334-016-0561-4.

Buerger, C. et al. (2012). "Nonrigid Motion Modeling of the Liver From 3-D Undersampled Self-Gated Golden-Radial Phase Encoded MRI". In: *IEEE Transactions on Medical Imaging* 31.3, pp. 805–815. ISSN: 1558-254X. DOI: 10.1109/TMI.2011.2181997.

Burnier, Michel et al. (2000). "Renal sodium handling in acute and chronic salt loading/depletion protocols: the confounding influence of acute water loading". In: *Journal of Hypertension* 18.11, p. 1657. ISSN: 0263-6352.

Çavuşoğlu, Mustafa et al. (2022). "Quantitative 23Na-MRI of the intervertebral disk at 3 T". In: *NMR in Biomedicine* 35.8, e4733. ISSN: 1099-1492. DOI: 10.1002/nbm.4733.

Chan, Rachel W. et al. (2009). "Temporal stability of adaptive 3D radial MRI using multidimensional golden means". In: *Magnetic Resonance in Medicine* 61.2, pp. 354–363. ISSN: 1522-2594. DOI: 10.1002/mrm.21837.

Christ, Andreas et al. (2009). "The Virtual Family—development of surface-based anatomical models of two adults and two children for dosimetric simulations". In: *Physics in Medicine & Biology* 55.2, N23. ISSN: 0031-9155. DOI: 10.1088/0031-9155/55/2/N01.

Christa, Martin et al. (2019). "Increased myocardial sodium signal intensity in Conn's syndrome detected by 23Na magnetic resonance imaging". In: *European Heart Journal - Cardiovascular Imaging* 20.3, pp. 263–270. ISSN: 2047-2404. DOI: 10.1093/ehjci/jey134.

Clausen, Torben (2003). "Na+-K+ Pump Regulation and Skeletal Muscle Contractility". In: *Physiological Reviews* 83.4, pp. 1269–1324. ISSN: 0031-9333. DOI: 10.1152/physrev.00011.2003.

Collins, Christopher M. and Zhangwei Wang (2011). "Calculation of radiofrequency electromagnetic fields and their effects in MRI of human subjects". In: *Magnetic Resonance in Medicine* 65.5, pp. 1470–1482. ISSN: 1522-2594. DOI: 10.1002/mrm.22845.

Commissioner, Office of the (2024). *FDA clears first 7T magnetic resonance imaging device*. FDA. URL: https://www.fda.gov/news-events/press-announcements/fda-clears-first-7t-magnetic-resonance-imaging-device (visited on 09/19/2024).

DAK V2.4 Application Note: DAK/DAKS Best Practices (2017).

Daniel, Alexander J. et al. (2021). "Automated renal segmentation in healthy and chronic kidney disease subjects using a convolutional neural network". In: *Magnetic Resonance in Medicine* 86.2, pp. 1125–1136. ISSN: 1522-2594. DOI: 10.1002/mrm.28768.

Dietrich, Sebastian et al. (2021). "3D Free-breathing multichannel absolute Mapping in the human body at 7T". In: *Magnetic Resonance in Medicine* 85.5, pp. 2552–2567. ISSN: 1522-2594. DOI: 10.1002/mrm.28602.

Felz, Jana et al. (2023). "Development of a Pulse Sequence with Alternating Excitation for Respiratory-Sorted B1+ and B0 Field Mapping in 23Na Human Torso MRI". In: Proc. Intl. Soc. Mag. Reson. Med. Toronto, Abstract #0114.

Feng, Li et al. (2016). "XD-GRASP: Golden-angle radial MRI with reconstruction of extra motion-state dimensions using compressed sensing". In: *Magnetic Resonance in Medicine* 75.2, pp. 775–788. ISSN: 1522-2594. DOI: 10.1002/mrm.25665.

Fessler, J.A. and B.P. Sutton (2003). "Nonuniform fast Fourier transforms using min-max interpolation". In: *IEEE Transactions on Signal Processing* 51.2, pp. 560–574. ISSN: 1941-0476. DOI: 10.1109/TSP.2002.807005.

Fiedler, Thomas et al. (2024). "Real-time SAR Supervision for a 32-channel RF Transmit System with Virtual Observation Points". In: Proc. Intl. Soc. Mag. Reson. Med. Singapore, Abstract #3747. DOI: 10.58530/2024/3747.

Fiedler, Thomas M., Mark E. Ladd, and Andreas K. Bitz (2018). "SAR Simulations & Safety". In: *NeuroImage*. Neuroimaging with Ultra-high Field MRI: Present and Future 168, pp. 33–58. ISSN: 1053-8119. DOI: 10.1016/j.neuroimage.2017.03.035.

Furey, Andrew T. (1966). "Hyponatremia after choledochostomy and T tube drainage". In: *The American Journal of Surgery* 112.6, pp. 850–855. ISSN: 0002-9610. DOI: 10.1016/0002-9610(66)90137-1.

Gabriel, S., R. W. Lau, and C. Gabriel (1996). "The dielectric properties of biological tissues: II. Measurements in the frequency range 10 Hz to 20 GHz". In: *Physics in Medicine & Biology* 41.11, p. 2251. ISSN: 0031-9155. DOI: 10.1088/0031-9155/41/11/002.

Gast, Lena V. et al. (2023). "Recent technical developments and clinical research applications of sodium (23Na) MRI". In: *Progress in Nuclear Magnetic Resonance Spectroscopy* 138-139, pp. 1–51. ISSN: 0079-6565. DOI: 10.1016/j.pnmrs.2023.04.002.

Gerhalter, Teresa, Lena V. Gast, Benjamin Marty, Jan Martin, et al. (2019). "23Na MRI depicts early changes in ion homeostasis in skeletal muscle tissue of patients with duchenne muscular dystrophy". In: *Journal of Magnetic Resonance Imaging* 50.4, pp. 1103–1113. ISSN: 1522-2586. DOI: 10.1002/jmri.26681.

Gerhalter, Teresa, Lena V. Gast, Benjamin Marty, Michael Uder, et al. (2020). "Assessing the variability of 23Na MRI in skeletal muscle tissue: Reproducibility and repeatability of tissue sodium concentration measurements in the lower leg

at 3 T". In: *NMR in Biomedicine* 33.5, e4279. ISSN: 1099-1492. DOI: 10.1002/nbm.4279.

Graaf, Robin A. de et al. (2006). "High magnetic field water and metabolite proton T1 and T2 relaxation in rat brain in vivo". In: *Magnetic Resonance in Medicine* 56.2, pp. 386–394. ISSN: 1522-2594. DOI: 10.1002/mrm.20946.

Graessl, Andreas et al. (2015). "Sodium MRI of the human heart at 7.0 T: preliminary results". In: *NMR in Biomedicine* 28.8, pp. 967–975. ISSN: 1099-1492. DOI: 10.1002/nbm.3338.

Graham, Paul P. et al. (1982). "Mineral Element Composition of Bovine Spleen and Separated Spleen Components". In: *Journal of Food Science* 47.3, pp. 720–722. ISSN: 1750-3841. DOI: 10.1111/j.1365-2621.1982.tb12699.x.

Grimm, Johannes et al. (2024). "A comparison of various custom-built pTx RF arrays for body imaging at 7T with regard to their transmit efficiency". In: Proc. Intl. Soc. Mag. Reson. Med. Singapore, Abstract #4943. DOI: 10.58530/2024/4943.

Grist, James T. et al. (2020). "Visualization of sodium dynamics in the kidney by magnetic resonance imaging in a multi-site study". In: *Kidney International* 98.5, pp. 1174–1178. ISSN: 0085-2538. DOI: 10.1016/j.kint.2020.04.056.

Griswold, Mark A. et al. (2002). "Generalized autocalibrating partially parallel acquisitions (GRAPPA)". In: *Magnetic Resonance in Medicine* 47.6, pp. 1202–1210. ISSN: 1522-2594. DOI: 10.1002/mrm.10171.

Haneder, Stefan, Johannes Michael Budjan, et al. (2015). "Dose-dependent changes in renal 1H-/23Na MRI after adjuvant radiochemotherapy for gastric cancer". In: *Strahlentherapie und Onkologie* 191.4, pp. 356–364. ISSN: 1439-099X. DOI: 10.1007/s00066-014-0787-x.

Haneder, Stefan, Vladimir Juras, et al. (2014). "In vivo sodium (23Na) imaging of the human kidneys at 7 T: Preliminary results". In: *European Radiology* 24.2, pp. 494–501. ISSN: 1432-1084. DOI: 10.1007/s00330-013-3032-6.

Haneder, Stefan, Paul Kettnaker, et al. (2013). "Quantitative in vivo 23Na MR imaging of the healthy human kidney: determination of physiological ranges at 3.0T with comparison to DWI and BOLD". In: *Magnetic Resonance Materials*

in Physics, Biology and Medicine 26.6, pp. 501–509. ISSN: 1352-8661. DOI: 10.1007/s10334-013-0369-4.

Haneder, Stefan, Simon Konstandin, et al. (2011). "Quantitative and Qualitative 23Na MR Imaging of the Human Kidneys at 3 T: Before and after a Water Load". In: *Radiology* 260.3, pp. 857–865. ISSN: 0033-8419. DOI: 10.1148/radiol.11102263.

Harrington, Michael G. et al. (2010). "Cerebrospinal fluid sodium rhythms". In: *Cerebrospinal Fluid Research* 7, p. 3. DOI: 10.1186/1743-8454-7-3.

Harris, Robin K. et al. (2001). "NMR nomenclature. Nuclear spin properties and conventions for chemical shifts(IUPAC Recommendations 2001)". In: *Pure and Applied Chemistry* 73.11, pp. 1795–1818. ISSN: 0033-4545, 1365-3075. DOI: 10.1351/pac200173111795.

Hausmann, Daniel et al. (2012). "Apparent Diffusion Coefficient and Sodium Concentration Measurements in Human Prostate Tissue via Hydrogen-1 and Sodium-23 Magnetic Resonance Imaging in a Clinical Setting at 3 T". In: *Investigative Radiology* 47.12, p. 677. DOI: 10.1097/RLI.0b013e318267bc6f.

Heinrich, Peter C., Matthias Müller, and Lutz Graeve, eds. (2014). *Löffler/Petrides Biochemie und Pathobiochemie*. Springer-Lehrbuch. Berlin, Heidelberg: Springer. ISBN: 978-3-642-17972-3. DOI: 10.1007/978-3-642-17972-3.

Hellerbach, Alexandra et al. (2013). "MRI Phantoms – Are There Alternatives to Agar?" In: *PLOS ONE* 8.8, e70343. ISSN: 1932-6203. DOI: 10.1371/journal.pone.0070343.

Henzler, T. et al. (2012). "Imaging of Tumor Viability in Lung Cancer: Initial Results Using 23Na-MRI". In: *RöFo - Fortschritte auf dem Gebiet der Röntgenstrahlen und der bildgebenden Verfahren* 184.4, pp. 340–344. ISSN: 1438-9029, 1438-9010. DOI: 10.1055/s-0031-1299277.

Hilal, Sadek K. et al. (1985). "In Vivo NMR Imaging of Sodium-23 in the Human Head". In: *Journal of Computer Assisted Tomography* 9.1, p. 1. ISSN: 0363-8715.

Hooper, G and D A Dick (1976). "Nonuniform distribution of sodium in the rat hepatocyte." In: *Journal of General Physiology* 67.4, pp. 469–474. ISSN: 0022-1295. DOI: 10.1085/jgp.67.4.469.

Hoult, D.I. (2000). "The principle of reciprocity in signal strength calculations - A mathematical guide". In: *Concepts in Magnetic Resonance* 12.4, pp. 173–187. ISSN: 1099-0534. DOI: 10.1002/1099-0534(2000)12:4<173::AID-CMR1>3.0.CO;2-Q.

Hu, Ruomin et al. (2020). "X-nuclei imaging: Current state, technical challenges, and future directions". In: *Journal of Magnetic Resonance Imaging* 51.2, pp. 355–376. ISSN: 1522-2586. DOI: 10.1002/jmri.26780.

Hubbard, P. (1970). "Nonexponential Nuclear Magnetic Relaxation by Quadrupole Interactions". In: *The Journal of Chemical Physics* 53.3, pp. 985–987. ISSN: 0021-9606. DOI: 10.1063/1.1674167.

Huhn, Konstantin et al. (2019). "Potential of Sodium MRI as a Biomarker for Neurodegeneration and Neuroinflammation in Multiple Sclerosis". In: *Frontiers in Neurology* 10. ISSN: 1664-2295. DOI: 10.3389/fneur.2019.00084.

Ianniello, Carlotta et al. (2019). "A dual-tuned multichannel bilateral RF coil for 1H/23Na breast MRI at 7 T". In: *Magnetic Resonance in Medicine* 82.4, pp. 1566–1575. ISSN: 1522-2594. DOI: 10.1002/mrm.27829.

Insko, Erik K and Lizann Bolinger (1993). "Mapping of the Radiofrequency Field". In: *Journal of Magnetic Resonance, Series A* 103.1, pp. 82–85. ISSN: 1064-1858. DOI: 10.1006/jmra.1993.1133.

Insko, Erik K, David B Clayton, and Mark A Elliott (2002). "In Vivo Sodium MR Imaging of the Intervertebral Disk at 4 T". In: *Academic Radiology* 9.7, pp. 800–804. ISSN: 1076-6332. DOI: 10.1016/S1076-6332(03)80350-1.

Jaccard, Guy, Stephen Wimperis, and Geoffrey Bodenhausen (1986). "Multiple-quantum NMR spectroscopy of S=3/2 spins in isotropic phase: A new probe for multiexponential relaxation". In: *The Journal of Chemical Physics* 85.11, pp. 6282–6293. ISSN: 0021-9606. DOI: 10.1063/1.451458.

Jacobs, Michael A. et al. (2009). "Proton, diffusion-weighted imaging, and sodium (23Na) MRI of uterine leiomyomata after MR-guided high-intensity focused ultrasound: A preliminary study". In: *Journal of Magnetic Resonance Imaging* 29.3, pp. 649–656. ISSN: 1522-2586. DOI: 10.1002/jmri.21677.

James, Judy R. et al. (2015). "In vivo sodium MR imaging of the abdomen at 3T". In: *Abdominal imaging* 40.7, p. 2272. DOI: 10.1007/s00261-015-0428-6.

Kamp, Benedikt et al. (2024). "Sodium MRI of the Lumbar Intervertebral Discs of the Human Spine: An Ex Vivo Study". In: *Journal of Magnetic Resonance Imaging*. ISSN: 1522-2586. DOI: 10.1002/jmri.29521.

Kirillov, Alexander et al. (2023). "Segment Anything". In: *2023 IEEE/CVF International Conference on Computer Vision (ICCV)*. 2023 IEEE/CVF International Conference on Computer Vision (ICCV), pp. 3992–4003. DOI: 10.1109/ICCV51070.2023.00371.

Konstandin, Simon and Armin M. Nagel (2014). "Measurement techniques for magnetic resonance imaging of fast relaxing nuclei". In: *Magnetic Resonance Materials in Physics, Biology and Medicine* 27.1, pp. 5–19. ISSN: 1352-8661. DOI: 10.1007/s10334-013-0394-3.

Kraff, Oliver et al. (2015). "MRI at 7 tesla and above: Demonstrated and potential capabilities". In: *Journal of Magnetic Resonance Imaging* 41.1, pp. 13–33. ISSN: 1522-2586. DOI: 10.1002/jmri.24573.

Kratzer, Fabian J. et al. (2021). "3D sodium (23Na) magnetic resonance fingerprinting for time-efficient relaxometric mapping". In: *Magnetic Resonance in Medicine* 86.5, pp. 2412–2425. ISSN: 1522-2594. DOI: 10.1002/mrm.28873.

Ladd, Mark E. et al. (2018). "Pros and cons of ultra-high-field MRI/MRS for human application". In: *Progress in Nuclear Magnetic Resonance Spectroscopy* 109, pp. 1–50. ISSN: 0079-6565. DOI: 10.1016/j.pnmrs.2018.06.001.

Lauterbur, P. C. (1973). "Image Formation by Induced Local Interactions: Examples Employing Nuclear Magnetic Resonance". In: *Nature* 242.5394, pp. 190–191. ISSN: 1476-4687. DOI: 10.1038/242190a0.

Lauzon, M. Louis and Brian K. Rutt (1996). "Effects of polar sampling in k-space". In: *Magnetic Resonance in Medicine* 36.6, pp. 940–949. ISSN: 1522-2594. DOI: 10.1002/mrm.1910360617.

Lemoine, Sandrine et al. (2024). "Redefining the concept of residual renal function with kidney sodium MRI: a pilot study". In: *Nephrology Dialysis Transplantation* 39.11, pp. 1809–1816. ISSN: 0931-0509. DOI: 10.1093/ndt/gfae070.

Liu, Fusheng et al. (2023). "Bile liquid biopsy in biliary tract cancer". In: *Clinica Chimica Acta* 551, p. 117593. ISSN: 0009-8981. DOI: 10.1016/j.cca.2023.117593.

Lommen, Jonathan et al. (2016). "Enhancing the quantification of tissue sodium content by MRI: time-efficient sodium B1 mapping at clinical field strengths". In: *NMR in Biomedicine* 29.2, pp. 129–136. ISSN: 1099-1492. DOI: 10.1002/nbm.3292.

Lopez Kolkovsky, Alfredo L. et al. (2022). "Interleaved and simultaneous multinuclear magnetic resonance in vivo. Review of principles, applications and potential". In: *NMR in Biomedicine* 35.10, e4735. ISSN: 1099-1492. DOI: 10.1002/nbm.4735.

Lott, Johanna (2020). "In-vivo 23Na-Magnetresonanztomographie am Herzen bei 7 Tesla". Dissertation. DOI: 10.11588/heidok.00028382.

Lott, Johanna, Nicolas G.R. Behl, et al. (2019). "Quantitative 23Na MRI of the human liver at 7 Tesla". In: Proc. Intl. Soc. Mag. Reson. Med. Montréal, QC Canada, Abstract #0487.

Lott, Johanna, Tanja Platt, et al. (2019). "Corrections of myocardial tissue sodium concentration measurements in human cardiac 23Na MRI at 7 Tesla". In: *Magnetic Resonance in Medicine* 82.1, pp. 159–173. ISSN: 1522-2594. DOI: 10.1002/mrm.27703.

Lu, Aiming et al. (2010). "Quantitative sodium imaging with a flexible twisted projection pulse sequence". In: *Magnetic Resonance in Medicine* 63.6, pp. 1583–1593. ISSN: 1522-2594. DOI: 10.1002/mrm.22381.

Lustig, Michael, David Donoho, and John M. Pauly (2007). "Sparse MRI: The application of compressed sensing for rapid MR imaging". In: *Magnetic Resonance in Medicine* 58.6, pp. 1182–1195. ISSN: 1522-2594. DOI: 10.1002/mrm.21391.

Ma, Jun et al. (2024). "Segment anything in medical images". In: *Nature Communications* 15.1, p. 654. ISSN: 2041-1723. DOI: 10.1038/s41467-024-44824-z.

Maarel, Johan R. C. van der (2003). "Thermal relaxation and coherence dynamics of spin 3/2. I. Static and fluctuating quadrupolar interactions in the multipole

basis". In: *Concepts in Magnetic Resonance Part A* 19A.2, pp. 97–116. ISSN: 1552-5023. DOI: 10.1002/cmr.a.10087.

Madelin, Guillaume, Alexej Jerschow, and Ravinder R. Regatte (2012). "Sodium relaxation times in the knee joint in vivo at 7T". In: *NMR in Biomedicine* 25.4, pp. 530–537. ISSN: 1099-1492. DOI: 10.1002/nbm.1768.

Madelin, Guillaume, Jae-Seung Lee, et al. (2014). "Sodium MRI: Methods and applications". In: *Progress in Nuclear Magnetic Resonance Spectroscopy* 79, pp. 14–47. ISSN: 0079-6565. DOI: 10.1016/j.pnmrs.2014.02.001.

Madelin, Guillaume and Ravinder R. Regatte (2013). "Biomedical applications of sodium MRI in vivo". In: *Journal of Magnetic Resonance Imaging* 38.3, pp. 511–529. ISSN: 1522-2586. DOI: 10.1002/jmri.24168.

Madelin, Guillaume, Ding Xia, et al. (2018). "Longitudinal study of sodium MRI of articular cartilage in patients with knee osteoarthritis: initial experience with 16-month follow-up". In: *European Radiology* 28.1, pp. 133–142. ISSN: 1432-1084. DOI: 10.1007/s00330-017-4956-z.

Malzacher, Matthias et al. (2016). "Sodium-23 MRI of whole spine at 3 Tesla using a 5-channel receive-only phased-array and a whole-body transmit resonator". In: *Zeitschrift für Medizinische Physik* 26.1, pp. 95–100. ISSN: 0939-3889. DOI: 10.1016/j.zemedi.2015.03.008.

Maril, Nimrod, Raanan Margalit, et al. (2004). "Functional sodium magnetic resonance imaging of the intact rat kidney". In: *Kidney International* 65.3, pp. 927–935. ISSN: 0085-2538. DOI: 10.1111/j.1523-1755.2004.00475.x.

Maril, Nimrod, Yael Rosen, et al. (2006). "Sodium MRI of the human kidney at 3 Tesla". In: *Magnetic Resonance in Medicine* 56.6, pp. 1229–1234. ISSN: 1522-2594. DOI: 10.1002/mrm.21031.

Maudsley, A. A. and S. K. Hilal (1984). "Biological Aspects of Sodium-23 Imaging". In: *British Medical Bulletin* 40.2, pp. 165–166. ISSN: 0007-1420. DOI: 10.1093/oxfordjournals.bmb.a071964.

Mellon, E. A. et al. (2009). "Sodium MR Imaging Detection of Mild Alzheimer Disease: Preliminary Study". In: *American Journal of Neuroradiology* 30.5, pp. 978–984. ISSN: 0195-6108, 1936-959X. DOI: 10.3174/ajnr.A1495.

Meyer, Melissa M. et al. (2019). "Cerebral sodium (23Na) magnetic resonance imaging in patients with migraine — a case-control study". In: *European Radiology* 29.12, pp. 7055–7062. ISSN: 1432-1084. DOI: 10.1007/s00330-019-06299-1.

Moon, Chan Hong, Alessandro Furlan, et al. (2014). "Quantitative sodium MR imaging of native versus transplanted kidneys using a dual-tuned proton/sodium (1H/23Na) coil: initial experience". In: *European Radiology* 24.6, pp. 1320–1326. ISSN: 1432-1084. DOI: 10.1007/s00330-014-3138-5.

Moon, Chan Hong, Jung-Hwan Kim, et al. (2011). "In Vivo Sodium and Proton T1rho MR Imaging of Human Spine Disc at 3T". In: Proc. Intl. Soc. Mag. Reson. Med. Montréal, QC Canada, Abstract #3244.

Moortele, P-F Van de and K Ugurbil (2009). "Very Fast Multi Channel B1 Calibration at High Field in the Small Flip Angle Regime". In: Proc. Intl. Soc. Mag. Reson. Med. Honolulu, HI United States, Abstract #0367.

Nagel, Armin M. (2009). "Natrium-Magnetresonanztomographie : Entwicklung einer 3D radialen Messtechnik mit optimierter k-Raum-Abtastdichte und hoher SNR-Effizienz". Dissertation. DOI: 10.11588/heidok.00009339.

Nagel, Armin M., Erick Amarteifio, et al. (2011). "3 Tesla Sodium Inversion Recovery Magnetic Resonance Imaging Allows for Improved Visualization of Intracellular Sodium Content Changes in Muscular Channelopathies". In: *Investigative Radiology* 46.12, pp. 759–766. ISSN: 0020-9996. DOI: 10.1097/RLI.0b013e31822836f6.

Nagel, Armin M., Frederik B. Laun, et al. (2009). "Sodium MRI using a density-adapted 3D radial acquisition technique". In: *Magnetic Resonance in Medicine* 62.6, pp. 1565–1573. ISSN: 1522-2594. DOI: 10.1002/mrm.22157.

Nagel, Armin M., Frank Lehmann-Horn, et al. (2014). "In Vivo 35Cl MR Imaging in Humans: A Feasibility Study". In: *Radiology* 271.2, pp. 585–595. ISSN: 0033-8419. DOI: 10.1148/radiol.13131725.

Niesporek, Sebastian C. et al. (2015). "Partial volume correction for in vivo 23Na-MRI data of the human brain". In: *NeuroImage* 112, pp. 353–363. ISSN: 1053-8119. DOI: 10.1016/j.neuroimage.2015.03.025.

Orzada, Stephan, Stefan Maderwald, et al. (2010). "RF excitation using time interleaved acquisition of modes (TIAMO) to address B1 inhomogeneity in high-field MRI". In: *Magnetic Resonance in Medicine* 64.2, pp. 327–333. ISSN: 1522-2594. DOI: 10.1002/mrm.22527.

Orzada, Stephan, Klaus Solbach, et al. (2019). "A 32-channel parallel transmit system add-on for 7T MRI". In: *PLOS ONE* 14.9, e0222452. ISSN: 1932-6203. DOI: 10.1371/journal.pone.0222452.

Ouwerkerk, Ronald, Karen B. Bleich, et al. (2003). "Tissue Sodium Concentration in Human Brain Tumors as Measured with 23Na MR Imaging". In: *Radiology* 227.2, pp. 529–537. ISSN: 0033-8419. DOI: 10.1148/radiol.2272020483.

Ouwerkerk, Ronald, Paul A. Bottomley, et al. (2008). "Tissue Sodium Concentration in Myocardial Infarction in Humans: A Quantitative 23Na MR Imaging Study". In: *Radiology* 248.1, pp. 88–96. ISSN: 0033-8419. DOI: 10.1148/radiol.2481071027.

Ouwerkerk, Ronald, Michael A. Jacobs, et al. (2007). "Elevated tissue sodium concentration in malignant breast lesions detected with non-invasive 23Na MRI". In: *Breast Cancer Research and Treatment* 106.2, pp. 151–160. ISSN: 1573-7217. DOI: 10.1007/s10549-006-9485-4.

Ouwerkerk, Ronald, Robert G. Weiss, and Paul A. Bottomley (2005). "Measuring human cardiac tissue sodium concentrations using surface coils, adiabatic excitation, and twisted projection imaging with minimal T2 losses". In: *Journal of Magnetic Resonance Imaging* 21.5, pp. 546–555. ISSN: 1522-2586. DOI: 10.1002/jmri.20322.

Padormo, Francesco et al. (2016). "Parallel transmission for ultrahigh-field imaging". In: *NMR in Biomedicine* 29.9, pp. 1145–1161. ISSN: 1099-1492. DOI: 10.1002/nbm.3313.

Pape, Hans-Christian, Armin Kurtz, and Stefan Silbernagl (2023). *Physiologie*. 10th ed. Thieme. 1088 pp. ISBN: 978-3-13-244610-6.

Platt, Tanja (2018). "In-vivo-^{23}Na-Magnetresonanztomographie des Körperstamms bei 7 Tesla". PhD thesis. DOI: 10.11588/heidok.00024043.

Platt, Tanja, Thomas M. Fiedler, et al. (2016). "Development and Application of a 23Na Elliptical Body Coil for 7 Tesla". In: *Procedings of the 24th Annual Meeting of the ISMRM, Singapore*.

Platt, Tanja, Mark E. Ladd, and Daniel Paech (2021). "7 Tesla and Beyond: Advanced Methods and Clinical Applications in Magnetic Resonance Imaging". In: *Investigative Radiology* 56.11, p. 705. DOI: 10.1097/RLI.0000000000000820.

Platt, Tanja, Reiner Umathum, et al. (2018). "In vivo self-gated 23Na MRI at 7 T using an oval-shaped body resonator". In: *Magnetic Resonance in Medicine* 80.3, pp. 1005–1019. ISSN: 1522-2594. DOI: 10.1002/mrm.27103.

Pruessmann, Klaas P. et al. (1999). "SENSE: Sensitivity encoding for fast MRI". In: *Magnetic Resonance in Medicine* 42.5, pp. 952–962. ISSN: 1522-2594. DOI: 10.1002/(SICI)1522-2594(199911)42:5<952::AID-MRM16>3.0.CO;2-S.

Rakhmanov, E. A., E. B. Saff, and Y. M. Zhou (1994). "Minimal Discrete Energy on the Sphere". In: *Mathematical Research Letters* 1.6, pp. 647–662. ISSN: 10732780, 1945001X. DOI: 10.4310/MRL.1994.v1.n6.a3.

Reetz, Kathrin et al. (2012). "Increased brain tissue sodium concentration in Huntington's Disease — A sodium imaging study at 4 T". In: *NeuroImage* 63.1, pp. 517–524. ISSN: 1053-8119. DOI: 10.1016/j.neuroimage.2012.07.009.

Regnery, Sebastian et al. (2020). "Ultra-high-field sodium MRI as biomarker for tumor extent, grade and IDH mutation status in glioma patients". In: *NeuroImage: Clinical* 28, p. 102427. ISSN: 2213-1582. DOI: 10.1016/j.nicl.2020.102427.

Reiser, Maximilian F., Wolfhard Semmler, and Hedvig Hricak, eds. (2008). *Magnetic Resonance Tomography*. Berlin, Heidelberg: Springer. ISBN: 978-3-540-29355-2. DOI: 10.1007/978-3-540-29355-2_1.

Resetar, Ana et al. (2015). "Retrospectively-gated CINE 23Na imaging of the heart at 7.0Tesla using density-adapted 3D projection reconstruction". In: *Magnetic Resonance Imaging* 33.9, pp. 1091–1097. ISSN: 0730-725X. DOI: 10.1016/j.mri.2015.06.012.

Roemer, P. B. et al. (1990). "The NMR phased array". In: *Magnetic Resonance in Medicine* 16.2, pp. 192–225. ISSN: 1522-2594. DOI: 10.1002/mrm.1910160203.

Ronco, Claudio et al. (2008). "Cardiorenal Syndrome". In: *Journal of the American College of Cardiology* 52.19, pp. 1527–1539. DOI: 10.1016/j.jacc.2008.07.051.

Ruck, Laurent et al. (2024). "Interleaved 23Na/1H (pTx) MRI of the human heart at 7 Tesla". In: Proc. Intl. Soc. Mag. Reson. Med. Singapore, Abstract #0926. DOI: 10.58530/2024/0926.

Sandstede, Joern J. W. et al. (2004). "Time course of 23Na signal intensity after myocardial infarction in humans". In: *Magnetic Resonance in Medicine* 52.3, pp. 545–551. ISSN: 1522-2594. DOI: 10.1002/mrm.20165.

Schmidt, Simon et al. (2022). "First in-vivo 23Na human imaging at 10.5T using a combined 23Na-loop 1H-dipole transceiver array". In: Proc. Intl. Soc. Mag. Reson. Med. London, England, UK, Abstract #0383. DOI: 10.58530/2022/0383.

Serai, Suraj D. et al. (2023). "MR Physics, Hardware Considerations, and Practical Steps for Clinical MRI of the Kidney". In: *Advanced Clinical MRI of the Kidney: Methods and Protocols*. Ed. by Suraj D. Serai and Kassa Darge. Cham: Springer International Publishing, pp. 13–46. ISBN: 978-3-031-40169-5. DOI: 10.1007/978-3-031-40169-5_2.

Slichter, Charles Pence (1990). *Principles of magnetic resonance*. 3rd ed. Vol. 1. Springer series in solid-state sciences. Springer. 655 pp. ISBN: 978-3-540-50157-2.

Speckmann, Erwin-Josef, Jürgen Hescheler, and Rüdiger Köhling (2024). *Physiologie*. 8th ed. Urban & Fischer Verlag/Elsevier GmbH. 966 pp. ISBN: 978-3-437-41104-5.

Stobbe, Robert and Christian Beaulieu (2008). "Advantage of sampling density weighted apodization over postacquisition filtering apodization for sodium MRI of the human brain". In: *Magnetic Resonance in Medicine* 60.4, pp. 981–986. ISSN: 1522-2594. DOI: 10.1002/mrm.21738.

Stobbe, Robert W. and Christian Beaulieu (2016). "Residual quadrupole interaction in brain and its effect on quantitative sodium imaging". In: *NMR in Biomedicine* 29.2, pp. 119–128. ISSN: 1099-1492. DOI: 10.1002/nbm.3376.

Thulborn, Keith R. (2018). "Quantitative sodium MR imaging: A review of its evolving role in medicine". In: *NeuroImage*. Neuroimaging with Ultra-high Field MRI: Present and Future 168, pp. 250–268. ISSN: 1053-8119. DOI: 10.1016/j.neuroimage.2016.11.056.

Truong, Trong-Kha et al. (2006). "Effects of static and radiofrequency magnetic field inhomogeneity in ultra-high field magnetic resonance imaging". In: *Magnetic Resonance Imaging* 24.2, pp. 103–112. ISSN: 0730725X. DOI: 10.1016/j.mri.2005.09.013.

Tsang, Adrian et al. (2011). "Relationship between sodium intensity and perfusion deficits in acute ischemic stroke". In: *Journal of Magnetic Resonance Imaging* 33.1, pp. 41–47. ISSN: 1522-2586. DOI: 10.1002/jmri.22299.

Vaeggemose, Michael, Rolf F. Schulte, and Christoffer Laustsen (2023). "Clinically feasible B1 field correction for multi-organ sodium imaging at 3 T". In: *NMR in Biomedicine* 36.2, e4835. ISSN: 1099-1492. DOI: 10.1002/nbm.4835.

Vaidya, Manushka V. et al. (2016). "Dependence of and field patterns of surface coils on the electrical properties of the sample and the MR operating frequency". In: *Concepts in Magnetic Resonance Part B: Magnetic Resonance Engineering* 46.1, pp. 25–40. ISSN: 1552-504X. DOI: 10.1002/cmr.b.21319.

Vaughan, J. Thomas et al. (2009). "Whole-body imaging at 7T: Preliminary results". In: *Magnetic Resonance in Medicine* 61.1, pp. 244–248. ISSN: 1522-2594. DOI: 10.1002/mrm.21751.

Volz, Steffen, Ulrike Nöth, and Ralf Deichmann (2012). "Correction of systematic errors in quantitative proton density mapping". In: *Magnetic Resonance in Medicine* 68.1, pp. 74–85. ISSN: 1522-2594. DOI: 10.1002/mrm.23206.

Wang, Jinghua, Maolin Qiu, and R. Todd Constable (2005). "In vivo method for correcting transmit/receive nonuniformities with phased array coils". In: *Magnetic Resonance in Medicine* 53.3, pp. 666–674. ISSN: 1522-2594. DOI: 10.1002/mrm.20377.

Wansapura, Janaka P. et al. (1999). "NMR relaxation times in the human brain at 3.0 tesla". In: *Journal of Magnetic Resonance Imaging* 9.4, pp. 531–538. ISSN: 1522-2586. DOI: 10.1002/(SICI)1522-2586(199904)9:4<531::AID-JMRI4>3.0.CO;2-L.

Werbelow, Lawrence G. (2011). "Relaxation Theory for Quadrupolar Nuclei". In: *eMagRes*. American Cancer Society. ISBN: 978-0-470-03459-0. DOI: 10.1002/9780470034590.emrstm0464.pub2.

Wetterling, Friedrich et al. (2012). "Whole body sodium MRI at 3T using an asymmetric birdcage resonator and short echo time sequence: first images of a male volunteer". In: *Physics in Medicine & Biology* 57.14, p. 4555. ISSN: 0031-9155. DOI: 10.1088/0031-9155/57/14/4555.

Wilferth, Tobias, Angelika Mennecke, et al. (2022). "Quantitative 7T sodium magnetic resonance imaging of the human brain using a 32-channel phased-array head coil: Application to patients with secondary progressive multiple sclerosis". In: *NMR in Biomedicine* 35.12, e4806. ISSN: 1099-1492. DOI: 10.1002/nbm.4806.

Wilferth, Tobias, Max Müller, et al. (2022). "Motion-corrected Na MRI of the human brain using interleaved H 3D navigator images". In: *Magnetic Resonance in Medicine* 88.1, pp. 309–321. ISSN: 1522-2594. DOI: 10.1002/mrm.29221.

Winkelmann, S. et al. (2007). "An Optimal Radial Profile Order Based on the Golden Ratio for Time-Resolved MRI". In: *IEEE Transactions on Medical Imaging* 26.1, pp. 68–76. ISSN: 1558-254X. DOI: 10.1109/TMI.2006.885337.

Zaric, Olgica, Alex Farr, et al. (2021). "Tissue Sodium Concentration Quantification at 7.0-T MRI as an Early Marker for Chemotherapy Response in Breast Cancer: A Feasibility Study". In: *Radiology* 299.1, pp. 63–72. ISSN: 0033-8419. DOI: 10.1148/radiol.2021201600.

Zaric, Olgica, Vladimir Juras, et al. (2021). "Frontiers of Sodium MRI Revisited: From Cartilage to Brain Imaging". In: *Journal of Magnetic Resonance Imaging* 54.1, pp. 58–75. ISSN: 1522-2586. DOI: 10.1002/jmri.27326.

Zaric, Olgica, Katja Pinker, et al. (2016). "Quantitative Sodium MR Imaging at 7 T: Initial Results and Comparison with Diffusion-weighted Imaging in Patients with Breast Tumors". In: *Radiology* 280.1, pp. 39–48. ISSN: 0033-8419. DOI: 10.1148/radiol.2016151304.

Zbýň, Štefan et al. (2016). "Evaluation of cartilage repair and osteoarthritis with sodium MRI". In: *NMR in Biomedicine* 29.2, pp. 206–215. ISSN: 1099-1492. DOI: 10.1002/nbm.3280.

Zhuang, Jianqin, Qian Wang, and Rupal Gupta (2023). "Applications of 17O and 51V NMR in inorganic and bioinorganic chemistry". In: *Comprehensive Inorganic Chemistry III (Third Edition)*. Ed. by Jan Reedijk and Kenneth R. Poeppelmeier. Oxford: Elsevier, pp. 35–61. ISBN: 978-0-12-823153-1. DOI: 10.1016/B978-0-12-823144-9.00085-6.

Zöllner, Frank G. et al. (2016). "Quantitative sodium MRI of kidney". In: *NMR in Biomedicine* 29.2, pp. 197–205. ISSN: 1099-1492. DOI: 10.1002/nbm.3274.

List of Figures

List of Tables

Acknowledgment

I would like to take this opportunity to thank everyone who has supported and encouraged me during my time as a doctoral student. My special thanks go to:

Prof. Dr. Mark E. Ladd for the opportunity to work in the department of Medical Physics in Radiology and for supervising my doctoral studies at the Faculty of Physics at the University of Heidelberg and for being first referee of this thesis. I appreciate the opportunity to attend conferences and workshops, it has broadened my scientific knowledge and given me the opportunity to discuss my research, leading to new ideas.

Prof. Dr. Leif Schröder for being second referee for this thesis.

Prof. Dr. Peter Bachert for introducing me to several groups after my oral exam during my master's program, which ultimately led me to choose this fascinating topic and become part of a great team.

Prof. Dr. Armin Nagel and his group for the insightful discussions on X-nuclei MRI and feedback on my work.

Dr. Tanja Platt, who has advised and supported me throughout my thesis. Her many informative explanations and detailed comments helped me to improve my work tremendously. I deeply appreciate the time and effort you dedicated to mentoring me.

Dr. Daniel Paech and his colleagues in the Radiology Department for providing specialized insights from the medical field.

The 3D print and precision mechanics divisions with special thanks to Armin Runz, Volker Stamm, Daniel Vögele, and Rüdiger Schmidt for their help in designing and building the reference vial holder.

Christian Kindtner for his help in organizational matters.

Acknowledgment

Everyone who volunteered for measurements and everyone who proofread parts of my thesis.

All of my former and current 7 T colleagues who have been supportive in case of questions and created an atmosphere that made it very enjoyable to work in this team.

My friends, who gave me the balance I needed during stressful times, but were also understanding when I put work first.

And finally, my family, who always supported me, sent me delicious care packages or flowers, and made my studies possible.